MÖSSBAUER INVESTIGATIONS ON Fe BASED NANO SPINEL FERRITES

By
LOUSHAMBAM HEROJIT SINGH
Enrolment No.: PHYS02200804009

Indira Gandhi Centre for Atomic Research

Kalpakkam, 603102, Tamil Nadu, India

A thesis submitted to the
Board of Studies in Physical Sciences
In partial fulfillment of requirements

For the Degree of

DOCTOR OF PHILOSOPHY

of

HOMI BHABHA NATIONAL INSTITUTE
Deemed University
Mumbai, India

November, 2013

Homi Bhabha National Institute

Recommendations of the Viva Voce Board

As members of the Viva Voce Board, we certify that we have read the dissertation prepared by **Loushambam Herojit Singh** entitled "**Mössbauer investigations on Fe based nano spinel ferrites**" and recommend that it may be accepted as fulfilling the dissertation requirement for the Degree of Doctor of Philosophy.

Date:

Chairman – Dr. C.S. Sundar

Date:

Convener – Dr. R. Govindaraj

Date:

Member 1 – Dr. G. Amarendra

Date:

Member 2 – Dr. K. G. M. Nair

Date:

External Examiner -

Final approval and acceptance of this dissertation is contingent upon the candidate's submission of the final copies of the dissertation to HBNI.

I hereby certify that I have read this dissertation prepared under my direction and recommend that it may be accepted as fulfilling the dissertation requirement.

Date:

Guide – Dr. R. Govindaraj

STATEMENT BY AUTHOR

This dissertation has been submitted in partial fulfillment of requirements for an advanced degree at Homi Bhabha National Institute (HBNI) and is deposited in the Library to be made available to borrowers under rules of the HBNI.

Brief quotations from this dissertation are allowable without special permission, provided that accurate acknowledgement of source is made. Requests for permission for extended quotation from or reproduction of this manuscript in whole or in part may be granted by the Competent Authority of HBNI when in his or her judgment the proposed use of the material is in the interests of scholarship. In all other instances, however, permission must be obtained from the author.

Loushambam Herojit Singh

Kalpakkam

November 2013

DECLARATION

I, hereby declare that the investigation presented in the thesis entitled “Mössbauer investigation on Fe based nano spinel ferrites” submitted to Homi Bhabha National Institute (HBNI), Mumbai, India, for the award of degree of Doctor of Philosophy in Physical Sciences is the record of work carried out by me during the period from September 2008 to November 2013 under the guidance of Dr. R. Govindaraj, Head, Metal physics Section, Materials Science Group, Indira Gandhi Centre for Atomic Research, Kalpakkam. The work is original and has not been submitted earlier as a whole or in part thereof for a degree / diploma at this or any other Institution / University.

Loushambam Herojit Singh

Kalpakkam

November 2013

Dedicated to my parents and folks

ACKNOWLEDGEMENTS

I would like to express my special thanks of gratitude to my thesis supervisor Dr. R. Govindaraj, for his immense efforts to guide and introduce me into the field of Mossbauer spectroscopy. His innovative thoughts thrilled and ignite me to make a way among the ocean of stray scientific problems. Besides I am also thankful to him for moral support and personal caring .

My sincere thanks to the doctoral committee Chairman Dr. C. S. Sundar, Director, Materials Science Group and other members Dr. G. Amarendra, Head, Metal Physics Division, Dr. R. Govindaraj, Head, Metal Physics Section and Dr. K. G. M. Nair, Former Head, Accelerator Materials Section for their constant encouragement and valuable suggestions throughout my PhD.

I would like to extent my hearty thanks deep from my heart to Shri. Sankara Shastry and Smt. Kalavathi for a number of XRD spectra, Dr. R. Mythili for many detailed TEM studies, Dr. P. Ch. Sahu and Dr. N. V. Chandra shekar for high pressure quenching of some of the samples.

My sincere thanks to the members of Metal Physics Section Dr. R. Rajaraman, Dr. G. Venugopal Rao, Mrs. M. Premila, Dr. T. N. Sairam, Dr. S. Abhya, Mrs. J. Parimala, Mr. S. Ragunathan and Mr. Renjith Ramachandran for their kind help and encouragement. I also wish to thank the officials of liquid nitrogen plant for unlimited supply of liquid nitrogen whenever needed. My thanks are also due to Zonal workshop staffs for their benevolent services for fabrication.

My sincere thanks are due to Dr. P. Vasudava Rao , Director of IGCAR for providing opportunity to pursue PhD. I also would like to thank Dr. Baldev Raj and Shri. S. C. Chetal, the former directors of IGCAR for the same.

My sincere thanks to all the MSG members for creating a homely and a very lively academic environment. I would also like to thank Dr. M. Sai Baba and his colleagues for their efforts to make research scholar enclave active and lively.

The acknowledgement would have been incomplete if I miss thanking all of my friends, brothers, sisters and bahenoi (brothers in law) for their physical, moral, economical supports that make me stay in balance at the time of ups and down.

L Herojit Singh
Nov, 2013

CONTENTS

CHAPTER 1

INTRODUCTION

CHAPTER 2

EXPERIMENTAL DETAILS

CHAPTER 3

ATOMIC SCALE CHARACTERIZATION OF MAGNETITE NANOPARTICLES AS SYNTHESIZED THROUGH COPRECIPITATION METHOD

CHAPTER 4

STABILITY OF MAGNETITE NANOPARTICLES CAPPED WITH OLEIC ACID

CHAPTER 5

MAGNETIC INTERACTIONS BETWEEN MAGNETITE NANOPARTICLES FORMED IN ZEOLITE

CHAPTER 6

POINT DEFECTS STUDIES IN NANO AND BULK FERRITES

CHAPTER 7

SUMMARY AND FUTURE PERSPECTIVES

SYNOPSIS

Ferrimagnetic spinel oxides or ferrites have been extensively used for magnetic and microwave applications. Intensive research on magnetite (Fe_3O_4) nano particles has lead to their technological applications in data storage, hyperthermia, magnetic resonance contrast reagent and in vivo drug delivery. Magnetite particles of size close to or less than 10 nm exhibit high magnetic saturation so that these particles show a large response under magnetic field for high density magnetic memory and data storage, drug delivery and hyperthermia. These particles exhibit structure and magnetic properties widely different from that of the bulk counterpart. The spins associated with these particles undergo super paramagnetic relaxation. Although a number of experimental techniques are widely used for characterization of these particles, Mössbauer spectroscopy plays a unique role due to the following reasons. Being a hyperfine interaction based atomic scale technique it provides a detailed understanding of local structure and magnetic properties. ^{57}Fe based Mössbauer spectroscopy is used to address the problems, as the systems to be investigated are nano and bulk ferrites composed mainly of Fe. The effective time of interaction of a Mössbauer resonant absorber with the electromagnetic fields is the lifetime of the isomeric state I=3/2 in the case of ^{57}Fe. This lifetime ($\approx 10^{-7}$ sec) is typically of the order of the inverse of spin relaxation rate of Fe associated with particles of size less than or equal to 10 nm indicating that the Mössbauer spectroscopy is a powerful technique to address aspects related to local structure, magnetic properties including relaxation of spins.

Nano particles are in general produced using techniques such as Sol-gel, hydrothermal, reverse micelle, co precipitation methods. Co precipitation method has been used to produce nano particles of ferrites, the system of investigations of this thesis. These samples contain the nano particles of goethite (α-FeOOH) which is a polymorph of iron oxyhydroxide along with predominantly occurring off-stoichiometric magnetite as characterized using Mössbauer spectroscopy. Annealing in reduced atmosphere restores the stoichiometric nature of the nano particles of the magnetite (Fe_3O_4). At the same time it is important to understand the evolution of goethite which also gets formed in the preparation of Fe_3O_4 nano particles. Based on the Mössbauer results on the sample subjected to controlled heat treatments shown that annealing in the interval between 400-520 K results in the reduction of goethite to off-stoichiometric magnetite while annealing beyond 550 K results predominantly in a topotactic conversion of goethite to haematite (α-Fe_2O_3). Based on this finding we could optimize the concentration of Fe_3O_4 at the cost of hydroxides by a controlled annealing treatment which has been illustrated.

In order to extensively make use of super paramagnetic particles of cubic iron oxides for different applications it is very important to control the size and shape of nano particles by means of surface modification leading to thermal and chemical stability. Physical and chemical stability of iron oxide nano particles are provided by suitable surfactants used to encapsulate these particles. Further, surface spins and hence magnetic interactions between nano particles could be greatly modified by means of surfactants or templates. By means of varying the ratio of concentration of surfactant to nano particles, the mean distance of separation between nano particles could be controlled. Complete understanding of the local structure and magnetic properties of stoichiometric nano particles of magnetite is still lacking mainly due to the fact that the magnetite particles of size less than 10 nm prepared based on many chemical methods remain almost off-stoichiometric.

Strong interaction between nano particles results in a less relaxation time of super paramagnetic spins. In general nano particles are capped with surfactants to control the interaction between nano particles. Oleic acid (OA) is one of the most commonly used surfactants to stabilize iron oxide nano particles as it has been experimentally established that there exists covalent bond between the carboxylic group of OA and Fe cation in iron oxide nano particles. Also a strong reducing behavior of OA could be exploited to obtain stoichiometric nano iron oxide of size close to or less than 10 nm in order to understand structure and magnetic properties of stoichiometric magnetite nano particles.

Zeolite due to its high porosity and uncompensated charges, could act as a good template for magnetite nanoparticles. Zeolite is biocompatible and highly crystalline solid with well arranged pores which trap the nanoparticles and provides a good stability. Not many results have been reported for confining nano particles of magnetite using zeolite which is also biocompatible. Different aspects such as stability of magnetite particles formed in zeolite and the interaction between magnetite particles as dispersed in zeolite have been addressed in this thesis.

Defect induced ferromagnetism in antiferromagnetic materials has been intensely investigated in the past decade. Bulk Zinc ferrite ($ZnFe_2O_4$) with a normal spinel configuration having A and B sites populated only with Zn^{2+} and Fe^{3+} respectively exhibits antiferromagnetic ordering with Neel temperature 10 K. In contrast the nano particles of zinc ferrite display ferromagnetic ordering understood as due to a partial inversion of the population of Fe^{3+} and Zn^{2+}. Ferromagnetic ordering has been reported in the bulk $ZnFe_2O_4$ synthesized using molten salt displaying high magnetization. Point defects aspects in terms of antisites, cationic and anionic vacancies have been addressed in the present thesis in order to understand the magnetic properties in nano ferrites under investigations. Thesis is presented in seven chapters whose main contents are summarized as follows. Chapter 1 gives a brief overview on bulk and nano ferrites and their important applications focusing on the issues related to local structure and magnetic properties which need to be understood. The unique role of Mössbauer spectroscopy as a powerful tool for addressing the aspects related to local structure and magnetic properties of nano ferrites would be elucidated. Chapter 2 describes the methodology of Mössbauer spectroscopy would be discussed. Details pertaining to spectrometer, data analysis and the results obtained in standard reference samples would be presented. Co-precipitation, a method employed for the preparation of nano particles in the present thesis would be discussed. Chapter 3 discusses about the synthesis of magnetite (Fe_3O_4) nano particles using appropriate precursor solutions of Fe^{3+} and Fe^{2+} in the molar ratio 2:1 by coprecipitation method. Mössbauer results point to the off-stoichiometric nature of magnetite nano particles. Annealing results on the evolution of local structure and magnetic properties due to reduction and coarsening of magnetite nano particles is presented. Mössbauer results in the sample prepared using coprecipitation method also indicate the occurrence of goethite particles along with the predominantly present off-stoichiometric magnetite. Evolution of local structure and magnetic properties of the associated goethite particles with controlled annealing treatments is discussed in a detailed manner. Based on the Mössbauer results obtained in this study a two step annealing process has been followed to significantly optimize the reduction of goethite to magnetite which would be illustrated in this chapter. Chapter 4 elucidates about the technological applicability of the nanoparticles where control of the size and shape comes out to be a very important issue. As the particle size decreases the surface effect becomes more significant due to an increase in the surface to volume ratio of the particle, therefore the nanoparticles become highly reactive and unstable. Controlling the size, shape in addition to maintaining the phase stability of the nano particles requires the particles to be capped or grown in a suitable template. Oleic acid has been chosen as a suitable surfactant for capping α-FeOOH and Fe_3O_4 nanocomposites. Optimization of Fe_3O_4 from the nano composites of off-stoichiometic magnetite and α-FeOOH by controlled annealing process is presented. An interesting linear correlation between hyperfine parameters viz., mean quadrupole splitting and hyperfine field that was deduced in the reduction of goethite to magnetite and hence to FeO is presented and discussed. The magnetic interaction between stoichiometric magnetite particles has also been deduced by means of carrying out Mössbauer studies at low temperature in the interval 300 –80 K. Chapter 5 would deal with the stability provided by the template, particle-particle interaction with respect to the interparticle distance which was compared with bare magnetite nanoparticles. Mössbauer results show that the Fe_3O_4 nanoparticles are strongly bound in zeolite matrix. Magnetic interaction between the dispersed Fe_3O_4 nanoparticles has been deduced across 300 – 80 K. Chapter 6 shows the results of Mössbauer studies carried out on Fe_3O_4 nano particles pointing to a possibility of the partial occupation of Fe^{2+} at tetrahedral sites are reported in this chapter. Point defects in terms of partial inversion of Fe^{3+} and Zn^{2+} at tetrahedral and octahedral sites leading to ferromagnetic ordering in nano zinc ferrites has also been discussed in this chapter. These results are compared with that of defect associated bulk zinc ferrites exhibiting ferromagnetism. Chapter 7 summarizes the findings reported in the thesis and the future perspectives

LIST OF FIGURES

LIST OF TABLES

LIST OF ABBREVIATION

Symbols	**Abbreviation**
A	Tetrahedral site
B	Octahedral site
D	Divalent cations
T	Trivalent cations
μ_o	Vacuum permeability
ΔE_{MS}	Magneto static energy
E_{dw}	Domain wall energy
D_c	Critical diameter
A	Exchange constant
K_{eff}	Anisotropic constant
M_S	Saturation magnetization
M_R	Remanence magnetization
H_C	Coercivity
$E(\theta)$	Magnetic anisotropy energy
V	Particle volume

θ	Angle
J	Exchange energy
R_{gd}	Radius of the ground state nucleus
R_{ex}	Radius of the excited state nucleus
Z	Atomic number
e	Electronic charge
	Wave function
ν	Frequency
c	Velocity of light
θ_D	Debye temperature
$\boldsymbol{\mu}$	Nuclear dipole moment
H	Magnetic field strength
I	Nuclear spin
μ_N	Nuclear magneton
Γ_i	Width of the ith component
δ_i	Isomer shift of the ith component
Δ_i	Quadrupole splitting of the ith component
Bhf_i	Hyperfine field of the ith component
f_i	Area of the ith component
k_B	Boltzmann’s constant
T	Temperature
τ	Relaxation time
ZFO	Zinc ferrite
b-ZFO	Bulk Zinc ferrite
n-ZFO	Nano Zinc ferrite

CHAPTER 1

INTRODUCTION

Chapter 1

INTRODUCTION

1.1 Motivation

Ferrites in general exhibit insulating or semiconducting and ferrimagnetic behavior and hence they are widely useful in microwave appliances and magnetic recording [1]. They have widespread applications in electronics [2], magneto-optics [3], magneto caloric refrigeration [4], high density magnetic memory [5], oscillation damping [6] and catalysis [7]. Magnetite, the oldest magnetic material known to the mankind, remains as an interesting system with respect to applications for spintronic devices [8]**.** A complete understanding of the physics of Verwey transition i.e. the variation of resistivity over several orders of magnitude from high temperature metallic to insulating behavior around 120 K is yet to emerge [9,10]**.** Nano particles of spinel oxides exhibit electronic, magnetic and structural properties widely different from that of the bulk analogue [11-19]. As shown schematically in Figure 1.1 and Table 1.1, most of the applications of spinel ferrites emerge due to small size of the particles in the range 5-10 nm. Among the nanocrystalline ferrites Fe_3O_4 and γ-Fe_2O_3 are biocompatible. Hence they have attracted interest for different biomedical applications such as enzyme encapsulation, biosensor design, cell labeling / separation, image contrast in magnetic resonance imaging. Also these are widely used in tumor hyperthermia and magnetically targeted drug delivery due to their dimensions being comparable to the cells and biomolecules [20]. Due to high saturation magnetization values these particles could be easily manipulated with low magnetic fields. The active surface of the nanoferrites could be used to bind toxic heavy metal ions towards purification of water [21].

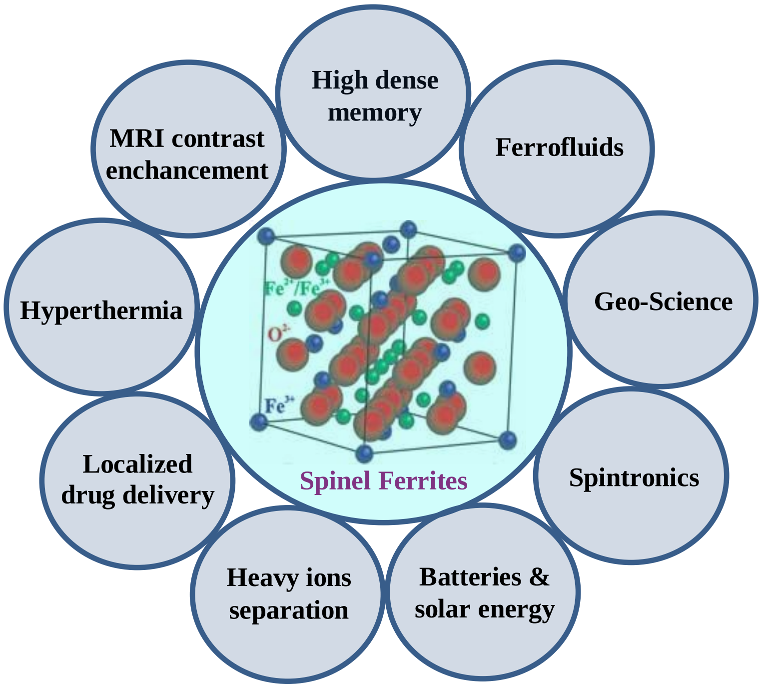

Figure 1.1: Schematics on various applications of spinel ferrites.

Table 1.1. Various compositions of spinel ferrites with its application.

Application	Spinel Ferrites	Ref
High density memory devices	$CoFe_2O_4$ nanodots	[22]
Magnetic Resonance Imaging	Fe_3O_4-Mesoporous silica nanoparticles and Surface modification with PEG, Fe_3O_4 nanoparticles conjugated to a cancer-targeting antibody, Herceptin.	[23,24]
Hyperthermia	Fe_3O_4 nanoparticles capped with oleic acid or polyethylene glycol.	[25]
Drug delivery	Fe_3O_4 in zeolite	[26]
Ions separation	Fe_3O_4 Magnetic Nanoparticles with Humic Acid, Fe_3O_4 nano particles entrapped in iron oxyhydroxides	[27,28]
Battery	M_3O_4 (M = Fe, Mn, Co) Anodes	[29]
Solar energy	$ZnFe_2O_4$, α-$Fe_2O_3/ZnFe_2O_4$ composite	[30,31]
GeoScience	Magnetite	[32]

The thermal conductivity as studied on ferrofluids prepared using spinel ferrites was predicted to be highly efficient and can be utilized to drive heat from Micro-Electro-Mechanical (MEMS) devices [33]. Some of the ferrites $ZnFe_2O_4$, $NiFe_2O_4$ and $Li_{0.35}Cd_{0.3}Fe_{2.35}O_4$ are also known to have application with respect to solar energy cells, lithium batteries [34,35].

Several physical, chemical, electronic and magnetic properties of the nanoparticles are very important to be understood for wider applications. Magnetite particles of size below 15 nm are reported to be partly off-stoichiometric [48]. Hence it is important to understand the local structure, magnetic properties of the nanoparticles and the evolution of these properties due to coarsening. Coarsening of nanoparticles should be strictly prevented for their usage in biomedical applications. This is usually done by means of either capping of the nanoparticles with proper surfactant or by dispersing the nanoparticles in suitable template. It should be borne in mind that either the surfactant or the template used for these studies should be biocompatible as far as biomedical applications of nanoparticles are concerned. Template exhibiting a strong binding of iron oxide nanoparticles could be contemplated for space and high temperature applications. A complete understanding of the stability of nanoparticles, intra and inter particle interactions are still lacking in spite of an innumerable work carried out on several aspects of nanoparticles [36,37]. Several issues related to site occupancies of cations, role of surfactant in modifying the magnetic interactions if any, binding of nanoparticles in suitable templates need to be investigated in a detailed manner in order to use these particles for several applications such as biomedical, high density memory, microwave and multi functional oxides. This thesis addresses the issues related to the variation in the local structure and magnetic properties with respect to an increase in the size of the nanoparticles due to coarsening caused by controlled annealing treatments. Other issues such as the stability, magnetic interactions between iron oxide nanoparticles either capped with surfactant or bound in template are also addressed. Introduction to local structure and magnetic properties of Fe based bulk and nano spinel ferrite is provided in the following discussion.

1.2 Structure and magnetic properties of Bulk Ferrites

Spinel ferrites possess crystal structure of the natural spinel $MgAl_2O_4$ as determined by Bragg [38]. Spinel oxides with a general formula AB_2O_4 crystallize in the cubic crystal system and belong to the space group Fd3m (O_h^7). Oxygen anions are arranged in a cubic close packed lattice to form 64 tetrahedrons and 32 octahedrons in a unit cell, while the cations A and B occupy 8 tetrahedral and 16 octahedral sites respectively. In the case of natural spinel $MgAl_2O_4$, Mg^{2+} and Al^{3+} occupy tetrahedral and octahedral sites respectively. In general this can be configured as $(D^{2+})[T^{3+}]_2O_4$ in which eight numbers of divalent cations occupy tetrahedral sites while all the octahedral sites are only occupied by sixteen trivalent cations known as normal ferrites (e.g) $ZnFe_2O_4$, $AlFe_2O_4$. Different cation distribution with the occupation of half of trivalent cations T^{3+} at tetrahedral and octahedral sites while all the divalent cations D^{2+} are understood to occupy octahedral sites is known as inverse ferrites $(T^{3+})[T^{3+} D^{2+}]_2O_4$ (e.g.) Fe_3O_4, $NiFe_2O_4$, $CoFe_2O_4$ [39]**.** An intermediate cation distribution is expressed as $(T_{1-d}^{3+} D_d^{2+})[T_d^{3+} D_{2-d}^{2+}]O_4$ is known as partially inverted ferrite with d as the degree of inversion $Zn_{1-d}Mg_dFe_2O_4$. Elastic energy, electrostatic energy and crystal field splitting dictate the cation distribution resulting in different configuration of spinel ferrites. Based on Neel's theory of ferrimagnetism, inter and intra-sublattice superexchange interactions between A-B, A-A and B-B are mediated via anion p orbital. Strength of superexchange interactions is dependent on the electronic structure of cations as well as on the geometry of the relative configuration of the interacting cations and intermediate anions. Strength of antiferromagnetic A-B interaction is being much stronger than that of other two such that $J_{AB} > J_{AA} > J_{BB}$ results in ferrimagnetic ordering.

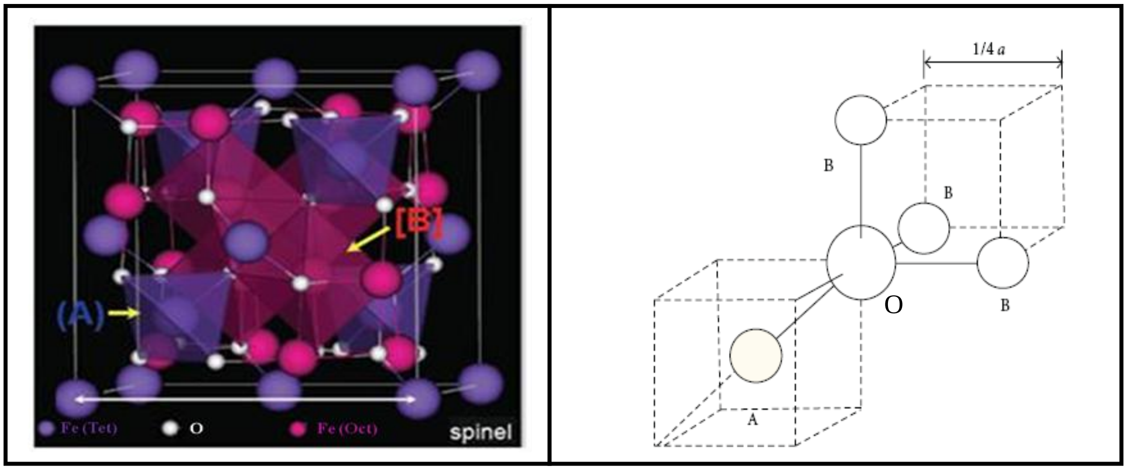

Figure 1.2: Schematic of the unit cell of Fe_3O_4 with eight tetrahedral A sites are occupied by only Fe^{3+} while the sixteen octahedral B sites are occupied by both Fe^{3+} and Fe^{2+} Tetrahedral A and octahedral B sites are marked as shown.

J_{AB}, antiferromagnetic super exchange interaction, is much larger in magnitude than ferromagnetic superexchange interaction J_{BB} mediated by (B-O-B) and double exchange interaction between Fe^{3+} and Fe^{2+} at B sites, as shown schematically in Figure (1.2 & 1.3). Spinel ferrites are characterized by ionic bonding and they are mostly insulating. Electrical resistivity exhibits a sharp decrease even if a small concentration of Fe^{3+} is reduced to Fe^{2+} [47]. In the absence of mixed Fe valances these spinel ferrites remain as insulators.

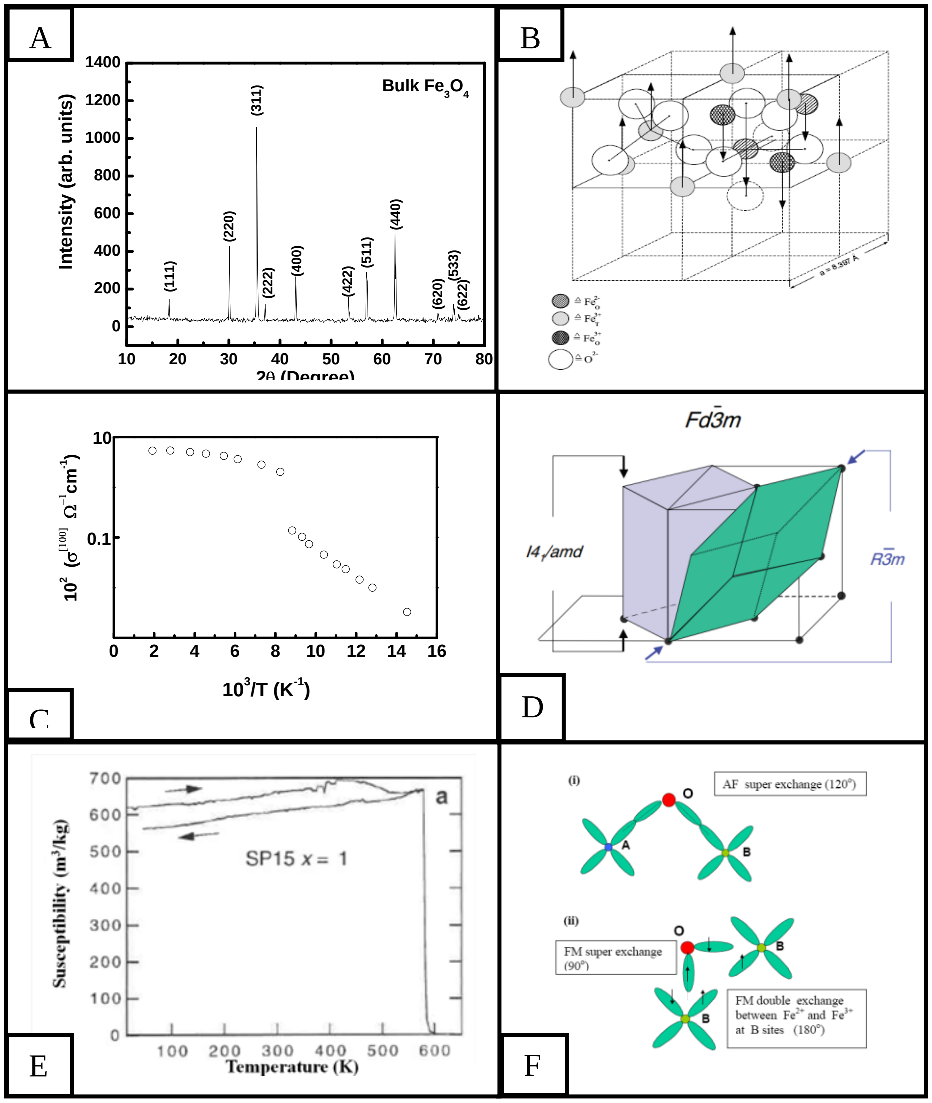

Figure 1.3: XRD spectrum and crystal structure of Fe_3O_4 are shown in (A) and (B) respectively. Variation of electrical conductivity with 1/T exhibits a sharp decrease in the conductivity below 125 K as shown in (C) is understood to be due to cubic to rhombohedral distortion (D). Figure E shows a sharp decrease in susceptibility around 550 C marking the ferromagnetic to paramagnetic transition. While (F) shows the schematic of the AF and FM superexchange interactions such as A-O-B and B-O-B respectively and Fe^{2+}-O-Fe^{3+} double exchange interaction. J_{AB} is much larger than that of J_{AA} and J_{BB} resulting in ferromagnetic ordering.

In the case of MFe_2O_4 the occupation of Fe at both tetrahedral and octahedral sites results in inverse spinel configuration (e.g. $NiFe_2O_4$, $CoFe_2O_4$, $MgFe_2O_4$), while in the case of the normal ferrites metal cations M and Fe occupy only A and B sites respectively (e.g. $ZnFe_2O_4$, $AlFe_2O_4$) resulting in a different magnetic property as compared to that of inverse ferrites. For example in the case of Fe_3O_4, a classic case of an inverse spinel oxide, 8 numbers of Fe^{2+} totally occupy B sites while 16 numbers of Fe^{3+} equally occupy A and B sites. Fe^{3+} and Fe^{2+} are of electronic configurations d^5 and d^6 respectively. The most important interaction between iron ions on the octahedral sites is the double exchange interaction based on the electron transfer between Fe^{2+} and Fe^{3+} which is possible when both the ions are aligned ferromagnetically. This results in an increase in the bandwidth thus favoring a ferromagnetic alignment. J_{AB} interaction due to overlap of the e_g orbitals on the B sites and t_{2g} orbitals on the A sites results in a strong antiferromagnetic coupling thus resulting in a high curie temp of 858 K.

1.3 Nano Ferrites

While the size of the particles become lesser than 100 nm there is an increase in the ratio of the atoms occupying surface to volume. Nano particles of ferrite could be exhibiting point defects such as cationic and anionic vacancies whose concentration are likely to be high at the surface [40]. Thus smaller the particle size larger is the contribution by these kinds of defects for the observed variation in the electronic and magnetic properties as compared to the bulk analogue. In large magnetic particles the regions of uniform magnetization are separated by domain walls in order to balance between magneto static energy ΔE_{MS} and domain wall energy E_{dw}. Magnetostatic energy increases with increasing volume of the material while domain wall energy increases with increasing interfacial area between domains. On reduction of the size of the particles there is a critical volume below which it costs more energy to create a domain wall than to support the external magnetostatic energy of the single domain state. This critical diameter typically lies in the range of a few tens of nanometers and depends on the material. It is influenced by the contribution from various anisotropy energy terms. Particle exist in single-domain state below critical diameter D_c, where $\Delta E_{MS} = E_{dw}$, which implies $D_c \approx 18\frac{\sqrt{AK_{eff}}}{\mu_o M^2}$, where A is the exchange constant, K_{eff} is anisotropy constant, μ_o is the vacuum permeability, and M is the saturation magnetization [41].

The superparamagnetism can be understood by considering the behavior of a well-isolated single-domain particle. The magnetic anisotropy energy per particle which is responsible for holding the magnetic moments along an easy axis can be expressed as follows: $E(\theta)=K_{eff}V\sin^2\theta$, where V is the particle volume, K_{eff} anisotropy constant and θ is the angle between the magnetization and the easy axis. The energy barrier $K_{eff}V$ separates the two energetically equivalent easy directions of magnetization. With decreasing particle size, the thermal energy, k_BT, exceeds the energy barrier $K_{eff}V$ and the magnetization is easily flipped. For $k_BT > K_{eff}V$ the system behaves like a paramagnet, instead of atomic magnetic moments. This system is named a superparamagnet [41]. Such a system has no coercitivity and the relaxation time of the moment of a particle, τ, is given by the Neel-Brown expression $\tau = \tau_o \exp [K_{eff}V/k_BT]$, where k_B is the Boltzmann's constant and the value of τ_o is of the order of 10^{-12} to 10^{-9} seconds and is almost temperature independent [42]. If the particle magnetic moment reverses at times shorter than the experimental time scales, the system is in a superparamagnetic state, if not, it is in the so-called blocked state. The temperature, which separates these two regimes, the so called blocking temperature, T_B, depends on the effective anisotropy constant, the size of the particles, the applied magnetic field, and the experimental measuring time.

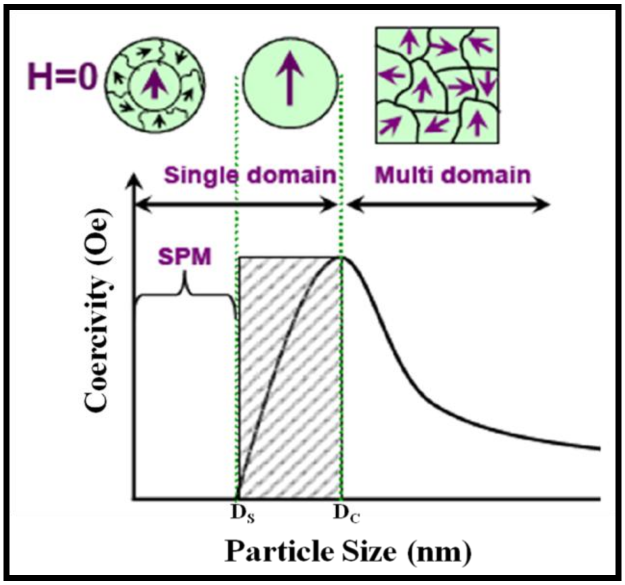

Figure 1.4: ***Variation of coercivity with particle size, where D_C signifies the critical radius below which the particles become single domain and D_S stand for the radius below which the particles behave superparamagnetic.***

The magnetic, electronic and physical properties of a particle are strongly dependent on the particle size [43]. Dependence of coercitivity (H_c) with respect to particle size (Cf. Figure 1.4) was known in the 1950s with the discovery of single domain magnetism [1]. Experimental investigation found the increase in the coercitivity with decreasing particle size, independent of the material. In a larger particle, magnetic domains are separated by domain walls and the motion of the walls is a primary means of reversing magnetization [44]. At the critical size (D_C) where the multidomain turns out to be a single domain particle, the coercitivity obtained is maxima. Any further decrease in the particle size leads to the reduction of coercitivity which is due to the contribution of thermal agitation, and when the thermal energy becomes equal or greater than the magnetostatic energy, it results in a zero coercitivity [45].

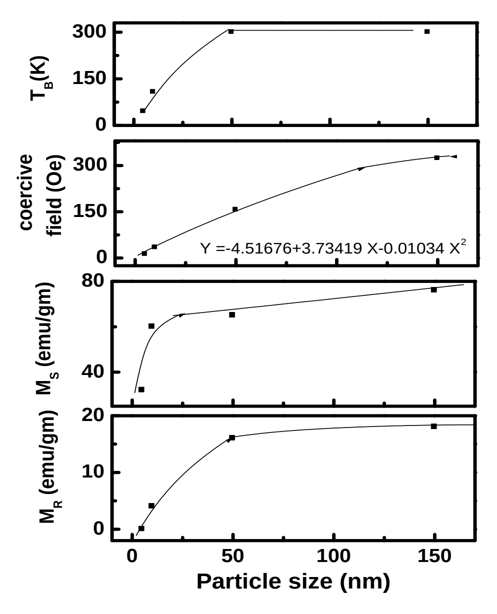

Figure 1.5: Variation of coercive field, saturation magnetization (M_S), Remanence (M_R) with particle size. Blocking temperature (T_B) has been obtained from the ZFC and FC curves for samples of different sizes [46].

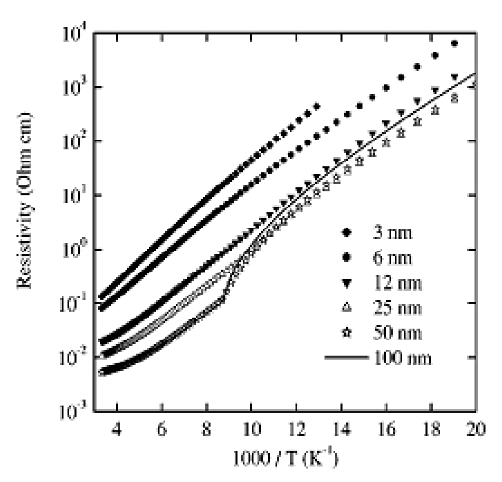

Figure 1.6: Variation of resistivity with inverse of temperature for magnetite film of different thickness. It is seen that for a film thickness beyond 50 nm the sample is observed to exhibit verwey transition. Commensurately magnetization results (Cf. Fig 1.5) show that the nanoparticles of size close to or larger than 50 nm exhibits bulk like magnetic behavior [47].

Shown in Figure 1.5 are the magnetization results as obtained in nanoparticles of magnetite of different sizes [46]. It can be seen that the magnetite particles of size close to or beyond 100 nm exhibit coercive field close to that of the bulk, while the values of M_s and M_r saturate for particles of size close or larger than 50 nm. Also it is important to note that around 100 K the values of ρ varies by two orders of magnitude for magnetite films of thickness ranging between 50-3 nm (c.f. Figure 1.6) [47]. Films of thickness equal to or higher than 50 nm exhibit Verwey transition similar to that of the bulk. Also it is seen that for the particles of different size (4 nm $<$ d $<$ 50 nm) the blocking temperature varies between 300-50 K. Thus both the transport and magnetic properties are seen to be dependent upon the size (either thickness of the film or diameter of the nanoparticle) of the system. Hence it is important to investigate an entirely different magnetic, electronic and structural properties exhibited either by nanoparticles of diameter (thin films of thickness) less than 50 nm. In particular the possible role of point defects such as cationic vacancies, cationic anti site defects and anionic vacancies resulting in entirely different magnetic, electronic and structural properties is important to be investigated.

1.4 Some of the important outstanding issues related to local structure and magnetic properties of nano ferrites

Superparamagnetic iron oxide nanoparticles (SPION) find an extensive application in medical and magnetic high density memory applications. In order to continue to use these particles for different such applications it is important to preserve the physical and chemical stability of nanoparticles. It is mentioned in the literature [48] that magnetic particles of size less than 20 nm remain off-stoichiometric. It is quite important to understand the point defects aspects of this off-stoichiometric magnetite.

Interparticle interactions, intra particle surface defects, core-shell structure are important to be considered. Strong magnetic interactions between bare nanoparticles could result in the instability of the nanoparticles. In general surfactants such as oleic acid are used for providing the physical and chemical stability. Also by means of binding the nanoparticles concerned with suitable surfactant it is possible to incorporate physical separations of the particles thus leading to reduced magnetic interactions. It is also required to understand the stability of oleic acid coated nanoparticles.

Bulk $ZnFe_2O_4$ is a normal ferrite with the complete occupation of Zn and Fe at A and B sites respectively. With the resultant J_{AB}=0, J_{AA}=0 and J_{BB} being very small results only in a weak antiferromagnetic ordering with a Neel temperature of 10 K. But it has been reported in the literature that in nano zinc ferrite there is a ferromagnetic ordering with a magnetic ordering temperature lying in the range 50-100 K [49,50]. This is understood to be due to partial inversion in the population of Zn and Fe occupying A and B sites respectively. It is essential to understand the role of point defects besides that of antisites such as Zn(Fe) and vice-versa in nano zinc ferrite leading to the observed weak ferromagnetism. It is important to understand as to how the size reduction effectively results in a partial inversion of cations occupying A and B sites in nano zinc ferrite.

It is already seen that the magnetic ordering in these oxides is dictated by super exchange interaction between Fe-O-Fe. Hence O^{2-} anions might play a crucial role for magnetic properties of the system. Oxygen vacancies if any exist in addition to affecting to local structure also leads to disruption of the superexchange interactions. Thus defects in terms of anionic and cationic vacancies play an important role in modifying both the local structural and magnetic interactions. Due to low valence of oxygen X-ray based techniques would not be able to provide a good understanding of structural or magnetic aspects of the system. Hyperfine interaction based techniques to study the interaction between the moments of Fe with the electromagnetic fields at their sites have been carried out extensively to understand the magnetic and structural aspects of spinel oxides. In this thesis work the local structure and magnetic properties at Fe sites in nano ferrites have been extensively studied using Mössbauer spectroscopy.

1.5 Mössbauer spectroscopy as a powerful technique for atomic scale characterization of bulk and nano ferrites

Magnetite particles of size close to or less than 10 nm are superparamagnetic at room temperature exhibiting a spin relaxation time of the order of 10^{-8} seconds. Hence any technique with the time scale of measurement close to 10^{-8} seconds could be a powerful tool for studying the magnetism of these particles.

Hence it is essential to study the local structure and magnetic properties at Fe sites in these systems. Mössbauer spectroscopy, a hyperfine interaction based technique, is one of the most powerful techniques to address the problems related to local structure and magnetic properties in spinel ferrites. Interaction between nuclear moments of a probe or absorber nucleus at its isomeric state with electromagnetic fields at the sites results in a shift and splitting, resulting in the removal of (2I+1) fold degeneracy of nuclear levels. Basic methodology of Mössbauer spectroscopy in terms of the principle and deduction of hyperfine parameters related to the solid state properties of the system of interest are explained in a detailed manner as follows.

1.5.1. Basic methodology of Mössbauer spectroscopy

Mössbauer spectroscopy is based on the phenomenon of recoilless emission and resonant absorption of nuclear gamma rays in bound nuclei of solids, known as Mössbauer effect. It was discovered in 1958 by Rudolf. L. Mössbauer. In view of the sharpness of the zero phonon emission line (10^{-7} eV), limited only by the lifetime of the excited state, it was immediately realized that this resonance phenomenon could be used as a probe of the magnetic and quadrupole interaction of the nuclear moments with the surrounding electrons. There exists number of Mössbauer isotopes among which ^{57}Fe, ^{119}Sn and ^{61}Ni are commonly used [48,51,52]. ^{57}Fe is the most commonly used isotope. The reasonably low gamma energy reduces the recoil of nuclei, longer half life time of the gamma source and the high abundance of Fe and its compound expand the scale of application of ^{57}Fe Mössbauer spectroscopy. In the course of time Mössbauer spectroscopy has been developed miraculously that its demand increases from basic science to the medical and technological purpose. Application of Mössbauer spectroscopy in probing solid state materials brings out a very good understanding of the local structure, electronic and magnetic properties, relaxation phenomena and lattice dynamics [53-58]. A detailed description of the instrument and application can be found in many review articles and books [59-62]. Interaction between nuclear moments at the isomeric state of resonant absorber atoms with electromagnetic fields results in a shift and splitting of nuclear energy levels. By means of Doppler shifting of the source γ-rays energy the resonant absorption is measured as a function of the relative velocity of the source with respect to the absorber in a Mössbauer measurement. Different terms of hyperfine interaction and the deduced solid state parameters have been explained in the following.

1.5.1.1 Isomer shift due to electric monopole interaction

The nuclear energy levels respond to the change in the s-electron density which arises due to change in valence electrons via shielding effect resulting to an altered Coulombic interaction which manifests itself as a shift in the nuclear levels as shown in Figure 1.7. The term “isomer shift” has been uniformly adopted because the effect depends on the difference in the nuclear radii of the ground (R_{gd}) and isomeric, excited (R_{ex}) states. The term “chemical shift” has also been used. The effect is properly considered as a part of electric hyperfine interaction and called as the “electric monopole interaction” in analogy with the electric quadrupole splitting.

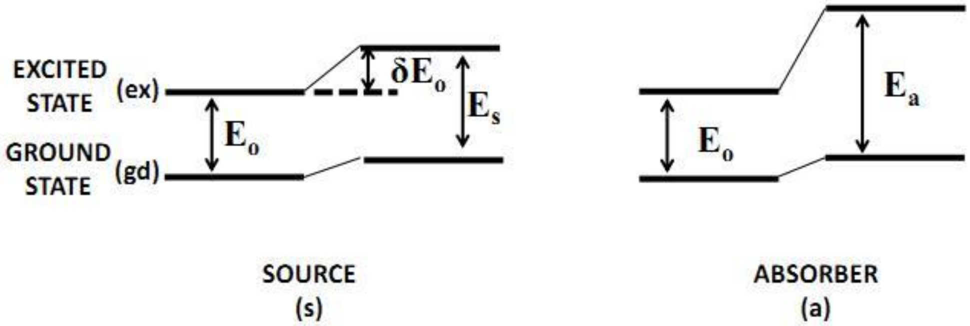

Figure 1.7: Nuclear energy levels of a source and an absorber.

The change in the energy of the gamma ray due to the nuclear electrostatic interaction can be expressed as:

$$\delta E = \delta E_{ex} - \delta E_{gd} = \frac{2\pi}{5} Ze^2 |\psi(0)|^2 (R_{ex}^2 - R_{gd}^2) \text{ ----------- (1), Where,}$$

$-e|\psi(0)|^2$ is the s-electronic charge density.

The gamma ray energy of a recoilless free emission and absorption is given by:

$$E_s = E_o + \frac{2\pi}{5} Ze^2 |\psi_s(0)|^2 (R_{ex}^2 - R_{gd}^2) \text{ ------------------- (2)}$$

And,

$$E_a = E_o + \frac{2\pi}{5} Ze^2 |\psi_a(0)|^2 (R_{ex}^2 - R_{gd}^2) \text{ ------------------- (3)}$$

Therefore, Isomer shift (IS) = E_a - E_s

$$= \frac{2\pi}{5} Ze^2 [|\psi_a(0)|^2 - [|\psi_s(0)|^2](R_{ex}^2 - R_{gd}^2) \text{ ---- (4)}$$

The simplified formula for chemical isomer shift is given as

$$\delta_c = \Delta E_{IS}\ c/E_o\ = \alpha\ \Delta|\psi\ (0)|^2$$

where ΔE_{IS} is the difference between the median transition energies of the absorber (E_A) and the source (Es). c/Eo is the Doppler conversion factor from energy to speed. $\Delta|\psi\ (0)|^2$ is the difference between the electron densities at two identical nuclei, one of which is embedded in the source material, while the other in the absorber material. Among others the factor α comprises of many factors including the relative difference between the radius of source and absorber atoms.

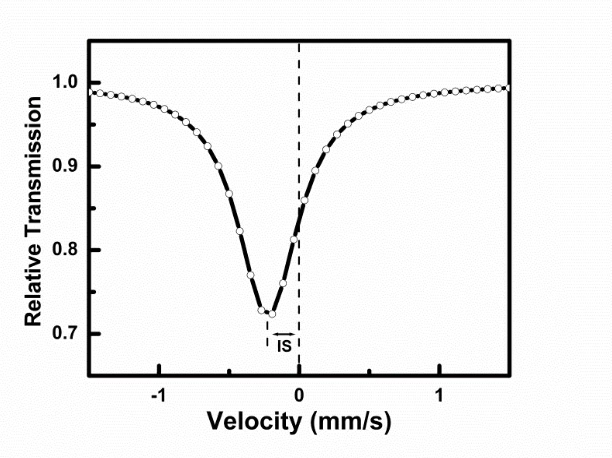

Figure 1.8: Mössbauer spectrum of a sample exhibiting electric monopole interaction alone.

Another effect that contributes to shift in the energy is due to thermal fluctutaion associated with vibrating atoms. The emitting or absorbing atoms are vibrating with a frequency of 10^{12} Hz. Although this is too fast to influence the Mössbauer absorption there is a relativistic second order contribution to the Doppler effect that will change the frequency of the emitted gamma ray as

$\nu' = \nu\ \sqrt{(1 - v^2/c^2)}$

This second order doppler shift (SOD) is added to the isomer shift and the sum is referred to as centroid shift. The crystal vibrations are temperature dependent and based on the debye model of vibrations of atoms the second order doppler shift could be derived based on the Debye model as

$$\text{SOD} = -2.19 \times 10^{-3}\ T^4/\ \theta_D^3 \int_0^{\theta_D/T} x^3 dx\ /\ (e^x-1) \quad \text{mm/sec}$$

Hence the SOD at high temperature is almost dependent of the Debye temperature (Θ_D) of the crystal. Hence SOD will be contributing dominantly at the low temperatures. Hence at room temperature the centroid shift is almost same as isomer shift (c.f. Figure 1.8).

1.5.1.2 Magnetic hyperfine field due to magnetic interaction

The magnetic hyperfine structure arises from the interaction of the magnetic dipole moment **μ** at the isomeric state with the magnetic field, **H**, due to the atom's own electrons. The eigenvalues of the Hamiltonian of the interaction or the energy levels obtained are

$$E_m = -\mu\frac{Hm_I}{I} = -g\mu_n Hm_I\ ,$$

$$m_I = I, I-1, \ldots, -I \quad \text{--- (7)}$$

Splitting due to magnetic hyperfine interaction is hence given as

$$\Delta_m = \Delta E_m \quad c/E_o = -g_I\, \mu_N\, B_{eff}\, c/E_o$$

where ΔE_m is the energy splitting due to magnetic interaction. g_I is a nuclear factor depends on the nuclear spin I of the nucleus, m_I is the magnetic quantum number and μ_N is the nuclear magneton. Effective magnetic field at the site of a resonant absorber is essentially due to the combination of different mechanisms such as Fermi contact interaction, orbital and dipolar interactions. Fermi contact field (H^c) arises from a net spin-up or spin-down s-electron density at the nucleus as a consequence of spin polarization of inner filled s-shells by spin-polarized partially filled outer shells. Hyperfine field H^L is due to orbital motion of valence electrons with the orbital momentum quantum number L. Spin dipolar field H^d is understood to arise from the total electron spin of the atom under consideration. All contributions add up to the total effective magnetic field $H_{eff} = H^c + H^L + H^d$.

The allowed gamma transitions between the equally spaced sublevels of the excited state and those of the ground state in the case of pure magnetic interaction between nuclear magnetic moment with effective magnetic field are given by the selection rules for magnetic dipole transitions: $\Delta I = 1$, $\Delta m_I = 0, \pm 1$. Therefore for ^{57}Fe having ground state I = 1/2 and excited state I = 3/2, exhibit 6 allowed transition as shown in Figure 1.9.

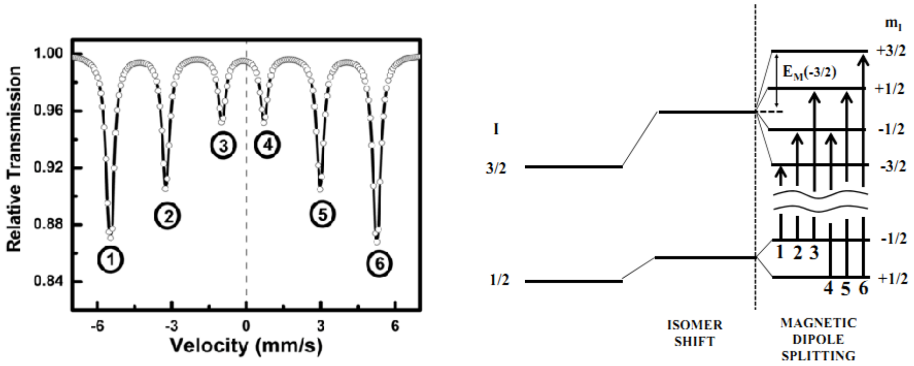

Figure 1.9: Mössbauer spectrum of a magnetically ordered material (left) and the energy transition corresponding to the peak of Mössbauer spectrum (right).

In a Mössbauer spectrum of a magnetically ordered absorber usually observes a resonance sextet, the centroid of the spectrum may be shifted from zero velocity by electric monopole interaction yielding the isomer shift parameter δ. The peak position assigned to the peaks of Mössbauer spectrum (Figure 1.9 (left)) refer to those of the γ-ray transitions between the sublevels of the excited state and the ground state (right). The relative intensities of the various allowed transitions as determined by the squares of the Clebsch-Gordan coefficients are given in Table 1.2.

Table 1.2. Various allowed transition and its relative intensity

Transitions	Δm	Total	Angular dependence
3/2 → 1/2 -3/2 → -1/2	-1 +1	3	$\frac{9}{4}(1+\cos^2\theta)$
1/2 → 1/2 -1/2 → -1/2	0 0	2	3 $\sin^2\theta$
-1/2 → 1/2 1/2 → -1/2	+1 -1	1	$\frac{3}{4}(1+\cos^2\theta)$

For isotropic orientation of magnetic spins with respect to the γ-ray propagation the relative intensities are 3:2:1:1:2:3. The separation between the lines 2 and 4 (3 and 5) refers to the magnetic dipole splitting of the ground state. The separation between lines 5 and 6 (1 and 2, 2 and 3, 4 and 5) refers to the magnetic dipole splitting of the excited I = 3/2 state. The magnetic hyperfine splitting can be utilized to determine the magnitude of the effective magnetic field and direction acting at the nucleus.

1.5.1.3 Quadrupole splitting due to electric quadrupole interaction:

Interaction between nuclear quadrupole moment with the electric field gradient at the site of absorber atoms results in quadrupole splitting of isomeric state. The electric field gradient can be qualitatively understood to be due to valence electronic term V_{zz}^{latt} resulting from an inequivalent electronic properties of five 3d orbitals of Fe and V_{zz}^{latt} which is due to non-cubic symmetry at absorber site. V_{zz}^{latt} could arise either due to point defects associated with the absorber atoms or the non-cubic symmetry of the matrix.

Due to the quadrupole interaction the isomeric state with spin I=3/2 is split in to $\pm$3/2 and $\pm$1/2 while there is no splitting of ground state spin with I= $\pm$1/2 (Cf. Fig.1.10). Resonant absorption of 14.4 keV rays by absorber atoms results in a doublet in a Mössbauer spectrum as shown in Fig 1.11.

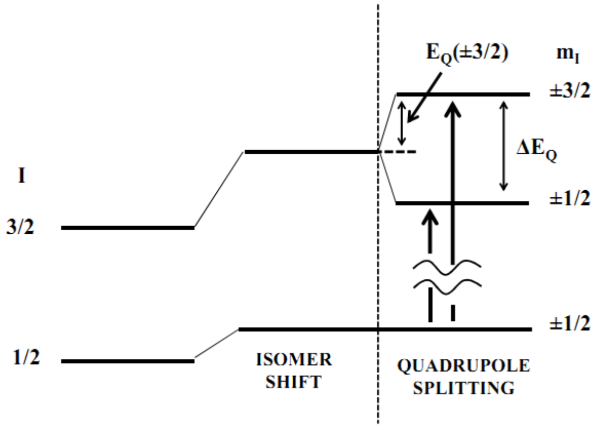

Figure 1.10: Splitting of energy levels of ^{57}Fe nucleus as a result of quadrupole interaction.

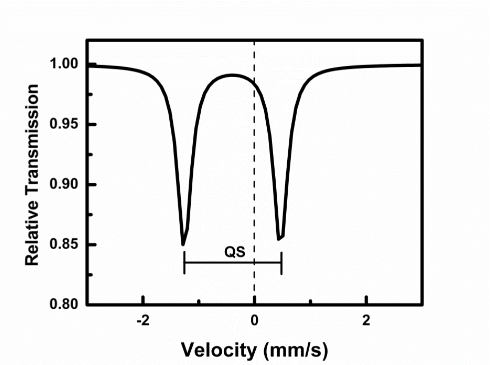

Figure 1.11: Quadrupole splitting of I=3/2 levels of ^{57}Fe resulting in the appearance of a doublet in a Mössbauer spectrum. The quadrupole splitting information determines the local symmetry of the Mössbauer atom.

The quadrupole splitting is given as

$$\Delta = \Delta E_Q \; c/E_o = \tfrac{1}{2} \; c/E_o \; eQV_{zz} \; (1 + \eta^2/3)^{1/2}$$

where Vzz is the principal component of EFG tensor, Q is the quadrupole moment and η is the asymmetry parameter given as $(V_{xx}-V_{yy})/V_{zz}$.

Magnetic dipole interaction and electric quadrupole interaction may be simultaneously present in certain cases. The perturbations are treated depending on their relative strengths. In the case of relatively weak quadrupole interaction the nuclear sublevels $|I,m_I>$ arising from magnetic dipole splitting are additionally shifted by the quadrupole interaction energies $E_Q(I, m_I)$; as a result, the sublevels of the excited I = 3/2 state are no longer equally spaced. The shifts by E_Q are upwards or downwards depending on the direction of the EFG. This enables one to determine the sign of the quadrupole splitting parameter ΔE_Q.

1.5.2 Atomic scale characterization of bulk spinel oxides using Mössbauer spectroscopy

Mössbauer spectra as obtained in the most common ferrite are shown in Fig 1.12. Out of 64 tetrahedral sites only 8 sites are occupied by Fe^{3+} while out of 32 octahedral sites only 16 sites are equally occupied by Fe^{3+} and Fe^{2+} cations. Hence the ratio of fraction of Fe atoms occupying A and B sites in the case of stoichiometric magnetite should be 2:1. Fe atoms occupying A and B sites experience magnetic hyperfine fields around 49 and 46 Tesla arising mainly due to superexchange interactions A-O-B as discussed earlier. The isomer shifts at A and B sites are deduced to be 0.35 mm/sec and 0.6 mm/sec. This is understood due to the presence of 8 numbers of Fe^{2+} along with the 8 numbers of Fe^{3+}, the effective valence at the octahedral B sites should be of the order of +2.5.

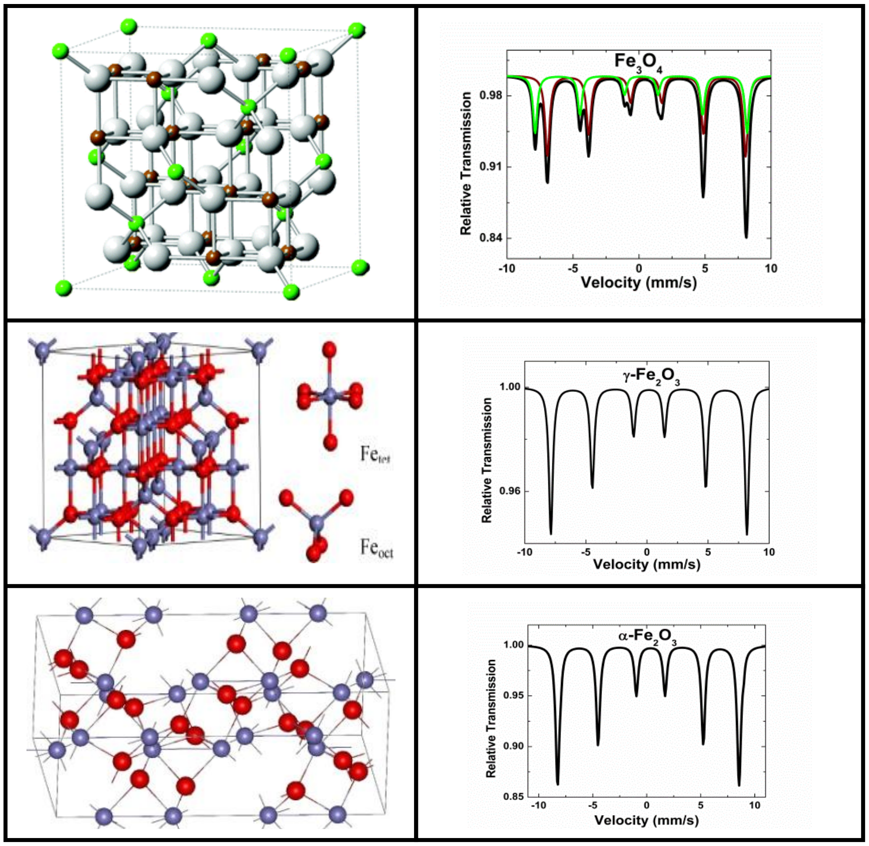

Figure 1.12: Schematics of unit cells of Fe_3O_4, γ-Fe_2O_3 and α-Fe_2O_3 along with their Mössbauer spectrum.

Magnetite if oxidized would result in the conversion to Maghemite with Fe^{2+} ➔ Fe^{3+}. This would further get oxidized to α-Fe_2O_3 [63].

1.5.3 Mössbauer spectroscopic studies on nanoparticles of magnetite

Mössbauer results obtained in a system composed of nanoparticles of Fe_3O_4 of different sizes have been presented here to illustrate the sensitivity of the technique to understand aspects related to structure and magnetic properties.

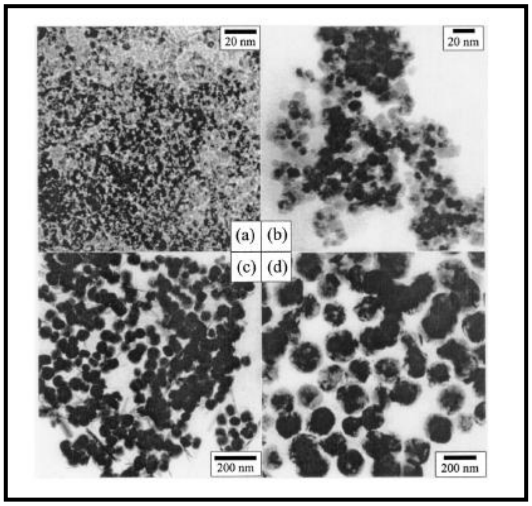

Figure 1.13: TEM micrographs of Fe_3O_4 nanoparticles of different size as mentioned [46]**.**

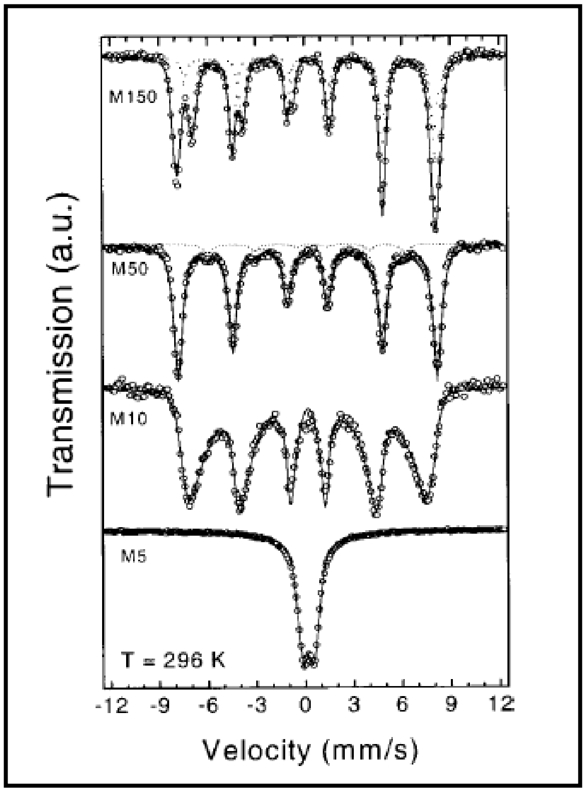

Figure 1.14: Mössbauer spectra obtained at 300 K in these nanoparticles of different size [46]**.**

Table 1.3. Mössbauer hyperfine parameters of Fe_3O_4 at RT of different particle size [46]**.**

Particle size (nm)	**site**	B_{hf} (T)	**Δ** (mm/s)	**δ** (mm/sec)	**f** (%)
5	--	---	0.6 (1)	0.2(1)	100 (3)
10	--	46	0 (1)	0.2(1)	100(3)
50	---	50	0(1)	0.2(1)	100 (3)
150	A	49.5	0.05(1)	0.2(1)	57(3)
	B	46.0	0.02(1)	0.64(1)	43(3)

The sensitivity of Mössbauer spectroscopy for studying the magnetic nanoparticles is illustrated here based on the results reported by Goya *et. al* [46]. Shown at Figure 1.13 are the TEM micrographs displaying the presence of magnetite nanoparticles of increasing size from (a)-(d). Mössbauer spectrum corresponding to particles of size less than or close to 5 nm is a doublet (Cf. Figure 1.14). This is understood to be due to superparamagnetic fluctuation of spins. By substituting the value of the anisotropy energy per unit volume K for magnetite as 10.5 J/m^3 [64] and the particle size to be 5 nm, the value of KV is seen to be close to that of kT at 300 K. This results in a very small time of fluctuation of spins τ as compared to that of the experimental observation time which is the lifetime of the isomeric state (10^{-7} sec). With increasing size of the nanoparticles the Mössbauer spectra evolve from a highly damped to a sharp sextet which could be de convoluted into two components with the Fe^{3+} atoms occupying both tetrahedral and octahedral sites while Fe^{2+} occupy octahedral sites.

Shown below are the Mössbauer spectra obtained in samples composed of nanoparticles of iron oxides of mean size 4, 12, 16 and 50 nm as deduced using XRD results. It is observed that the nanoparticles of mean size close to 5 nm exhibits a doublet at room temperature due to superparamagnetic relaxation. Spectrum corresponding to 12 and 16 nm is distinctly different with a much larger interaction between nanoparticles. With a decrease in the superparamagnetic fluctuation of spins, the contribution of disordered spins occupying the surface thus results in larger dampening effects in the case of 12 nm than that of 14 nm particle. Iron oxide particles of size close to 50 nm exhibit a Mössbauer spectrum similar to that of the bulk displaying almost same hyperfine parameters as that of the bulk (cf. Figure 1.15). Variation of the mean hyperfine parameters such as linewidth, isomer shift, quadrupole splitting and that of hyperfine fields with particle size are shown in the Figure 1.16. It is interesting to see that the variation of the mean hyperfine parameters match with that of the variation of coercivity.

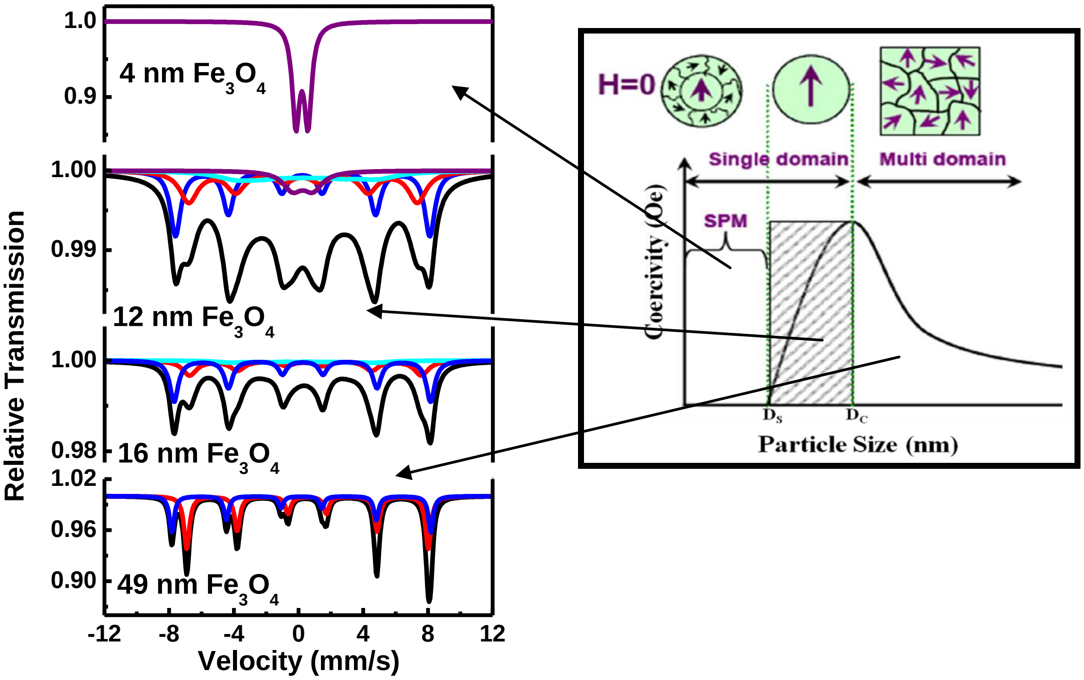

Figure 1.15: Mössbauer spectra with varying particle size of Fe_3O_4. Also shown is the variation of coercivity with particle size and the representative size dependent Mössbauer spectra are marked by means of arrows.

Mössbauer spectra are observed to be matching with that of the variation of coercivity up to the size corresponding to that of multi domain regime. ^{57}Fe resonant absorbers associated with iron oxide particles of size close to or less than 5 nm are seen to be exposed to a mean hyperfine field of 0 Tesla similar to that of zero coercivity which is understood to be due to superparamagnetic relaxation of spins. With increasing particle size there is an increase in the anisotropy energy as compared to that of the thermal energy. This results in an increase in the spin relaxation time and hence an increase in hyperfine field. With a further increase in particle size the area fraction associated with superparamagnetic doublet further decreases at the cost of nearly bulk. This is also associated with a decrease in the fraction of Fe atoms exposed to disordered spins. For particles of size beyond 25 nm the fraction of Fe atoms associated with disordered spins decrease almost to zero and the values of hyperfine parameters get restored as that of the bulk. As the Fe atoms are exposed to local field and these are not effective to interaction between domains, beyond certain size of the particles the hyperfine field becomes saturated and remains as constant and independent of size effect.

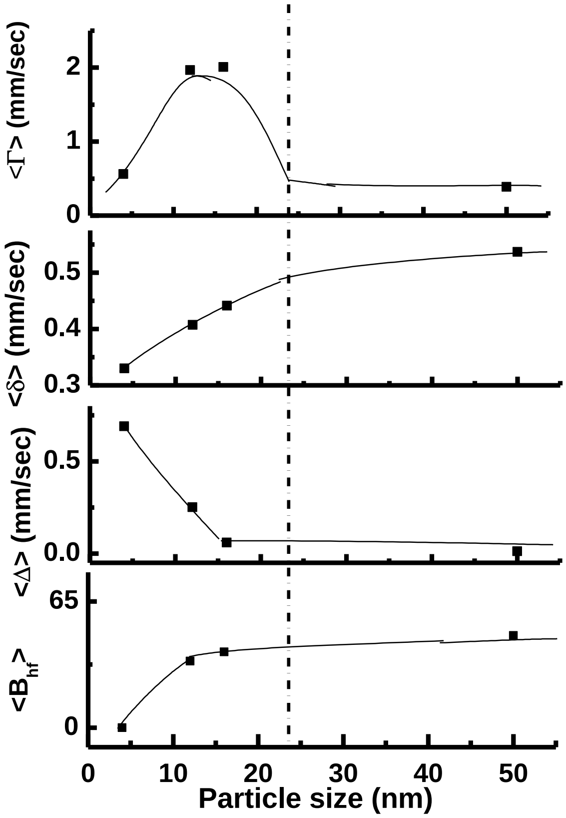

Figure 1.16: Variations of the mean values of hyperfine parameters with particle size as deduced from Mössbauer studies.

The variation of mean line width of Mössbauer spectrum exhibits an interesting change almost similar to that of coercivity with annealing temperature. When the particle size is of the order of 5 nm in the superparamagnetic regime, the linewidth is quite low. Fe absorbers associated with these particles in this size regime are exposed to zero hyperfine fields. While the size increases towards single domain particle there is a disordered spins at the surface which increases leading to an increase in the line width. This contribution increases with increasing size as more disordered spin configurations are possible. Also important are the interparticle interactions. These effects result in an increase in the mean line width. Beyond certain size of the particle the particle volume becomes sufficiently large compared to surface and the particles behave like bulk. Another important observation is an increase in the mean isomer shift with an increase in the particle size implying that below certain size of the particle the concentration of Fe^{2+} is smaller than that of the bulk. Finer aspects of the evolution of the spectra are explained in the following paragraph based on the discussion of the results obtained in the present thesis.

This result shows that the values of mean hyperfine field, quadrupole splitting and isomer shift exhibit interesting changes in the particle regime < 20 nm beyond which these parameters become constant. Line width signifying the distribution in the observed parameters such as mean hyperfine field and/or quadrupole splitting is small of the order of ≈ 0.5-0.7 mm/sec for a superparamagnetic particle. This is due to zero hyperfine fields due to superparamagnetic fluctuations and a unique quadrupole splitting. The zero hyperfine fields is caused by superparamagnetic fluctuation while the quadrupole splitting quadrupole splitting is understood to be due to an appreciable distortion plausibly caused by point defects such as cationic and anionic vacancies.

The distribution in linewidth exhibits a maximum is very small for the range of particles of size close to 5 nm. This is understood to be mainly due to the vanishing of magnetic interaction with the effective hyperfine field at the site of Fe becoming zero. This is consistent with the variation of coercivity as a function of particle size. Another important result is the increase in isomer shift with increasing particle size implying an increase in Fe^{2+} surface defects.

1.6 Overview of thesis

Several important issues related to iron based spinel ferrite nanoparticles oxides need to be understood completely [65,66].

i) Evolution of hyperfine parameters with increasing particle size. It is quite important to understand these aspects especially in particles of size less than 10 nm. A complete understanding of the aspects related to structure and magnetism of these particles is still lacking, though the effect of oxidation in the particles of size less than 10 nm has been reported which would result in an increase in the number of Fe^{3+} at the cost of Fe^{2+}. In particular the possible role of pint defects on these aspects needs to be understood.

ii) Role of surfactant in modifying magnetic interaction between nano particles and the effect of binding of nanoparticles by surfactant need to be understood for devising suitable functional assemblies. In this thesis a study iron oxide nanoparticles by oleic acid is carried out to understand the physics of the binding of NP of iron oxides with oleic acid.

iii) In order to enhance the stability of superparamagnetic nanoparticles it is required to bind the particles in a suitable template (depending upon the application envisaged) which can bind the particles very strongly. Such a study would result in an understanding of the binding of the particles in template and also the interactions between particles.

iv) Point defects aspects in nano magnetite. Also point defects aspects of nanoparticles resulting in for example ferromagnetic ordering in nano zinc ferrite. How it compares while we introduce defects in a bulk zinc ferrite.

Physics of local structure and magnetic properties of Fe based spinel ferrite nanoparticles related to the above mentioned issues would be studied in a detailed manner in the present thesis mainly using Mössbauer spectroscopy.

The thesis consists of seven chapters as briefly described below:

In this **Chapter 1**, the importance of ferrites in particular the nanoferrites for a wide range of applications including high dense magnetic memory, drug delivery is briefly introduced. A detailed literature survey on the magnetism of the ferrite nanoparticles with varying size and the utilization of hyperfine techniques in particular the Mössbauer spectroscopy to study local structure and magnetic properties are presented in this chapter.

Coprecipitation method of synthesis of nano ferritic particles has been explained along with the introduction to various characterization tools employed for investigating the structural and magnetic properties pertaining to the bulk iron based spinel ferrites are presented in **Chapter 2**. Experimental aspects of Mössbauer spectroscopy which is used as a main characterization tool have also been presented in chapter 2.

Atomic scale understanding of magnetite nanoparticles prepared through co precipitation method in terms of their local structure and magnetic properties along with the optimization of parameters for the synthesis of magnetite by coprecipitation. Nucleation and growth of magnetite from iron hydroxide phase has been presented in **Chapter 3** based on a systematic annealing carried out on sample containing iron oxyhydroxide and magnetite. **Chapter 4** presents the role of oleic acid surfactant in modifying particle-particle interaction, binding of oleic acid with different state of iron along with the physics behind the formation of core/shell of different polymorphs of iron oxide. **Chapter 5** illustrates the high thermal stabilization of the magnetite nanoparticles as bound in the zeolite template. The dipole-dipole interaction with respect to interparticle separation is discussed in a detailed manner. **Chapter 6** reports the understanding of the cationic distribution in the nanoparticles of off-stoichiometric magnetite and the redistribution of the cations as the particle size increases based on the Mossbauer results. The magnetism of $ZnFe_2O_4$ nanoparticles and the disappearance of ferromagnetism due to coarsening of the particles are discussed in a detailed manner based on the Mossbauer results. **Chapter 7** summarizes the results obtained in this thesis and in addition the scope for future work is provided.

1.7 References

[1] Snelling, E.C., *Soft ferrites: properties and applications*, 1988: Butterworth-Heinemann

[2] Y. Suzuki, *Annu. Rev. Mater. Res.* **31**, 265 (2001)

[3] G. Armelles, A. Cebollada, A. García-Martín, J. M. Montero-Moreno, M. Waleczek, and K. Nielsch, *Langmuir*, **28**, 9127 (2012)

[4] H. Mamiya, N. Terada, T. Furubayashi, H. S. Suzuki and H. Kitazawa, *J. Magn. Magn. Mater.*, **322**, 1561 (2010)

[5] Y. C. Sui, R. Skomski, K. D. Sorge and D. J. Sellmyer, *Appl. Phys. Lett.*, **84**, 1525 (2004)

[6] J.P. Parekh, *Electronics Letters*, **5**, 14 (1969)

[7] P. V. Kumar, M. P. Short, S. Yip, B. Yildiz and J. C. Grossman, *J. Phys. Chem. C*, **117**, 5678 (2013)

[8] M. Monti, B. Santos, A. Mascaraque, O. R. de la Fuente, M. A. Nino,T. O. Mentes, A. Locatelli, K. F. McCarty, J. F. Marco and J. de la Figuera, *Phys. Rev. B*, **85**, 020404(R) (2012)

[9] S.-C. Weng, Y.-Ru Lee, C.-G. Chen, C.-H. Chu, Y.-L. Soo and S.-L. Chang, *Phys. Rev. Lett.*, **108**, 146404 (2012)

[10] J. Garcia, G. Subias, M. G. Proietti, J. Blasco, H. Renevier, J. L. Hodeau and Y. Joly, *Phys. Rev. B*, **63**, 054110 (2001)

[11] A. Pratt, M. Kurahashi, X. Sun, D. Gilks and Y. Yamauchi, *Phys. Rev. B*, **85**, 180409(R) (2012)

[12] J. Blasco, J. Garcia and G. Subias, *Phys. Rev.* B, **83**, 104105 (2011)

[13] S.-C. Weng, Y.-Ru Lee, C.-G. Chen, C.-H. Chu, Y.-L. Soo and S.-L. Chang, *Phys. Rev. Lett.*, **108**, 146404 (2012)

[14] J. J. I. Wong, A. G. Swartz, R. Zheng, W. Han and R. K. Kawakami, *Phys. Rev. B*, **86**, 060409(R) (2012)

[15] M. S. Senn, I. Loa, J. P. Wright and J. P. Attfield, *Phys. Rev. B*, **85**, 125119 (2012)

[16] A. Tanaka, C. F. Chang, M. Buchholz, C. Trabant, E. Schierle, J. Schlappa, D. Schmitz, H. Ott, P. Metcalf, L. H. Tjeng and C. S.-Langeheine, *Phys. Rev. Lett.*, **108**, 227203 (2012)

[17] J. de la Venta, M. Erekhinsky, S. Wang, K. G. West, R. Morales and I. K. Schulle, *Phys. Rev. B*, **85**, 134447 (2012)

[18] T. Kołodziej, A. Kozłowski, P. Piekarz, W. Tabis, Z. Kakol, M. Zajac, Z. Tarnawski, J. M. Honig, A. M. Oles and K. Parlinski, *Phys. Rev. B,* **85**, 104301 (2012)

[19] M. Hoesch, P. Piekarz, A. Bosak, M. Le Tacon, M. Krisch, A. Kozłowski, A. M. Oles´ and K. Parlinski, *Phys. Rev. Lett.*, **110**, 207204 (2013)

[20] A. K. Gupta and M. Gupta, *Biomaterials*, **26**, 3995 (2005)

[21] L.-S. Zhong, J.-S. Hu, H.-Pu Liang, A.-M. Cao, W.-G. Song and Li-Jun Wan, *Adv. Mater.*, **18**, 2426 (2006)

[22] X. Gao, L. Liu, B. Birajdar, M. Ziese, W. Lee, M. Alexe and D. Hesse, *Adv. Funct. Mater.*, **19**, 3450 (2009)

[23] J. E. Lee, N. Lee, H. Kim, J. Kim, S. H. Choi, J. H. Kim, T. Kim, I. C. Song, S. P. Park, W. K. Moon and T. Hyeon, *J. Am. Chem. Soc.*, **132**, 552 (2010)

[24] Y.-M. Huh, Y.-w. Jun, H.-T. Song, S. Kim, J.-s. Choi, J.-H. Lee, S. Yoon, K.-S. Kim, J.-S. Shin, J.-S. Suh, and J. Cheon, *J. Am. Chem. Soc.*, **127**, 12387 (2005)

[25] R. Ghosh, L. Pradhan, Y. P. Devi, S. S. Meena, R. Tewari, A. Kumar, S. Sharma, N. S. Gajbhiye, R. K. Vatsa, B. N. Pandey and R. S. Ningthoujam, *J. Mater. Chem.*, **21**, 13388 (2011)

[26] M. Arruebo, R. F.-Pacheco, S. Irusta, J. Arbiol, M. R. Ibarra and J. Santamaria, *Nanotechnology*, **17**, 4057 (2006)

[27] J.-f. Liu , Z.-S. Zhao and G.-b. Jiang, *Environ. Sci. Technol.*, **42**, 6949 (2008)

[28] N. Karapinar, *Int. J. Miner. Process.*, **71**, 45 (2003)

[29] H. Kim, D.-H. Seo, H. Kim, I. Park, J. Hong, K.-Y. Park and K. Kang, *Chem. Mater.*, **24**, 720 (2012)

[30] Y. Tamaura and H. Kaneko, *Solar Energy*, **78**, 616 (2005)

[31] K. J. McDonald and K.-S. Choi, *Chem. Mater.*, **23**, 4863 (2011)

[32] D. Suk, D. R. Peacor and R. V. Voo, *Nature*, **345**, 611 (1990)

[33] P. D. Shima and J. Philip, *J. Phys. Chem. C*, **115**, 20097 (2011)

[34] Y. Tamaura, H. Kaneko, *Solar Energy*, **78**, 616 (2005)

[35] G. Zhou, D.-W. Wang, F. Li, L. Zhang, N. Li, Z.-S. Wu, L. Wen,G. Q. (Max) Lu and H.-M. Cheng, *Chem. Mater.*, **22**, 5306 (2010**)**

[36] S. Laurent, D. Forge, M. Port, A. Roch, C. Robic, L. V. Elst and R. N. Muller, *Chem. Rev.*, **108**, 2064 (2008)

[37] S. P. Gubin, Y. A. Koksharov, G. B. Khomutov and G. Y. Yurkov, *Russ. Chem. Rev.*, **74**, 489 (2005)

[38] W. L. Bragg and J. West, *Proc. R. Soc. Lond. A*, **114**, 450 (1927)

[39] R. W. Grimes, A. B. Anderson and A. H. Heuerg, *J. Am. Chem. Soc*., **111**, 1 (1981)

[40] C. R. Vestal and Z. J. Zhang, *J. Am. Chem. Soc*., **125**, 9828 (2003)

[41] An-Hui Lu, E. L. Salabas, and Ferdi Schmith, *Angew. Chem*. **46**, 1222 (2007)

[42] F. Bodker, M. F. Hansen, C. B. Koch, K. Lefmann, and S. Morup, *Phys. Rev. B*, **61**, 6826 (2000)

[43] A.H. Morrish,*The Physical Principles of Magnetism*, Wiley, New York (**1965**)

[44] E.C. Stoner, E.P. Wohlfarth, *Philos. Trans. R. Soc. A*, **240**, 599 (1948)

[45] Daliya S. Mathew, Ruey-Shin Juang, *Chem. Eng. J.*, **129**, 51 (2007)

[46] G. F. Goya, T. S. Berquo, F. C. Fonseca and M. P. Morales, *J. Appl. Phys.*, **94**, 3520 (2003)

[47] W. Eerenstein, T. T. M. Palstra, and T. Hibma, S. Celotto, *Phys. Rev. B*, **66**, 201101 (2002)

[48] J. S. Salazar, L. Perez, O. de Abril, L. T. Phuoc, D. Ihiawakrim, M. Vazquez, J.-M. Greneche, S. B.-Colin and G. Pourroy, *Chem. Mater*., **23**, 1379 (2011)

[49] S. A. Oliver, H. H. Hamdeh and J. C. Ho, *Phys. Rev. B*, **60,** 3400 (1999)

[50] J. F. Hochepied, P. Bonville and M. P. Pileni, *J. Phys. Chem. B*, **104**, 905 (2000)

[51] A. de Kergommeaux, J. F.-Vincent, A. Pron, R. de Bettignies, B. Malaman and P. Reiss, *J. Am. Chem. Soc.* **134**, 11659 (2012)

[52] I. Sergueev, L. Dubrovinsky, M. Ekholm, O. Yu. Vekilova, A. I. Chumakov, M. Zajac, V. Potapkin, I. Kantor, S. Bornemann, H. Ebert, S. I. Simak, I. A. Abrikosov and R. Ruffer, *Phys. Rev. Lett.*, **111**, 157601 (2013)

[53] H.-H. Klauss, H. Luetkens, R. Klingeler, C. Hess, F. J. Litterst, M. Kraken, M. M. Korshunov, I. Eremin, S.-L. Drechsler, R. Khasanov, A. Amato, J. Hamann-Borrero, N. Leps, A. Kondrat, G. Behr, J. Werner and B. Buchner, *Phys. Rev. Lett.*, **101**, 077005 (2008)

[54] R. D. Ellerbrock, A. Fuest, A. Schatz, W. Keune and R. A. Brand, *Phys. Rev. Lett.*,

74, 3053 (1995)

[55] C. Battistoni, J.L. Dormann, D. Fiorani, E. Paparazzo and S. Viticoli, *Solid State Commun.*, **39**, 581 (1981)

[56] G. A. Pirez Alcazar and E. G. da Silva, *J. Phys. F: Met. Phys.*, **17**, 2323 (1987)

[57] G. C. Papaefthymiou, E. Devlin, A. Simopoulos, D. K. Yi, S. N. Riduan, S. S. Lee and J. Y. Ying, *Phys. Rev. B,* **80**, 024406 (2009)

[58] A. Mochel, I. Sergueev, H.-C. Wille, J. Voigt, M. Prager, M. B. Stone, B. C. Sales, Z. Guguchia, A. Shengelaya, V. Keppens and R. P. Hermann, *Phys. Rev. B*, **84**, 184306 (2011)

[59] C. A. Gorski and M. M. Scherer, *American Mineralogist*, **95**, 1017 (2010)

[60] G. K. Wertheim, *Mössbauer Effect: Principles and Applications,* Academic press (New York), (1971)

[61] Bancroft, G. M., *Mössbauer spectroscopy: An introduction for inorganic chemists and geochemists,* Wiley (New York) (1973)

[62] N. N. Greenwood and T. C. Gibb, *Mössbauer Spectroscopy*, London (1971)

[63] W. Feitknecht and K. J. Gallagher, *Nature,* **228**, 548 (1970)

[64] B.D. Cullity, *Introduction to Magnetic Materials*, Addison-Wesley, Reading, MA, (1972).

[65] S. Ayyappan, S. P. Raja, C. Venkateswaran, J. Philip and B. Raj, *Appl. Phys. Lett*., **96**, 143106 (2010)

[66] J. Garcia and G. Subias, *Phys. Rev. Lett*., **109**, 049701 (2012)

CHAPTER 2

EXPERIMENTAL DETAILS

Chapter 2

Experimental details

2.1 Introduction

In this chapter the basics of co precipitation method of preparation of the nanoparticles of iron oxide such as magnetite and $ZnFe_2O_4$ is discussed. In addition the solid state method of preparation of bulk $ZnFe_2O_4$ is also presented. Details of XRD spectrometer and Transmission electron microscope employed in the thesis are discussed briefly. Bulk magnetization and the dynamics of magnetic particles have been studied using Vibration scanning magnetometry (VSM). Experimental aspects of Mössbauer spectroscopy, which has been used as the main characterization technique for studying the local structural and magnetic properties, have been presented in a detailed manner. In addition the details of the post annealing treatments employed on the samples for effecting stoichiometry and to study the stability aspects of the nanoparticles have been presented.

2.2 Preparation of nano particles of spinel ferrites by coprecipitation method

Magnetite nanoparticles have been prepared extensively using various chemical methods such as co-precipitation, hydrothermal, sol-gel, micelle method, thermal decomposition, mechanical milling, solvothermal, sonochemical and bacteria synthesis method [1-8]. Each method has its limitations with respect to varying degree of resultant mono dispersity of nanoparticles, co-existence of impurity phases, cost and synthesis at ecologically unfavorable condition. Among the various methods the co-precipitation method was adopted for the synthesis of nano ferrites in the present thesis. Co-precipitation method is ecofriendly and cost effective. Importantly co-precipitation does not result in the formation of any organic compounds or any toxic reagents as end products which need to be separated or filtered from the metal oxides like in various other synthesis methods of nanoparticles such as thermal decomposition, sol-gel and electrochemical route [9-11]. A disadvantage of coprecipitation method over thermal decomposition is the broad particle size distribution. The distribution in the size of nanoparticles as produced through co-precipitation can however be narrowed down by tuning the stirring speed, surfactant modification and growing in a template [12-14]. In this thesis work the co-precipitation method was adopted for the synthesis of nanoferrites. MFe_2O_4 (M = Fe and Zn) spinel ferrite nanoparticles were synthesized by precipitating metal ion salts (M^{2+} and Fe^{3+}) of appropriate stoichiometric proportions in an alkaline medium. For the synthesis of spinel ferrite nanoparticles, Fe^{2+} / Zn^{2+} and Fe^{3+} based salts such as $FeSO_4.7H_2O$ / $ZnCl_2$ and $FeCl_3$ respectively were used along with NaOH, 35 % HCl, H_2SO_4 and acetone procured from E-Merck were used. All the chemicals used were of GR grade pure and used without any further purification. Ultra high pure water was used for the synthesis. $FeSO_4.7H_2O$ / $ZnCl_2$ and $FeCl_3$ were weighed in the required molar proportion of 1:2. The solution of the required concentration obtained was precipitated to metal oxide using NaOH maintaining to a specific pH.

Drawing of the setup used for the preparation of nanoparticles using coprecipitation method is shown in Figure 2.1. Flowcharts of the procedures followed for co-precipitation and solid state reaction methods are shown in Figure (2.2 & 2.3).

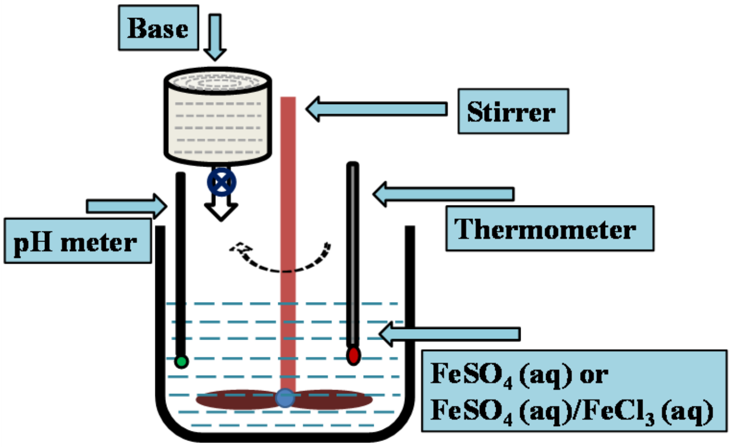

Figure 2.1: Drawing of the set up for the preparation of ferrite nanoparticles using coprecipitation

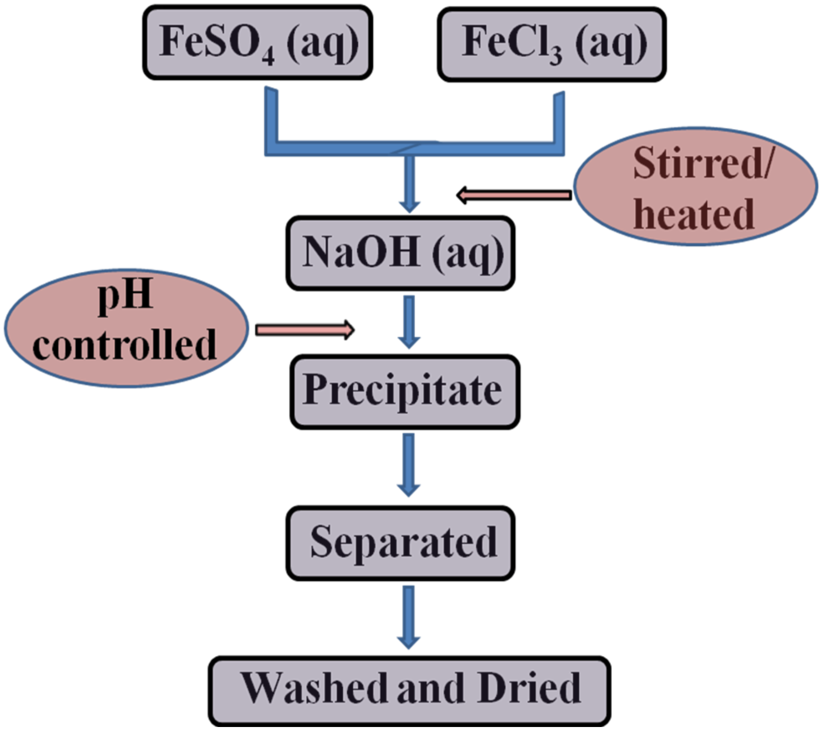

Figure 2.2: Flowchart of the procedure of Fe_3O_4 nanoparticle synthesis from Fe^{+2}/Fe^{+3} precursors.

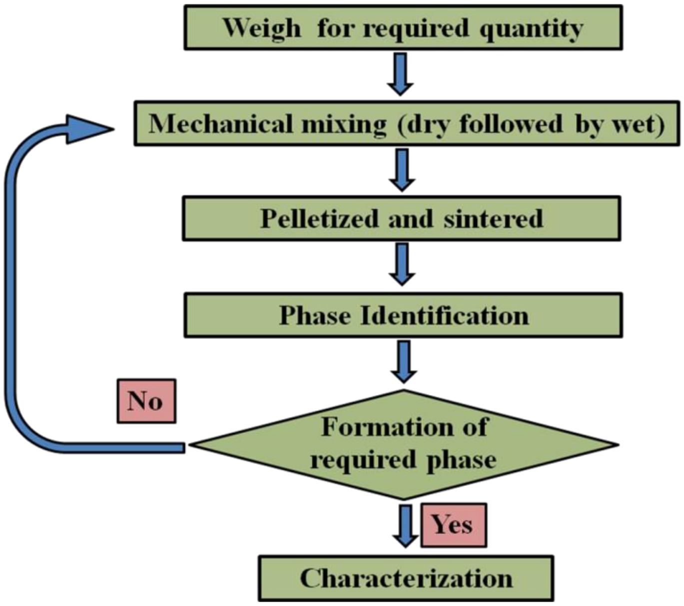

Figure 2.3: Flowchart for the synthesis using solid state reaction.

2.3 Preparation of bulk zinc ferrite by solid state reaction method

High pure ZnO and α-Fe_2O_3 (99.9 %) were taken in the molar ratio of 1 : 2 and was grounded using agate mortar to obtain homogenous mixture of the powders. The homogeneously mixed powder was pelletized and subjected to 1073 K for 8 h and then heated at 1473 K for 8 h. After cooling down to room temperature the annealed pellet was thoroughly grounded and heated to 1473 K for 5 h and cooled slowly to room temperature.

2.4 Techniques for structure and magnetic characterization

2.4.1 X-ray diffraction

Basic phase identification of nano ferrites were done using XRD performed with Cu K_α radiation of wavelength 1.5418 Å. Room temperature powder XRD patterns of samples were recorded using a computer controlled X-ray diffractometer (STOE, Germany). The diffractometer consists of flat pyrolitic graphite secondary monochromator that selects the Cu K_α (λ=1.5418 Å) radiation and NaI:Tl scintillation counter was used as a detector of scattered X-ray at different angles with respect to the angle of incidence. Si (911) single crystal was used as sample holder. The diffraction pattern was recorded in θ-2θ Bragg-Brentano geometry. Apart from the identification of phases present in the sample, the mean size of particles belonging to different phases have been deduced using Scherer formula after correction for instrumental resolution and strain broadening.

2.4.2 Transmission electron microscopy

Transmission electron microscope (TEM) of CM-200 make was operated at 200 kV to analyze the micro structure. Selective area and micro electron diffraction studies were conducted to obtain the information related to crystalline phase. A stream of electrons is obtained from an electron source and made to accelerate (100-300 kV) towards the sample in vacuum. The electron beam is confined and focused by using apertures and magnetic lenses. The interaction between electron beam and specimen generates elastic and inelastic scattering. The objective lens forms a diffraction pattern in the back focal plane. The diffraction technique is used to measure the spacing of the atomic crystalline lattice and determine the crystal structure. The crystalline lattice diffracts electrons to form bright spots on the viewing screen and the image consists of central bright spot surrounded by a series of reflected spots. The central bright spot represents undiffracted rays while the peripheral spots represent rays diffracted at various angles. The distance of the spots from the bright central spot is inversely proportional to the *d*-spacing of the crystalline lattice. For preparing TEM samples, a small quantity of the powder sample was ultrasonicated in methanol for 10 minutes. A single drop from the top of the suspension was then deposited on a carbon coated grid using a syringe and dried under infrared lamp to carry out the SAD and micro diffraction studies.

2.4.3 Vibrating Sample Magnetometer (VSM)

The VSM works on the principle of Faraday's law of electromagnetic induction. The sample is magnetized by a homogeneously applied magnetic field and is vibrated with respect to a stationary pick-up coil. The change in magnetic flux because of vibration of magnetized sample induces an emf in the pick-up coil. The induced emf V is proportional to the magnetic moment of the sample. In this work, the magnetization (M~H loop) measurements were done using a VSM (Cryogenics) up to a maximum field of ± 50 kOe at ambient and down to 4 K. The zero-field cooled (ZFC) and field-cooled (FC) magnetization were measured as a function of temperature in the range 4-300 K with different applied magnetic fields.

2.5 Local structure and magnetic properties using Mössbauer spectroscopy

Mössbauer spectrometer is mainly meant for deducing the shift or splitting of nuclear levels due to hyperfine interactions by Doppler shifting either source or absorber with a continuously varying velocity v and to look for the values of velocity at which there are resonant absorption of 14.4 keV gamma ray leading to minima in transmitted spectrum as the shift/ splitting ΔE becomes equal to $\Delta E = E_\gamma$ v/c. Block diagram of a Mössbauer spectrometer is shown in Figure 1. The spectrometer mainly consists of a Mössbauer drive unit, detector set for 14.4 keV gamma ray which is energized by a high voltage bias supply, preamplifier, amplifier and a Multichannel analyzer operated in Multi Channel Scaling mode. Mössbauer source is mounted on a drive which could be moved with a continuously varying velocity between zero and a preset value v. The slope of the v-t waveform (i.e.) acceleration is constant referred to as constant acceleration mode as shown as inset in Figure 2.4. The velocity changes from -v to +v in a half cycle (T/2 seconds). The analogue output from the function generator is applied to power amplifier, which drives the source. The output from the function generator is applied to the Multichannel analyzer (MCA) to provide synchronization and channel incrementing in multi channel scaling (MCS). Correspondence between the channel numbers and the velocity of the drive is established through Doppler equation.

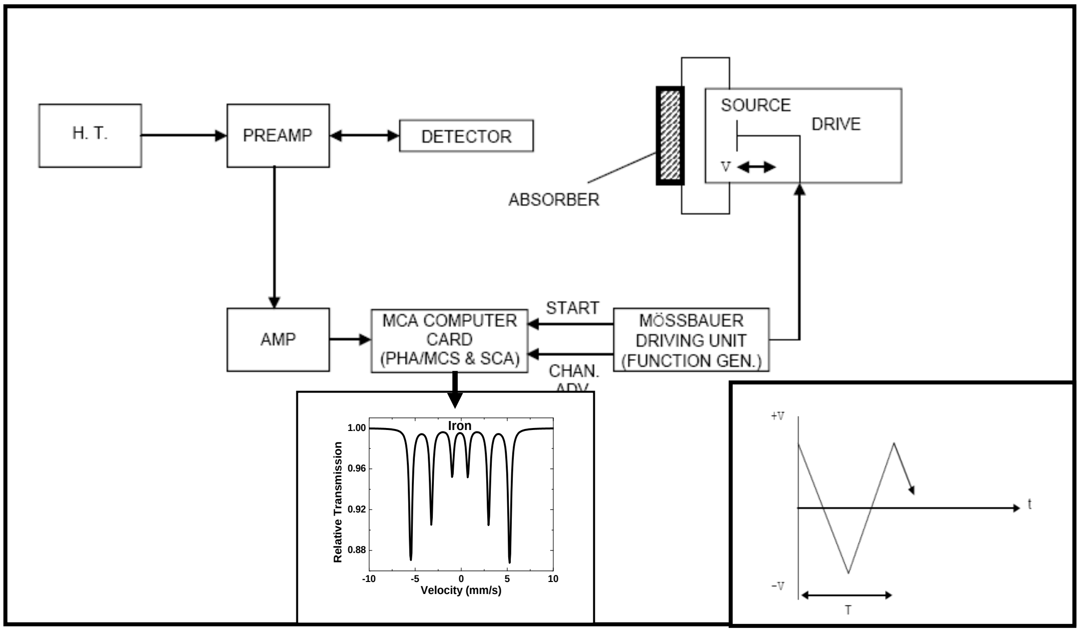

Figure 2.4: Schematic of Mössbauer spectrometer.

The source velocity is controlled by a transducer with a constant acceleration mode. A waveform generator sends a reference waveform (either triangular or sine) to the drive amplifier through a digital to analog converter. This signal is sent to the vibrator where it is converted to a mechanical oscillation of the drive shaft and source. Feedback signal is provided by a small coil within the vibrator to correct any deviations from the reference waveform. Gas filled proportional counter is used a detector of gamma rays.

From the detector pulse after amplification, 14.4 keV γ photons have been selected using energy discrimination by single channel analyzer. The digital logic pulses from single channel analyzer are fed as input to MCA and counted at different Doppler velocity. Thus a Mössbauer spectrum in terms of the intensity of the transmitted gamma rays through an absorber versus the velocity of the source i.e., Doppler shifted gamma energy is obtained.

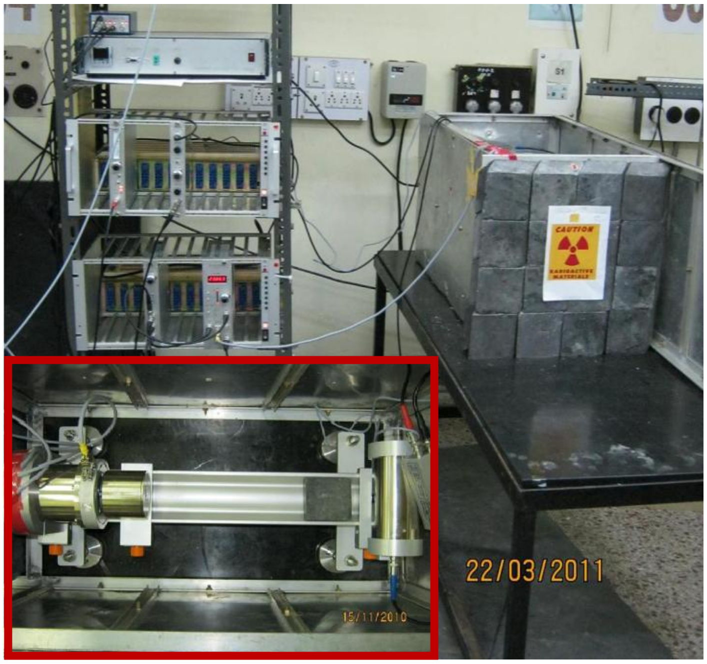

Figure 2.5: Photograph of Mössbauer spectrometer (made by Wissel, GmbH) showing the NIM bin in which modules corresponding to waveform generator, Mössbauer drive unit, High voltage power supply and linear amplifiers are housed. Inset shows the vibration free platform in which the shielded source mounted transducer, sample and proportional counter are mounted tightly.

The detector counts and source velocity are synchronized using a microprocessor system. The counts are accumulated in 1024 channels for one complete cycle, which contain two complete spectra viz., one for positive and another for negative acceleration of the source. As the acceleration is constant the time interval is equal for all velocity channels, hence each channel records for the same amount of time. During analysis the full spectrum acquired over positive and negative acceleration of source is folded around a center point to obtain a single spectrum. This increases the statistics of the data.

Brief description of the components and fundamentals are as follows:

2.5.1 Mössbauer Source

^{57}Co dispersed in Rh matrix is used as the Mossbauer source. The decay scheme of ^{57}Co isotope is shown in Figure 2.6. The half-life of ^{57}Co is 271.7 days and decays by electron capture to I = 5/2 excited state of ^{57}Fe. This is followed by a subsequent de excitation to I = 3/2 level, which is the isomeric state of interest for the Mössbauer effect. The excited state is characterized by a mean lifetime of 10^{-7} seconds and decays to ground state with I = ½. The excited state with I=3/2 is characterized by magnetic and quadrupole moments as 0.153 nm and 0.29 barn respectively. While the ground state with I=1/2 is characterized by magnetic and quadrupole moments as 0.093 nm and 0 barn respectively. The 14.41 keV state decays to the ground state by gamma-ray emission or internal conversion of the nuclei at I = 3/2. The ratio of these two decay rates is given by the equation $\alpha = N(e)/N(\gamma)$, where $N(e)$ and $N(\gamma)$ are the probability of radiative and non-radiative emission respectively. For ^{57}Fe internal conversion or non-radiative emission is 8.21 times more probable than photon emission. Based on the half-life of the 14.41 keV excited state (*i.e.)* 97.8 ns, the natural linewidth is deduced to be around 0.097 mm/s. The linewidth of a resonant emission and absorption event is thus 0.194 mm/s in perfect conditions [15].

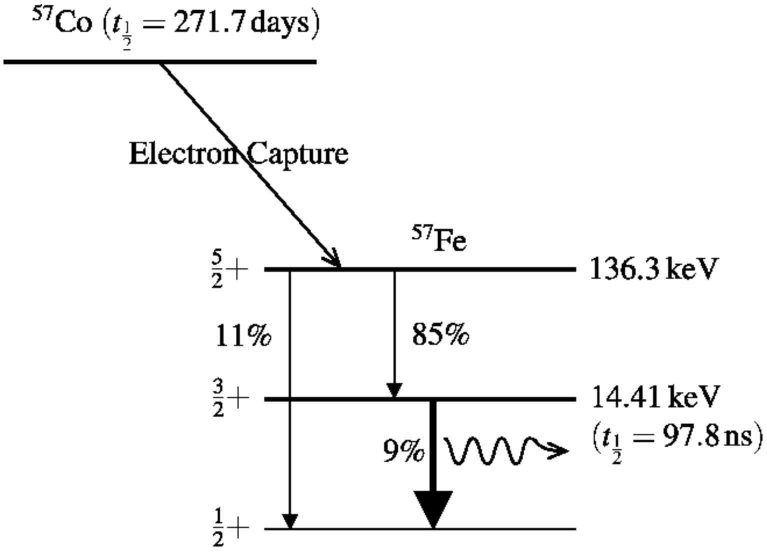

Figure 2.6: ***Decay scheme for a ^{57}Co source leading to gamma-ray emission. Internal conversion accounts for the remaining 91 % of 14.41 keV events.***

^{57}Co atoms diffused rhodium foil which provides a non-magnetic and cubic matrix is used as a Mössbauer source. Thus the ^{57}Co atoms occupying substitutional and defect free sites in Rh matrix provides a solid environment with a high recoil-free fraction produce mono-energetic gamma-rays. Specific activity of the source is 50 mCi.

2.5.2 Samples for Mössbauer measurements, Absorber thickness

Roughly 20 mg of powder samples of iron based bulk / nano ferrites are spread on to a cellophane tape to an area of 1 cm^2 to result in an absorber thickness ρt mentioned in the units of gm/cm^2. Resonance absorption is maximum for an optimal thickness of the absorber leading to a minimum value of linewidth. A linewidth of 0.28 mm/sec is obtained with a 10 µm thick Fe absorber. This is covered with a thin Al foil while carrying out measurements below 300 K. Mössbauer studies on samples constituting high Z elements were carried out by means of dispersing the sample in boron nitride.

2.5.3 Mössbauer Drive system

The drive system consists of the Mössbauer drive unit and a velocity transducer. It provides a precise motion of the γ-source for the measurement of the Mössbauer effect. The drive unit feeds the velocity transducer with an electronically controlled voltage. The waveform for the source motion is given by the function generator's reference signal. Drive unit and the transducer form a feedback system which minimizes the deviation of the actual source motion from its correct value. The drive system is suitable for desired waveform; however the best results are yielded with a sinusoidal waveform.

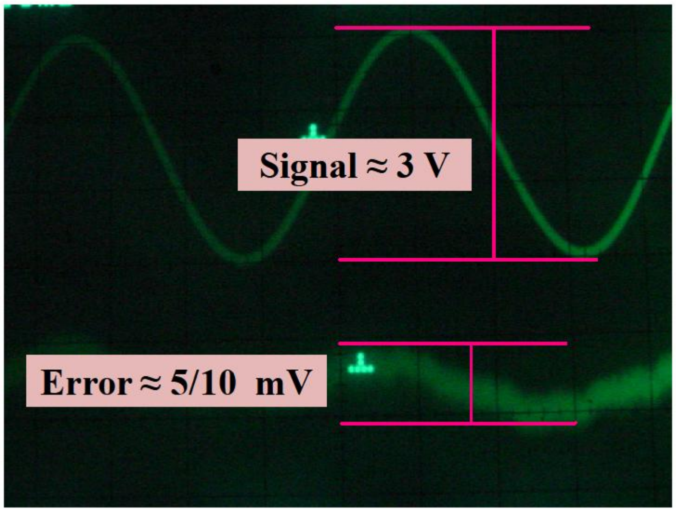

Figure 2.7: Input signal vs error of the waveform.

Shown in Figure 2.7 are the waveform of the drive unit and the error signal amplified by 10 times. These signals are of amplitude 3 V and 2.5 mV respectively indicating that the signal / noise ratio is of the order of 10^4.

2.5.4 Detector

The detector is a proportional counter filled with a gas consisting of 90% of Ar and 10% of Methane. Detector is energized by a bias of 1700 V to obtain the pulse. This is amplified and the output of the amplifier is fed to CMCA. Complete pulse height spectrum as obtained in the gas filled proportional counter is shown in Figure 2.8.

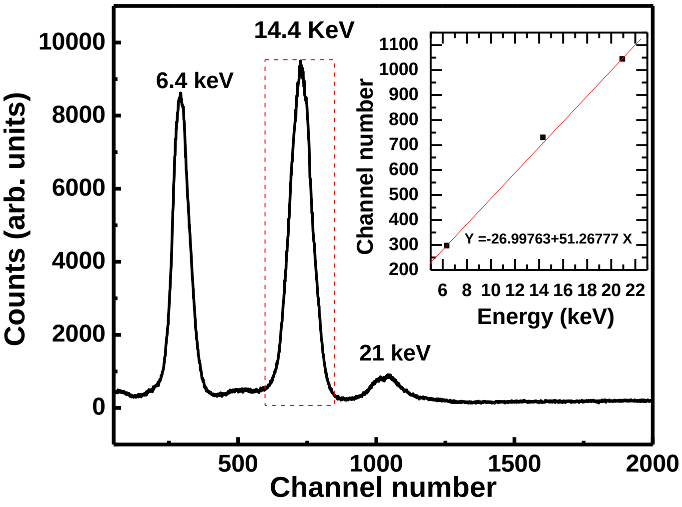

Figure 2.8: Pulse height spectrum obtained with ^{57}Co source dispersed in Rh matrix using a gas filled proportional counter. Three peaks are shown which are 6.4 keV K-xray of daughter nucleus ^{57}Fe, 14.4 keV γ ray of ^{57}Fe and 21 keV Rh – x ray peak. Inset shows the linearity in the variation of channel number with energy for a fixed bias supply of the detector.

The pulse magnitude from the detector is directly proportional to the gamma-ray energy and is sorted by a single channel analyzer after amplification. This allows the selection of the Mössbauer gamma-ray from any other radiation emitted from the source.

The detector counts and source velocity are synchronized by a microprocessor system. The counts accumulate in 1024 channels for one complete cycle, which contain two complete spectra: one for positive acceleration and one for negative acceleration of the source. As the acceleration is constant with the time interval equal for all velocity intervals counts are acquired in each channel for the same amount of time. During analysis the full spectrum is folded around a center point to produce a single spectrum. This increases the number of counts and flattens the background profile produced by the difference in intensity of the source radiation as the source moves relative to the absorber and detector. The detector is observed to be in a stable operating condition as verified by means of pulse height spectra acquired in between Mössbauer data acquisition.

2.5.5 Data analysis and deduction of hyperfine parameters

The Mössbauer spectra were fitted using WinNormus-for-Igor (version 3.0). Fitting involves finding out the positions, width and intensities of a number of Lorentzian lines so that these when superimposed give the best fit to the observed envelope. The program iterates to achieve the optimum values of the Mössbauer parameters (i.e. width (Γ mm/s), isomer shift (δ mm/s), quadrupole splitting (Δ mm/s) and B_{hf} (T)) using nonlinear optimization with least-squares statistics (a χ^2 model) [16]. The fitted parameters with $1 \leq \chi^2 \leq 1.5$ were taken into account.

2.5.6 Calibration

To analyze the recorded spectra the spectrometer needs to be calibrated. The three main calibration parameters are the velocity scale, the center point of the spectrum and the linearity of the velocity/time profile of the oscillation compared to a standard reference.

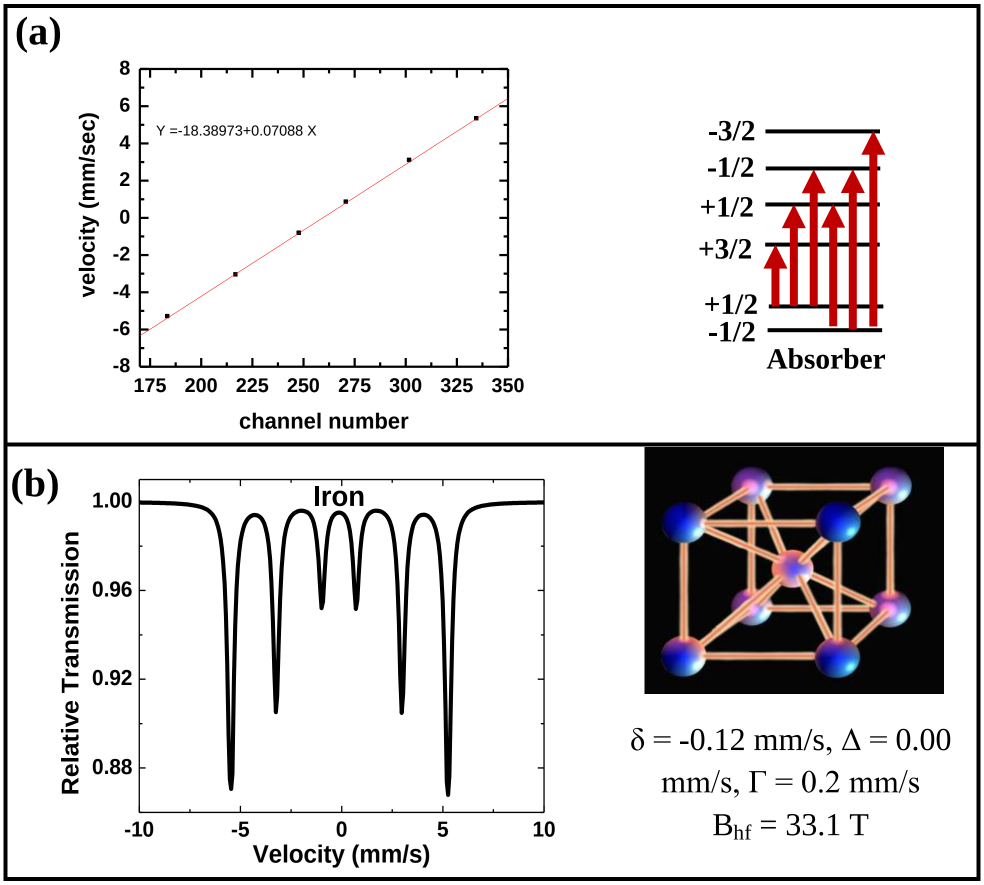

Figure 2.9. (a) Variation of velocity and channel number corresponding to the positions of resonant absorption peaks as deduced from the Mössbauer spectra of α-Fe [17]. (b) Mössbauer spectrum of α-Fe taken at room temperature, also shown are the cubic crystal structure of α-Fe and the hyperfine parameters derived by the analysis.

The calibration is performed using a spectrum recorded from 10 µm thick α-iron foil at room temperature (cf. Figure 2.9).

The velocity scale is calibrated using the well defined line positions of the sextet from α-iron, which occur at $\pm 5.312\ ^{mm}/_{s}$, $\pm 3.076\ ^{mm}/_{s}$ and $\pm 0.840\ ^{mm}/_{s}$ [17]. The peak channels corresponding to the above line positions of sextets of α-Fe in terms of velocities are obtained and are shown in Fig 2.9a. The center of this α-iron spectrum at room temperature is taken as the reference point ($0.0\ ^{mm}/_{s}$) for isomer shift values of sample spectra. The values of isomer shifts presented in this thesis henceforth are given with respect to that of α-Fe absorber at 300 K.

2.5.7 Cryostat

The cryostat used for the low temperature Mössbauer spectrometer is the model MBBC-HE0106. It is a top-loading bath cryostat with an exchange gas sample chamber. A photograph showing the front view of the cryostat is presented in Figure 2.10. The cryostat can be operated either with liquids of helium or nitrogen depending upon the requirement. In the helium operation mode, both, liquid helium and liquid nitrogen are used as cooling agents.

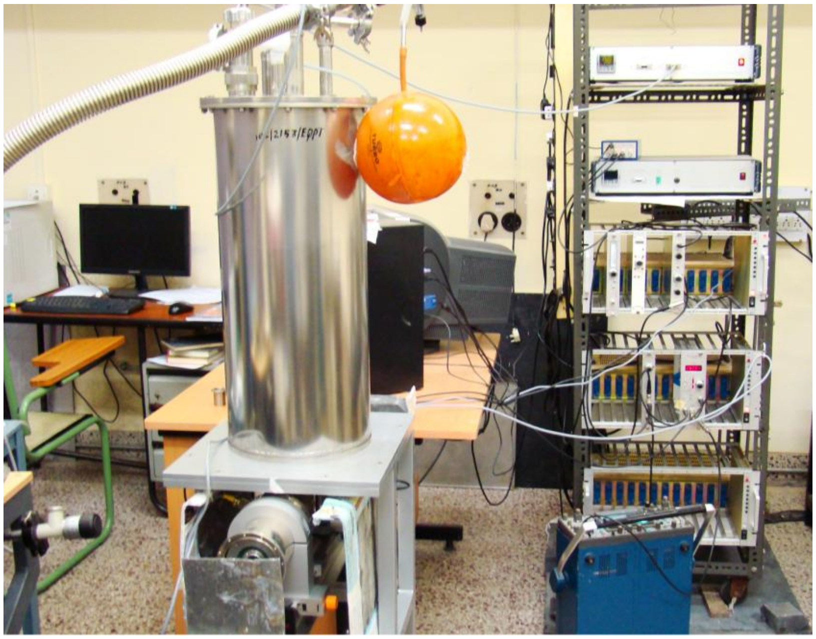

Figure 2.10: Photograph of Mössbauer spectrometer showing the Low temperature set up.

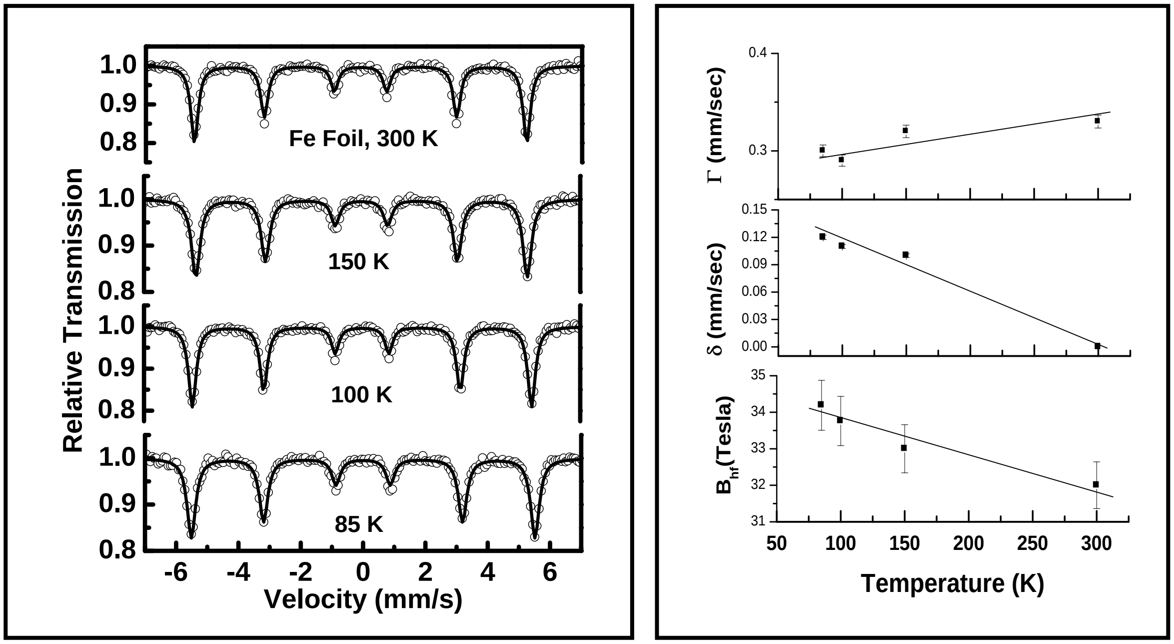

Figure 2.11: Mössbauer spectra of Fe foil obtained at different temperatures (left) and the variation of hyperfine parameters at different measurement temperatures (right).

The sample holder consists of a rectangular copper plate with a cylindrical hole of diameter d = 20 mm. For a better thermal contact, exchange gas is blown into the central tube through the input/output exchange gas tube. These windows are made of 0.1 mm thick aluminized Mylar with the absorptivity of 14.4 keV γ-rays to less than 1 %. The Mössbauer spectra obtained in 10 μm thick α-iron foil is shown in Figure 2.11. The hyperfine parameters of the spectra at various temperatures match very well with the reported results. A decrease in the linewidth concomitant with the increase in the values of center shift (δ) hyperfine field (Bhf) is observed. Increase in hyperfine field is understood to be due to an increase in the spin ordering based on Heisenberg exchange interaction model while the increase in center shift is due to an increase in the value of second order Doppler shift.

2.5.8 Application of an external magnetic field

Mössbauer measurement under the application of an external magnetic field helps in resolving the occurrence of phase(s) exhibiting ferrimagnetic ordering with the co-existing antiferro/ ferro magnetically ordered phases. Also Mössbauer study on the magnetically ordered nanoparticles under external magnetic field would be helpful to understand the interaction between nanoparticles besides resolving the disordered spin structure at the surface of the nanoparticles. Mössbauer measurements under the application of external magnetic field are carried out by sand witching the sample in between two ring magnets of 0.3 T as demonstrated in Figure 2.12. The magnets were arranged such that the direction of magnetic field lies parallel to the γ-rays. For a thin absorber the direction of hyperfine fields are in general randomly oriented with respect to γ-ray direction of propagation. If θ is the angle between direction of magnetic field at the nucleus and the γ ray direction, the intensity and hence the relative area under the six lines give information regarding the degree of alignment of the hyperfine field with the external magnetic field.

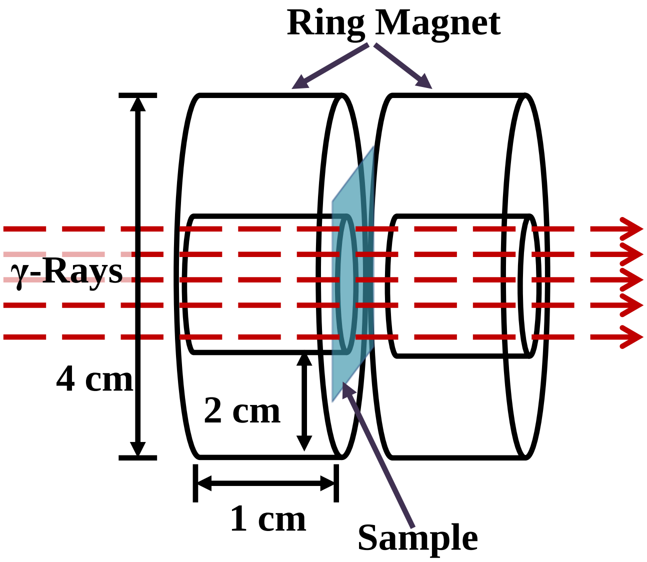

Figure 2.12: Configuration of magnet and magnetic field for the Mössbauer spectra acquisition.

$$A_{1,6} = 3(1+\cos^2\theta)$$

$$A_{2,5} = 4\sin^2\theta$$

$$A_{3,4} = (1+\cos^2\theta)$$

where $A_{i,j}$ is the area of line i or j. In the presence of an external magnetic field B_{ext} parallel to the gamma ray direction, for a thin Mössbauer absorber with a direction of hyperfine field is at random with respect to γ- direction of the beam the relative area Zeeman sextet are in the ratio 3:2:1:1:2:3. If the external field is very strong to completely polarize the spins the intensities of lines 2 and 5 vanish. While the external field is not so strong to completely polarize the canted spins the intensities will be in the ratio 3:p:1:1:p:3 with the value of p is given as

$p = 2 \sin^2\theta / (1+ \cos^2\theta)$.

Effective field at the nucleus $\overrightarrow{\mathbf{B}}_{efc} = \overrightarrow{\mathbf{B}}_{hf} + \overrightarrow{\mathbf{B}}_{ext}$

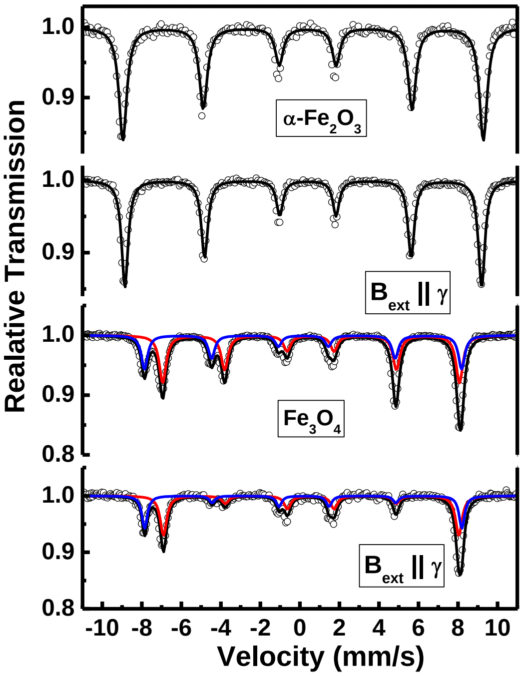

Figure 2.13: Mössbauer spectra with the application of an external magnetic field 0.28 Tesla applied parallel to the γ direction in the case of an antiferromagnetic and ferromagnetic system.

It can be seen that the external magnetic field could not influence the antiferromagnetically ordered spins of α-Fe_2O_3 (cf. Figure 2.13). While in the case of Fe_3O_4 the value of p tends to become zero for Fe_3O_4 particles of size close to 40 nm.

2.6 Post annealing treatments of chemically synthesized ferrites

Various heat treatment of the sample was carried out using a tubular furnace which can be operated up to a maximum temperature of 1373 K. Depending upon the problem of interest the samples have been annealed either at a partial pressure of 10^{-3} mbar or 10^{-6} mbar and the Mössbauer measurements have been carried out at 300 K. In certain systems depending upon the problem of interest Mössbauer measurements have been carried out in the temperature interval 300 – 80 K.

2.7 Summary

In this chapter experimental details including the synthesis of nanoparticles of spinel oxides using coprecipitation and bulk ferrite such as $ZnFe_2O_4$ using solid state reaction methods have been discussed. Basic details pertaining to techniques such as XRD, TEM and VSM employed for characterization of bulk crystalline structure, microstructure and magnetization respectively have been discussed. Details of Mössbauer spectrometer and experimentation at low temperature 300-80 K and under the application of external magnetic field have been presented. Performances of the Mössbauer spectrometer in terms of a very high value of signal to error voltage, a good linearity of the velocity drive are established.

2.8 References

[1] S. K. Suh, K. Yuet, D. K. Hwang, K. W.n Bong, P. S. Doyle and T. Alan Hatton, *J. Am. Chem. Soc.*, **134**, 7337 (2012)

[2] Xiaohong Sun, Chunming Zheng, Fuxiang Zhang, Yali Yang, Guangjun Wu, Aimin Yu, and Naijia Guan, *J. Phys. Chem. C*, **113**, 16002 (2009)

[3] K. Woo, H.J. Lee, J.-P. Ahn, Y.S. Park, *Adv. Mater*., **15**,1761 (2003)

[4] Y. Lee, J. Lee, C. J. Bae, J.-G. Park, H.-J. Noh, J.-H. Park, T. Hyeon, *Adv. Func. Mater*., **15**, 503 (2005)

[5] G. F. Goya, *Solid State Commun*., **130**, 783 (2004)

[6] Jian Lu, Xiuling Jiao, Dairong Chen and Wei Li, *J. Phys. Chem. C*, **113**, 4012 (2009)

[7] A.-L. Morel , S. I. Nikitenko, K. Gionnet, A. Wattiaux , J. Lai-Kee-Him , C. Labrugere , B. Chevalier, G. Deleris, C. Petibois ,A. Brisson and M. Simonoff, *ACS Nano*, **2**, 847 (2008)

[8] R. Prozorov, T. Prozorov, S. K. Mallapragada, B. Narasimhan, T. J. Williams, D. A. Bazylinski, *Phys. Rev. B*, **76**, 054406 (2007)

[9] N. s. Baik, Go Sakai, N. Miura and N. Yamazoe, *J. Am. Ceram. Soc*., **83**, 2983 (2000)

[10] L. Yan, J. Zhuang, X. Sun, Z. Deng and Y. Li, *Mater. Chem. Phys*., **76**, 119 (2002)

[11] T. P. Gbatu, O. Ceylan, K. L. Sutton, J. F. Rubinson, J. A. Caruso and H. B. Mark Jr, *Anal. Commun.* , **36**, 203 (1999)

[12] R. Massart, E. Dubois, V. Cabuil, E. Hasmonay, *J. Magn. Magn. Mater*., **149**, 1(1995)

[13] S. Sun and Hao Zeng, *J. Am. Chem. Soc.*, **124**, 8204 (2002)

[14] S. Alam, C. Anand, K. Ariga, T. Mori and Ajayan Vinu, *Angew. Chem*., **21**, 7494 (2009)

[15] J.G. Stevens and V.E. Stevens, editors. *Mössbauer Effect Data Index*. IFI/Plenum, New York, 1975

[16] R.E. Vandenberghe, E. De Grave and P.M.A. de Bakker, *Hyp. Int*., **83**, 29 (I994)

[17] J.G. Stevens, V.E. Stevens, and W.L. Gettys., *Mössbauer Effect Reference and Data Journal*, 3:99, 1980

CHAPTER 3

ATOMIC SCALE CHARACTERIZATION OF MAGNETITE NANOPARTICLES AS SYNTHESIZED THROUGH COPRECIPITATION METHOD

Chapter 3

Atomic scale characterization of magnetite nanoparticles as synthesized through coprecipitation method

3.1 Introduction

Variation of coercivity with particle size spanning from single domain to multi domain is shown in Figure 1.4. In the coprecipitation method of preparation of nanoparticles the particle size can be very well tuned by adjusting the pH, ionic concentration, temperature and stirring speed of the solution during synthesis [1,2]. The net surface charge and the sign of iron oxide particles depend on the pH of the medium. The pH where the surface charge becomes zero is known as point of zero charge (PZC). As the pH > PZC, the surface charge becomes negative whereas at lower pH the surface gets positively charged. At fixed ionic strength (I) imposed by the medium, the magnitude of the surface charge (σ) increases with increasing $\Delta pH = |pH - PZC|$ upto a maximum value σ_{max}. For constant pH, σ varies with I through a screening effect between charged sites which depends on the size, charge and concentration of the counter ions balancing the surface charge of the particles [1]. The surface charge of the nanoparticles enhances their interaction with the water molecules. Through the screening effect as due to interaction with surface and water, the structure and size of the nanoparticles can be tuned. Therefore at fixed I, particle size decreases as pH increases and vice versa as shown in Figure 3.1 [1,3]. The mechanical agitation as a result of stirring, controls the rate of nucleation which directly tunes the particle size. An increase in the crystallite size was observed for ferrites as precipitation temperature increases [4,5]. Many issues related to point defects affecting the local structure and magnetic properties of ferrites due to an enhanced surface to volume are yet to be understood.

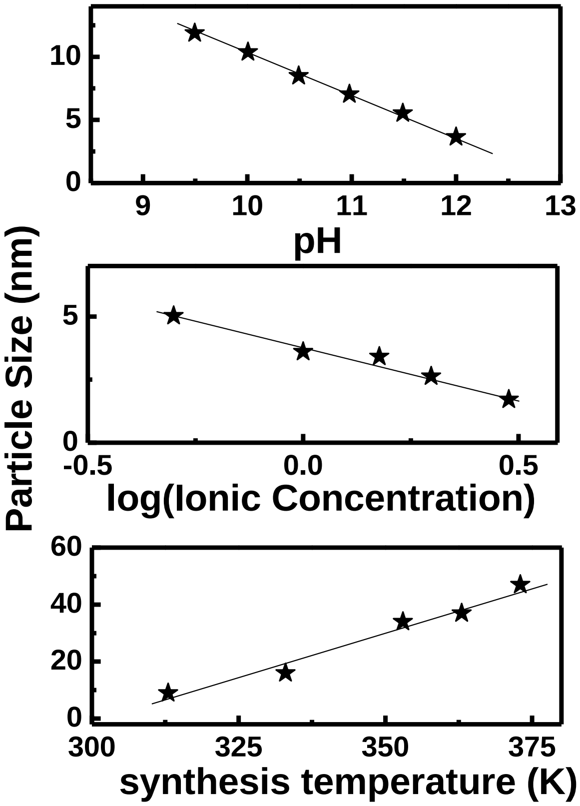

Figure 3.1. Variation of the size of ferrites nanoparticles with respect to pH [1]***, ionic concentration*** **[**1**]** ***of NaOH added precursor solution and the temperature*** [2] ***at which the solution was annealed while synthesizing ferrite particles using co-precipitation method.***

This chapter deals with the atomic scale characterization of nanoparticles of iron oxides produced by coprecipitation method. This is done by means of adjusting some of the experimental parameters such as stirring speed, temperature of the Fe^{3+}/Fe^{2+} precursor's solution to obtain magnetite particles of different size. Also discussed is the evolution of local structure and magnetic properties of these particles due to coarsening caused by controlled annealing treatments.

3.2 Synthesis of magnetite nanoparticles using co-precipitation method

Synthesis of magnetite nanoparticles was carried out using coprecipitation method, the details of which are explained in section 2.2. The parameters maintained in the synthesis are listed in table 3.1.

Table 3.1. Parameters maintained during synthesis of magnetite nanoparticles labeled as M1, M2 and M3

Parameters	Fe^{+2} / Fe^{+3} precursors		
	M1	M2	M3
Fe^{+2} conc. (Mol/l)	0.5	0.5	0.5
Fe^{+3} conc. (Mol/l)	1	1	1
Initial Ph	2	3.5	3
Final Ph	10	10	10
Synthesis Temp (K)	343	343	298
Stirring Speed	1200	1000	800
Stir. time bef. base add. (min)	20	30	20
Stir. time aft. base add. (min)	75	60	60
Drying Temp. (K)	373	373	373
Drying time (h)	6	6	6

The corresponding XRD spectrum of the as prepared magnetite using Fe^{3+}/Fe^{2+} precursors are shown in Figure 3.2. XRD spectrum of M1 can be indexed with cubic spinel oxide either maghemite and/or magnetite having space group Fd3m [6]. Close observation of the spectrum shows broad peaks matching with that of α-FeOOH. Goethite (α-FeOOH), a main intermediate phase of magnetite has an orthorhombic crystalline structure having space group Pnma with each Fe^{3+} ion surrounded by six oxygen ions forming an octahedron [7]. Two octahedra are linked through weak hydrogen bonding that causes distortion of octahedral linking that breaks long range coherency between crystal planes. Hydroxyl bonds form zig-zag chains between oxygen planes.

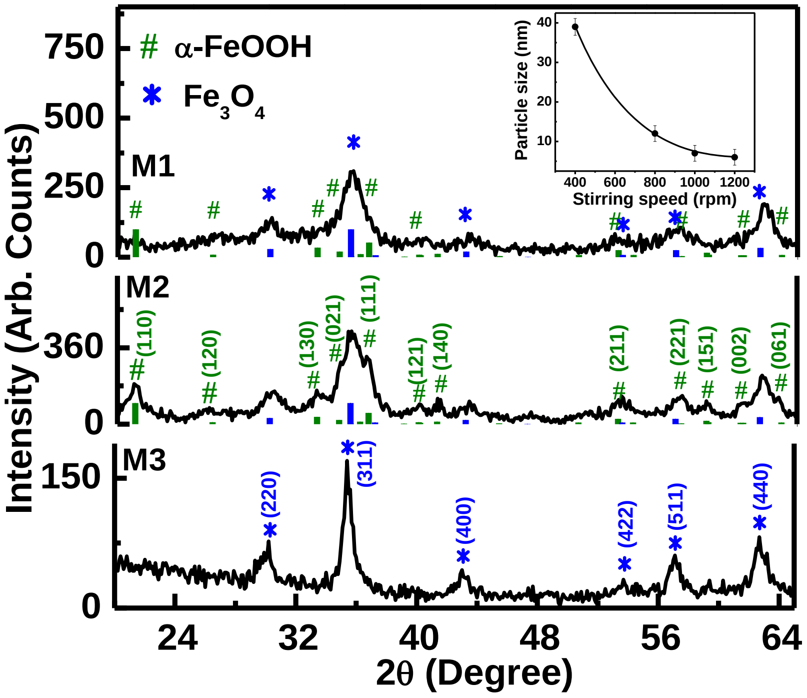

Figure 3.2: XRD of the as prepared Magnetite M1, M2, and M3. Particle size variation with respect to the stirring speed during synthesis is shown as inset.

These flexible hydrogen bonds stabilize the structure by accommodating internal stress though there is a loss of coherency of the crystalline lattice planes. Fe^{3+}-O^{2-}-Fe^{3+} superexchange interactions result in a strong antiferromagnetic ordering with a Neel temperature of 400 K. Four sub lattices of goethite with spins inclined at an angle ±13° with respect to [010] direction contribute for the bulk magnetic structure [7]. Schematic of the unit cell of α-FeOOH is given along with the Mössbauer spectrum in Figure 3.3.

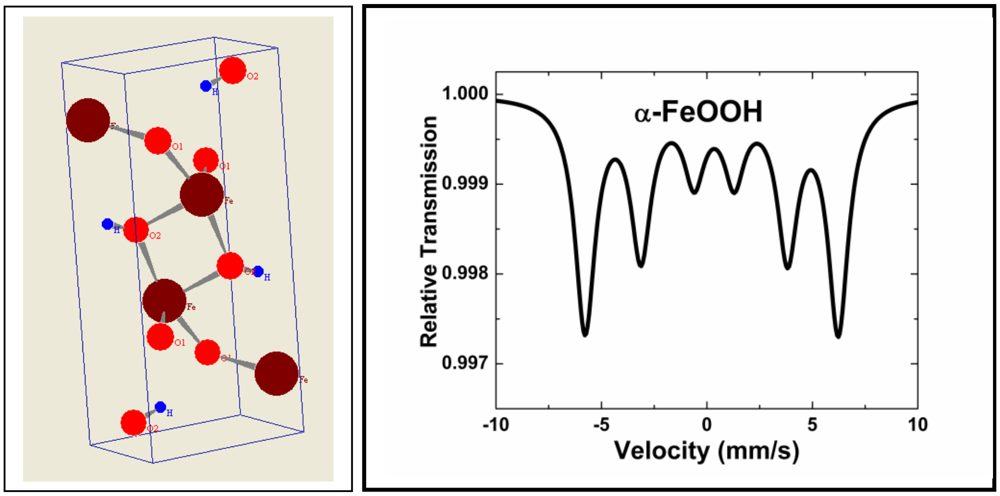

Figure 3.3: Crystal structure of Goethite (α-FeOOH) and its corresponding Mössbauer spectrum.

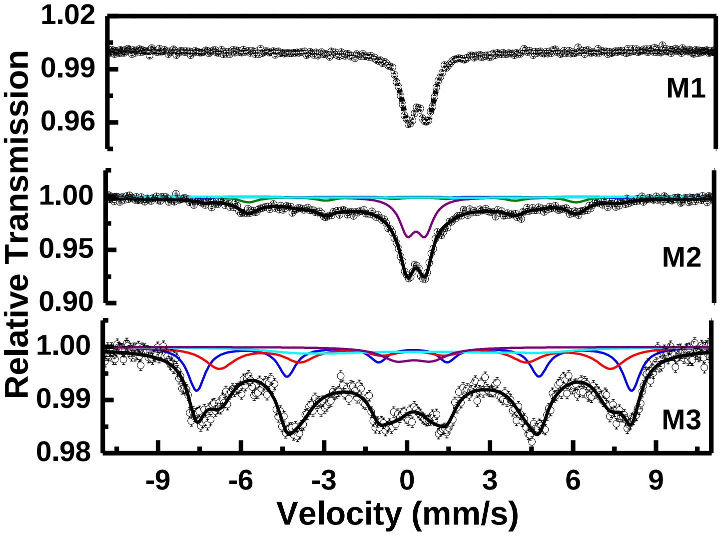

Figure 3.4: Mössbauer spectra of as prepared sample M1, M2 and M3.

Table 3.2 : Mössbauer parameter of the as synthesized magnetite nanoparticles. The value within the bracket gives the error of the first digit. f_1, f_2 are fractions of Fe atoms associated with super paramagnetic and disordered surface spins of nano particles respectively. Fractions f_3, f_4 of Fe atoms are associated with crystallite goethite, γ-Fe_2O_3, haematite respectively, while f_5 and f_6 represent Fe atoms occupying octahedral and tetrahedral interstitial sites of Fe_3O_4.

Sample details	i	Γ_i (mm/s)	δ_i (mm/s)	Δ_i (mm/s)	B_{hf}^{i} (T)	f_i (%)
M1	1	0.67(1)	0.34(2)	0.70(1)	-	100(3)
M2	1	0.69(2)	0.35(0)	0.65(1)	-	34(0)
	2	5.10(3)	0.34(9)	-0.32(3)	22.3(5)	45(2)
	3	0.84(9)	0.36(2)	-0.30(4)	36.8(4)	18(0)
	4	0.67(7)	0.34(0)	-0.04(0)	45.9(5)	03(1)
M3	1	1.4(1)	0.38(1)	1.12(1)	0	11(1)
	2	3.5(3)	0.47(3)	0.27(1)	27.2(6)	35(3)
	5	1.3(0)	0.38(0)	0.07(0)	43.8(3)	32(0)
	6	0.78(2)	0.36(1)	0.04(0)	48.7(4)	22(0)

Mössbauer spectra of M1, M2 and M3 are shown in Figure.3.4. The fitted Mössbauer parameters are listed in Table 3.2. Mössbauer spectrum of M1 shows a single doublet attributing to the ^{57}Fe (site 1) exhibiting superparamagnetism which is commensurate with the size calculated from the XRD (i.e. 6 nm) where nanoparticles below 10 nm exhibit a single doublet [8]. Hence the Mössbauer spectrum corresponding to M1 is due to association of Fe atoms with the nanoparticles of both α-FeOOH and magnetite. Sample M2 is indexed with a cubic spinel i.e. magnetite along with a lower intensity peaks corresponding to α-FeOOH nanoparticles (cf. Figure 3.2 (M2)). Mössbauer spectrum corresponding to M2 could be deconvoluted into four components including SPM, crystallite goethite and maghemite. M3 is deduced to contain 11% of SPM, and close to 55% of off-stoichiometric magnetite and about 35% of Fe atoms are deduced to be occupying the surface of the nanoparticles. Thus it is seen that the nanoparticles prepared using coprecipitation method are deduced to contain α-FeOOH also along with that of off-stoichiometric magnetite. Occurrence of α-FeOOH is observed in samples 1 and 2 along with magnetite, while the sample 3 contains only the magnetite nanoparticles as characterized by XRD and Mössbauer spectroscopy. This is basically understood due to the higher annealing temperature of precursor solution corresponding to samples 1 and 2 than that of the sample 3. Higher annealing temperature of precursor solution has resulted in partial oxidation of some of Fe^{2+} resulting in the occurrence of α-FeOOH along with magnetite particles. Magnetite nanoparticles could also be prepared purely through either +3 or +2 route [9,10]. Magnetite samples have also been prepared using Fe^{2+} route with $FeSO_4.7H_2O$, which is discussed in the following.

3.3 Preparation of Magnetite nanoparticles through Fe^{2+} route:

Freshly prepared aqueous NaOH was added drop wise to $FeSO_4.7H_2O$ solution of concentration 0.2 mol/lit to a pH value of 8 to convert sulfates in to hydroxides. The precipitate was dried for 15 days in air and the nanoparticles then obtained is referred as M4. XRD measurements indicate the presence of α-FeOOH and magnetite nanoparticles consistent with the reported results [6]. The XRD spectra are characterized by sharp peaks of Fe_3O_4 while indicating the poor crystalline nature of α-FeOOH.

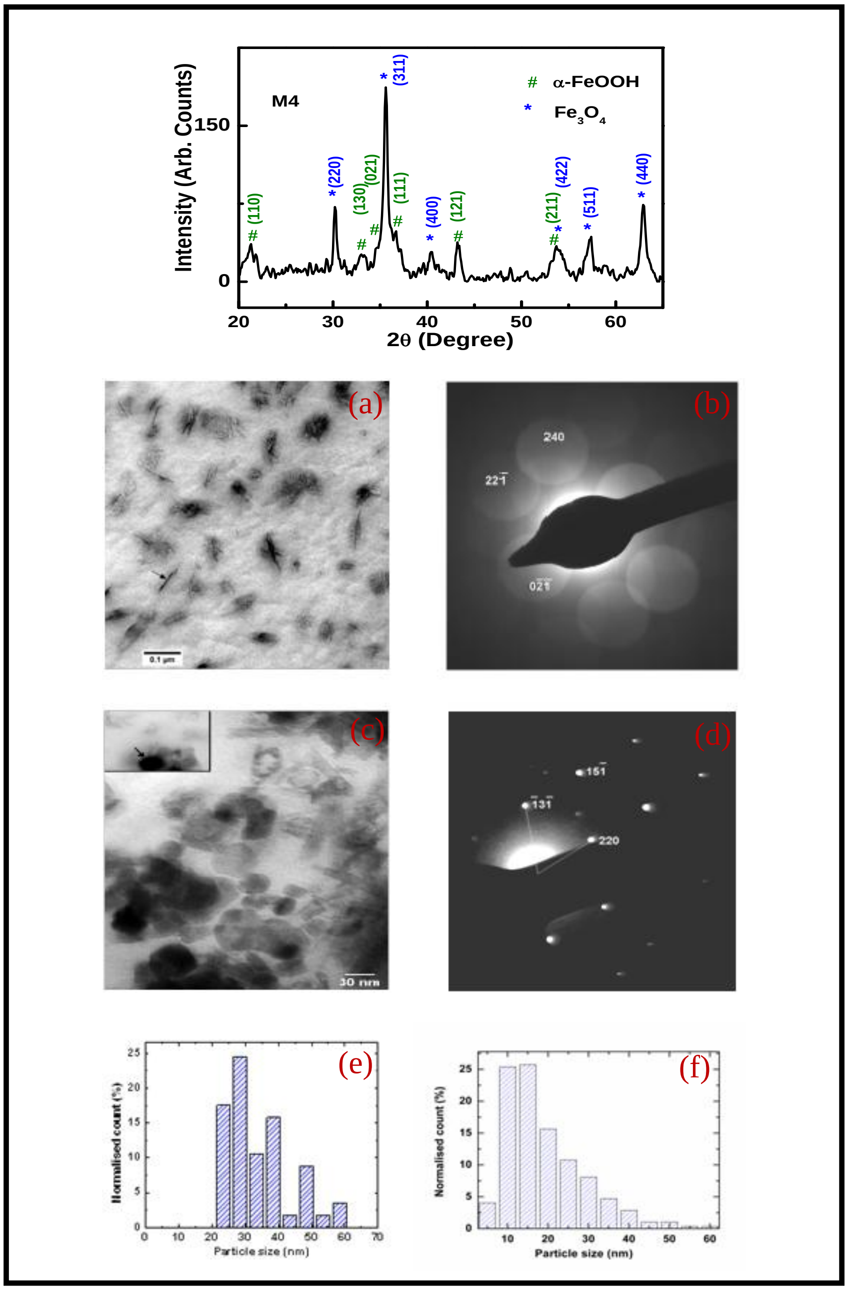

Figure 3.5: XRD spectrum of the sample M4 (top), and the corresponding TEM image is shown in bottom, (a) Bright field TEM micrograph showing fine rod like α-FeOOH particles. (b) Micro diffraction pattern from a goethite particle in fig 3.5(a) along zone axis [2 -1 2]. (c) Bright field TEM micrograph of Fe_3O_4 (d) Micro diffraction pattern from magnetite particle as marked in Fig 3.5(c). while (e) and (f) refer to size distribution of α-FeOOH and Fe_3O_4 particles.

TEM image (Cf. Figure 3.5) shows the presence of rod shaped particles which were deduced to be α-FeOOH based on the analysis of micro diffraction pattern (Cf. Figure 3.5(b)) obtained on these particles. Size distribution of α-FeOOH particles as obtained based on the analysis of TEM image (Cf. Figure 3.5(a)) is shown in Figure 3.5(e). This shows that about 30% of α-FeOOH particles are in the size range 5-10 nm, while 40% are in the range of 15-20 nm and the remaining particles are larger with the size ranging between 25-40 nm. It is clear from the TEM image analysis (Cf. Figure 3.5 (c) and (e)) that the Fe_3O_4 particles are much larger than that of α-FeOOH particles with size ranging between 20 nm and 70 nm (Cf. Figure 3.5(f)).

Particle size as calculated using Scherrer formula shows an increase in particle size as the rotational speed during precipitation decreases (cf. Figure 3.2 (inset)).

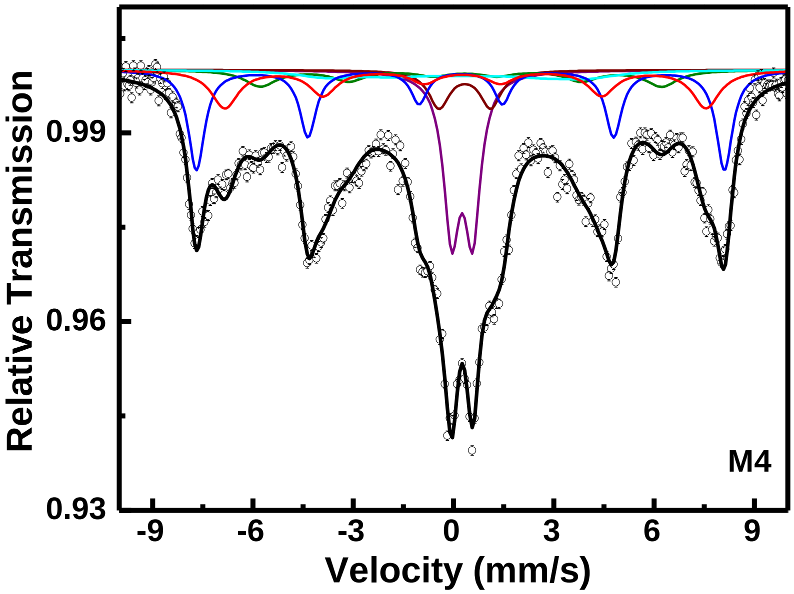

Figure 3.6: Mössbauer spectra of the as prepared sample of magnetite (M4).

Table 3.3: Mössbauer parameters of the as synthesized magnetite nanoparticles (M4). The value in the bracket gives the error of the first digit. M4 consists of superparamagnetic particles of α-FeOOH indicated as the fraction f_1 and f_2 while f_4 is associated with Fe at the surface of nanoparticles of α-FeOOH and f_3 due Fe atoms associated with crystallite α-FeOOH. , f_5 and f_6 are due to Fe atoms occupying tetrahedral and octahedral interstitial sites in off-stoichiometric magnetite.

Phase	**Size (nm)**	**i**	**Γ_i (mm/s)**	**δ_i (mm/s)**	**Δ_i (mm/s)**	**B_{hf}^i (T)**	**f_i (%)**
α-FeOOH	4	1	0.58(0)	0.38(1)	0.63(1)	-	16 (0)
		2	0.71(1)	0.46(2)	1.56(0)	-	06(0)
		3	1.22(2)	0.39(4)	-0.12 (1)	37.4(7)	15(1)
		4	2.30(8)	0.40(6)	-0.31(3)	23.9(9)	21(4)
Magnetite	39	5	0.57(0)	0.33(0)	0.02(0)	49.0(9)	20(0)
		6	0.95(1)	0.39(0)	0.11(1)	44.9(8)	22(1)

3.4 Understanding the occurrence of α-FeOOH along with magnetite prepared by co-precipitation

Coprecipitation of Fe^{3+} ions with divalent cations, M^{2+} to various Fe^{3+} -based spinel ferrites has a complex kinetics. Various factors in the synthesis such as raw materials, ionic concentrations, solvent effect, pH of the medium, aging time and all more temperature also plays an important role in dictating the final precipitate [4]. Raw materials i.e. precursors and the precipitating agents affects the precipitation, for example ions such as Cl^{1-}, and SO_4^{2-} act as Poison in many catalytic effects [4]. High ionic concentration is desirable for precipitation of the metal ions. This increases the space-time yields by decreasing the vessel volume for the same mass of precipitate. The higher degrees of supersaturation lead to faster precipitation. Above all, smaller particle sizes and higher surface areas are usually achieved at higher concentrations due to increased nucleation rates at higher supersaturation if homogeneous nucleation takes place [1,4].

Precipitate during coprecipitation is influenced by the solvent used, in terms of particles size which was tuned by tuning the dielectric constant of the solvent [11], it is also reported affecting the final product as the [H_2O] / [ethanol] ratio changes [12]. Apart from the factors mentioned the pH plays a very important role in the precipitation since it directly controls the degree of supersaturation at least if hydroxides are precipitated, this should be one of the crucial factors in precipitation processes. As for many other parameters, the influence of pH is not simple, and must be investigated experimentally for any specific system, even in a relatively well-known system such as magnetite [4].

Apart from the pH, synthesis temperature is a decisive factor for controlling the precipitate properties such as primary crystallite sized, surface area and the phases formed. Synthesis is preferred to carry out above room temperature near to 373 K, since precipitation occurs more rapidly, provided that high levels of supersaturation are maintained. However, synthesis temperature may alter the concentration of ions leading to the non stoichiometry which finally affects the nucleation growth of the desired composition leading to a mixed phase [4].

After precipitation the properties of the precipitate may vary during aging such as crystal growth due to Oswald ripening. While the precipitate is in solution, any impurities which may be occluded may be redissolved especially during a fast precipitation reaction.

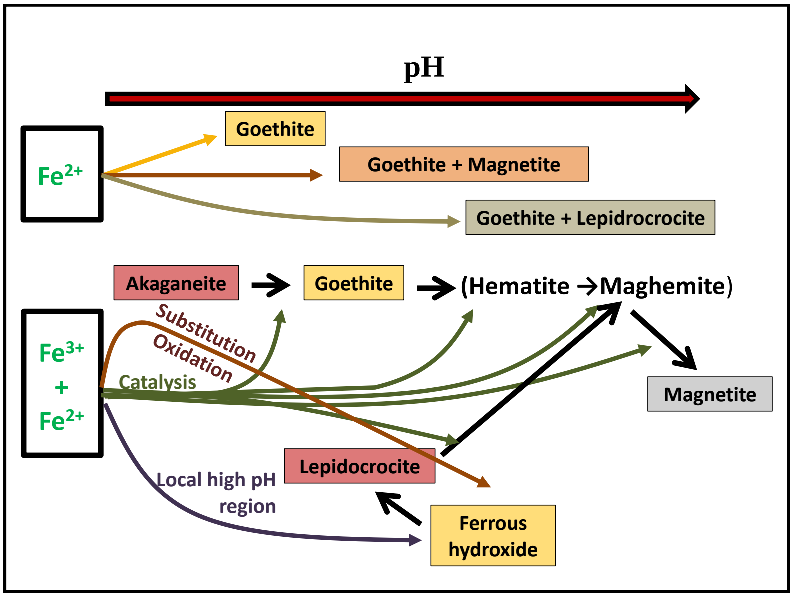

Figure 3.7: Various intermediates of oxidation of Fe^{2+} and Fe^{3+}/Fe^{2+} precursors [14,16]**.**

In the coprecipitation of Fe_3O_4, iron oxyhydroxides occur as the intermediates phase as shown in the Figure 3.7. Many investigations on the formation of magnetite using co-precipitation was carried out [13-16], where the coexistence of α-FeOOH was confirmed using TEM which could not be deduced using XRD [17-18].

Having observed the occurrence of α-FeOOH along with off-stoichiometric magnetite in the end product of coprecipitation of precursor solutions corresponding to Fe^{2+} and Fe^{3+}, it is required to find out the possibility of reduction of α-FeOOH to magnetite which would be discussed in the following.

3.5 Reduction of alpha-FeOOH to magnetite:

It has been reported that α-FeOOH when heated dehydrates to α-Fe_2O_3 due to removal of hydroxyl sheets and some of the oxygen in strips parallel to c-axis to form water [19]. Various aspects related to the topotactical transformation of α-FeOOH to α-Fe_2O_3 have been addressed in a detailed manner in the literature [20-26]. Possibility of formation of Fe_3O_4 in small concentration has also been reported due to dehydration of α-FeOOH based on low temperature magnetization studies [19]. α-FeOOH has been reported to reduce directly by mechano chemical means by ball milling treatment which was understood mainly due to hydrogen gas generated during the milling process [20]. Hence the reduction of α-FeOOH to magnetite is explored due to controlled annealing treatment of the products of the above Fe^{2+} based reaction in a detailed manner using Mössbauer spectroscopy.

3.5.1 Thermal evolution of off-stoichiometric to stoichiometric magnetite nanoparticles

Sample containing α-FeOOH and off-stoichiometric magnetite nanoparticles was subjected to annealing at different temperatures and at a partial pressure of 10^{-6} mbar. After each annealing step the Mössbauer measurements were carried out at 300 K. Some of the representative Mössbauer spectra of the sample subjected to annealing at different temperatures have been presented in Figure 3.8. Mössbauer results obtained in the starting sample (Cf. Figure 3.6 and Table- 3.3) with the external magnetic field of strength 0.3 Tesla applied parallel to γ-ray direction (Cf. Figure 3.8 and Table- 3.4) mainly show that based on the values of the intensity ratios $I_{2,5}$ / $I_{3,4}$ for different Fe sites associated with α-FeOOH and off stoichiometric magnetite that the spins of Fe atoms occupying tetrahedral and octahedral sites of magnetite could be understood to be collinear and slightly canted respectively. High value of $I_{2,5}$ / $I_{3,4}$ corresponding to sextets associated with f_4 is consistent with the canted nature of spins and is understood to be due to OH^- vacancies. Application of the external magnetic field is seen to

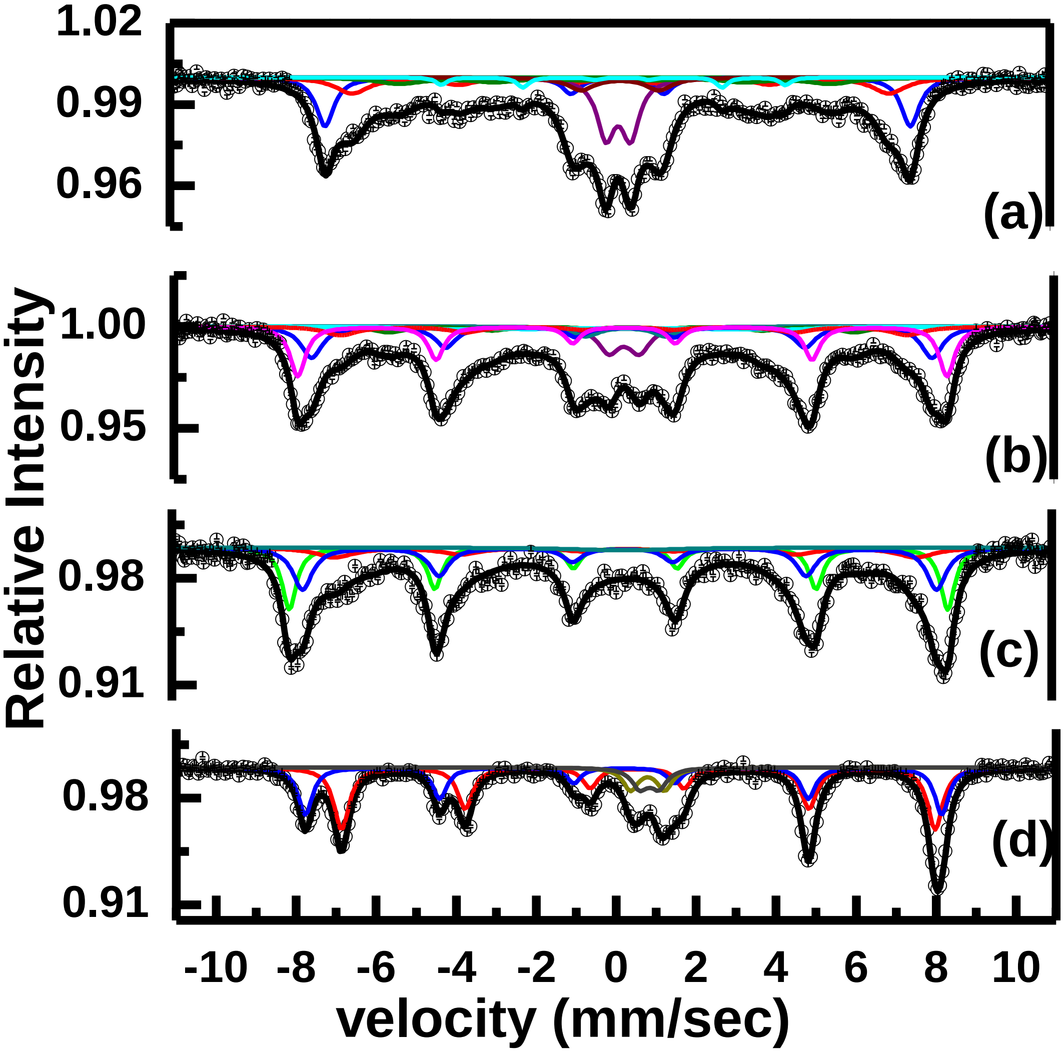

Figure 3.8: Mössbauer spectra obtained in the sample containing nano composites of α-FeOOH and Fe_3O_4 subsequent to annealing at a partial pressure of (3±1) × 10^{-6} mbar at different temperatures viz., (a) 0.3 T γ-rays, (b) 423 K, (c) 623 K and (d) 1073 K

Table 3.4. Hyperfine parameters as experienced by relative fractions of Fe atoms associated with nano goethite (f_1, f_2, f_3 and f_4), magnetite (f_5, f_6) particles in the starting sample and the polymorphs of iron oxides derived due to thermal reduction of nano goethite such as maghemite (f_7) and hematite (f_8). Fraction f_9 refers to nano haematite while f_{10} and f_{11} refer to that of Fe atoms associated with FeO reduced from Fe3O4. Detailed description of each fraction is referred to the text.

Sample	**i**	Γ_i (mm/s)	δ_i (mm/s)	Δ_i (mm/s)	B^i_{hf} (Tesla)	f_i (%)
B_{ext}=0.28 T	1	0.55(1)	0.34(0)	0.64(1)	-	15(0)
MF II γ-rays	2	0.97(3)	0.46(1)	1.91(2)	-	07(1)
	3	1.39(5)	0.36(1)	-0.08(1)	34.6(1)	30(0)
	4	0.46(1)	0.42(2)	-0.22(1)	26.7(3)	04(0)
	5	0.57(2)	0.30(0)	0.05(0)	47.1(1)	20(2)
	6	1.00(5)	0.43(0)	0.12(0)	43.1(0)	24(1)
Ta = 423K(1h)	1	0.61(0)	0.37(0)	0.75(1)	-	09(0)
3×10^{-6} mbar	2	0.77(1)	0.42(0)	1.93(2)	-	05(0)
	3	1.04(1)	0.37(0)	-0.18(1)	36.3(0)	10(0)
	4	2.22(3)	0.38(2)	-0.12(3)	25.1(3)	19(3)
	5	0.60(1)	0.33(1)	0.09(1)	48.1(0)	21(0)
	6	0.93(0)	0.39(2)	0.13(0)	44.1(1)	15(0)
	7	0.47(0)	0.35(1)	-0.04(0)	50.3(2)	21(1)
Ta = 623K(1h)	5	0.59(0)	0.31(1)	0.07(0)	49.1(1)	33(0)
3×10^{-6} mbar	6	1.13(2)	0.42(1)	0.06(1)	45.1(2)	31(1)
	8	0.48(1)	0.39(1)	-0.16(0)	51.0(2)	28(2)
	9	2.68(3)	0.29(0)	1.02(2)	-	08(1)
Ta = 873K(1h)	5	0.54(1)	0.30(0)	0.10(1)	49.5(5)	34(0)
3×10^{-6} mbar	6	0.81(0)	0.54(1)	0.08(0)	45.7(1)	32(0)
	8	0.37(2)	0.31(1)	-0.17(2)	51.7(2)	34(0)
Ta = 873K(1h)	5	0.48(1)	0.35(0)	0.06(0)	48.4(1)	18(0)
8×10^{-6} mbar	6	1.08(0)	0.48(1)	0.06(1)	43.7(2)	19(0)
	8	0.38(1)	0.34(2)	-0.13(0)	50.5(4)	26(1)
	8a	0.33(0)	0.39(0)	-0.21(1)	51.9(3)	29(1)
	9	2.68(2)	0.29(0)	1.02(0)	-	08(0)
Ta = 1073K(1h)	5	0.43(0)	0.31(1)	0.01(0)	49.0(2)	36(0)
3×10^{-6} mbar	6	0.46(1)	0.66(2)	0.03(0)	46.0(1)	54(1)
	10	0.49(0)	0.95(1)	0.48(2)	-	05(00)
	11	0.46(0)	0.91(1)	0.85(1)	-	05(0)

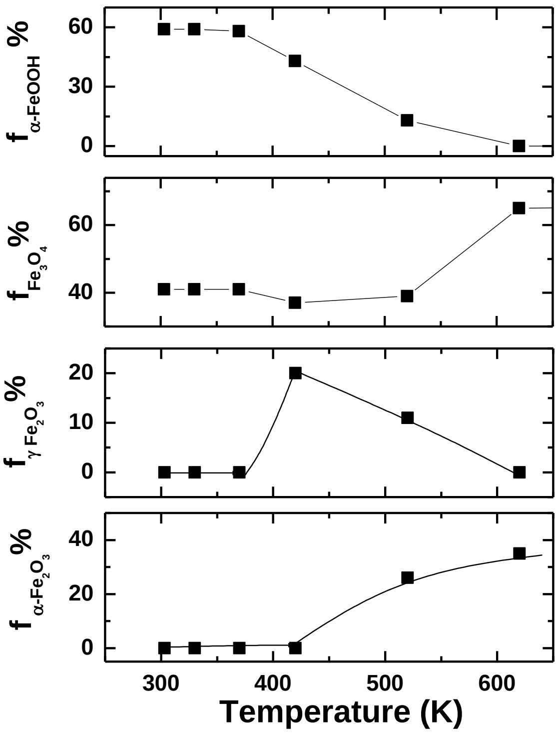

Figure 3.9: Variation of the fractions of iron atoms associated with the phases of α-FeOOH ($f_{\alpha\text{-FeOOH}} = f_1+f_2+f_3+f_4$), Fe_3O_4 ($f_{Fe3O4}=f_5+f_6$), γ-Fe_2O_3 ($f_{\gamma\text{-Fe2O3}} = f_7$) and α-$Fe_2O_3$ ($f_{\alpha\text{-Fe2O3}}=f_8$) with annealing temperature.

result in a decrease in the spin disordering of Fe atoms associated with the fraction f_4. These results in an increase in the fraction f_3 attributed to crystalline like α-FeOOH at the cost of f_4.

It is commonly agreed that the surface of nano particles of α-FeOOH contain defects resulting in a large line width in the Mössbauer spectra characteristic of distribution in the hyperfine fields [27]. This observation elucidates the important role played by surface spins for accounting for the super exchange interactions between closely spaced antiferromagnetic goethite particles. Having identified in detail the distinct sites of Fe atoms associated with nano particles of α-FeOOH of different size and off stoichiometric magnetite, the following discussion is mainly based on the evolution of the fractions of Fe atoms associated with distinct phases of iron oxides due to thermal reduction of α-FeOOH.

The variations of fractions (viz., f_1, f_2, f_3, f_4) associated with α-FeOOH, (f_5, f_6) corresponding to Fe_3O_4 nano particles and their evolutions with annealing treatments are shown in Figure 3.9. The variations occur appreciably in the temperature interval between 350-550 K in which desorption of excess water and structural OH^- of α-FeOOH is observed to take place significantly due to thermal reduction. The hyperfine parameters associated with Fe_3O_4 in the as prepared sample (Cf. Table-3.3) are found to be different from that of the bulk magnetite [8]. Ratio of population of Fe atoms associated with octahedral and tetrahedral sites is 1:1 instead of 2:1 corresponding to that of the bulk magnetite. This implies the off stoichiometry of the magnetite which could arise due to Fe vacancies occurring at octahedral and tetrahedral sites. As the ratio of population of f_5:f_6 is 1:1, the number of Fe vacancies at octahedral sites is likely to be higher than that of tetrahedral sites. This is commensurate with the observation of higher quadrupole splitting corresponding to octahedral sites than that experienced by absorber atoms occupying tetrahedral sites (Table-3.3).

3.5.2 Thermal evolution of α-FeOOH to polymorphs of iron oxides in reduced atmosphere

The magnitude of the fractions (viz., f_1, f_2, f_3, f_4) associated with α-FeOOH, (f_5, f_6) corresponding to Fe_3O_4 nano particles are seen to be constant for annealing treatments up to 370 K (Cf. Figure 3.9). Spectrum analysis shows that annealing at 420 K results in the formation of γ-Fe_2O_3 with the value of this fraction (f_7) becomes 20 %. Concomitantly there is a reduction in the relative fraction of Fe_3O_4 by 5% (Cf. Table-3.4). Hence it can be understood that the occurrence of γ-Fe_2O_3 with the value of f_7 as 20% has resulted from the conversion of 15% of α-FeOOH, and the remaining fraction of 5% due to oxidation of Fe_3O_4. Color of the sample has become more brownish in accordance with an increase in γ-Fe_2O_3. Annealing at 520 K results in the formation of a fraction (f_8) of 20% of α-Fe_2O_3 as converted from α-FeOOH. Also a reduction in the relative fraction of Fe atoms associated with γ-Fe_2O_3 by 10% is observed due to annealing treatment at 520 K concomitantly leading to an increase in the relative fraction of Fe_3O_4. The fraction f_7 associated with γ-Fe_2O_3 becomes zero following the annealing at 620 K leading to an associated relative increase in the fraction of Fe_3O_4 by 15%. Thus the fraction of Fe atoms associated with Fe_3O_4 becomes 60% following the annealing at 620 K. Annealing beyond 500 K results in the formation of α-Fe_2O_3 phase as indicated by fraction f_8, due to topotactic transformation of α-FeOOH. Thus it is seen that OH^- play an important role in the conversion of α-FeOOH to γ-Fe_2O_3 in the temperature interval 400-450 K, while the partial reduction of α-FeOOH to Fe_3O_4 is observed in the annealing interval of 500-625 K.

Comparison of this result with that of the as prepared sample containing 60% and 40% of α-FeOOH and Fe_3O_4 respectively, it could be deduced that the annealing treatments of the sample at low temperatures (<625 K) and at low partial pressure results in the conversion of a relative fraction of 15% of α-FeOOH to Fe_3O_4. Primary stages of reduction of α-FeOOH occur at temperatures less than 450 K were the formation of γ-Fe_2O_3 while the reduction of α-FeOOH to Fe_3O_4 takes place during annealing treatments between 500-625 K. Also the formation of α-Fe_2O_3 is observed to occur in the interval 500-625 K. Reduction of α-FeOOH involves removal of excess H_2O, loosely bound OH^- and strongly bound structural OH^- at different temperatures of annealing.

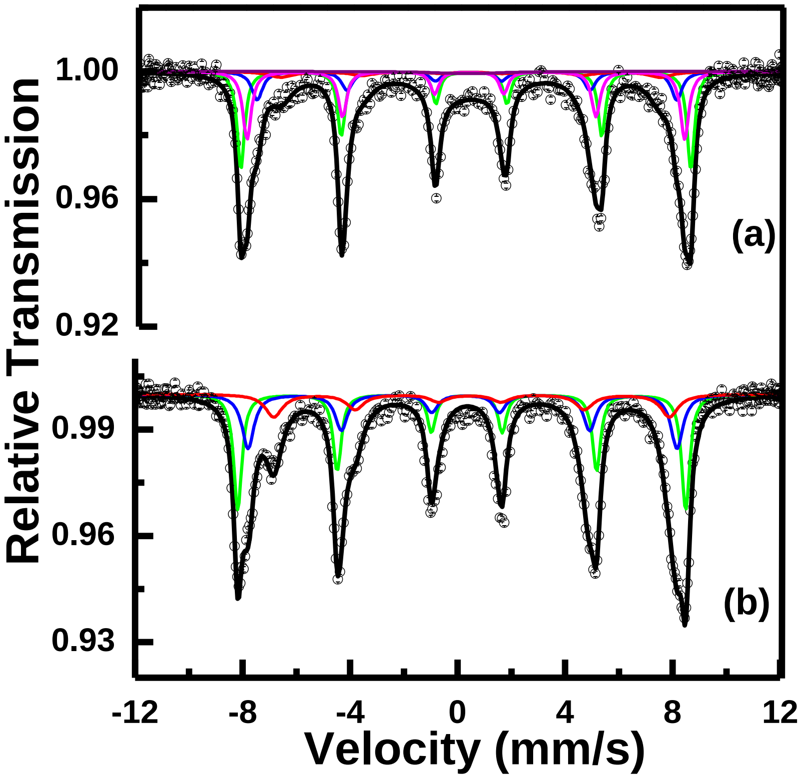

Figure 3.10: Mössbauer spectra corresponding to the sample annealed at 873 K. This temperature is so chosen to be much higher than 650 K marking the complete conversion of goethite to oxides. Spectra (a) and (b) refer to the sample annealed at 873 K at partial pressure of $8x10^{-6}$ mbar and $2x10^{-6}$ mbar respectively. Spectrum (a) clearly reveals that α-FeOOH annealed at 870 K (well above the dissociation temperature of α-FeOOH) and at a partial pressure close to 10^{-5} mbar gets predominantly converted to α-Fe_2O_3. (b) Annealing at 873 K and at a lower partial pressure $2x10^{-6}$ mbar results in an enhanced Fe_3O_4 due to α-FeOOH → α-Fe_2O_3 → Fe_3O_4.

It is interesting to find out the effect of thermal reduction of goethite by annealing the starting sample at a temperature much higher than 650 K, well beyond the temperature of complete conversion of α-FeOOH to iron oxides as deduced from Fig 3.10. In order to understand the effect the sample has been annealed at 870 K at a vacuum of $8\text{x}10^{-6}$ mbar. Analysis of the Mössbauer spectrum (Cf. Figure 3.10) shows the existence of α-Fe_2O_3 and Fe_3O_4 by relative fractions 60% and 40% respectively. This is seen to be commensurate with the starting composition of the fractions of 60% and 40% of goethite and magnetite respectively in the as prepared sample. This result shows clearly that annealing of α-FeOOH at high temperatures (much above 650 K) and at a partial pressure as low as 10^{-5} mbar results only in the complete conversion of α-FeOOH to α-Fe_2O_3. Annealing at 870 K at a partial pressure of $3\text{x}10^{-6}$ mbar results in the formation of Fe_3O_4 and α-Fe_2O_3 with the relative fractions 70 : 30. A higher volume fraction of magnetite seen in the case of sample annealed at lower partial pressure is understood to be due to partial reduction of hematite to magnetite. Mechanism of formation of γ-Fe_2O_3 / Fe_3O_4 from goethite is discussed in the following paragraph.

3.5.3 Proposed mechanism of conversion / reduction of α-FeOOH to γ-Fe_2O_3 / Fe_3O_4

Crystal structure of α-FeOOH consists of an hcp array of anions (O^{2-} and OH^-) stacked along the [010] direction with Fe^{3+} ions occupying half the octahedral interstices within a layer. Each Fe ion is surrounded by three O^{2-} and three OH^- to result in $FeO_3(OH)_3$ octahedra. Partial transformation of goethite to maghemite is observed to occur over the temperature interval 400-450 K based on the present Mössbauer results. The mechanism of the conversion of α-FeOOH to γ-Fe_2O_3 can be understood as follows. Core of goethite particles are rich in OH^- while the surface of these particles are deficient in OH^-. Hence OH^- from water molecules gets bonded with OH- dangling bonds. Annealing beyond 400 K results in a partial dissociation of H^+-OH^- bonded with dangling bonds of α-FeOOH. These causes desorption of hydrogen molecules which react with interface oxygen atoms giving rise to water molecule and anionic (oxygen) vacancies. Thus the creation of oxygen vacancies results in an increase in the local concentration of Fe ions. These excess Fe ions diffuse in the restacked manner to form γ-Fe_2O_3 lattice. This is shown schematically in Figure 3.11. A fraction of about 20% of Fe atoms are found to be associated with γ-Fe_2O_3 subsequent to annealing treatment at 420 K.

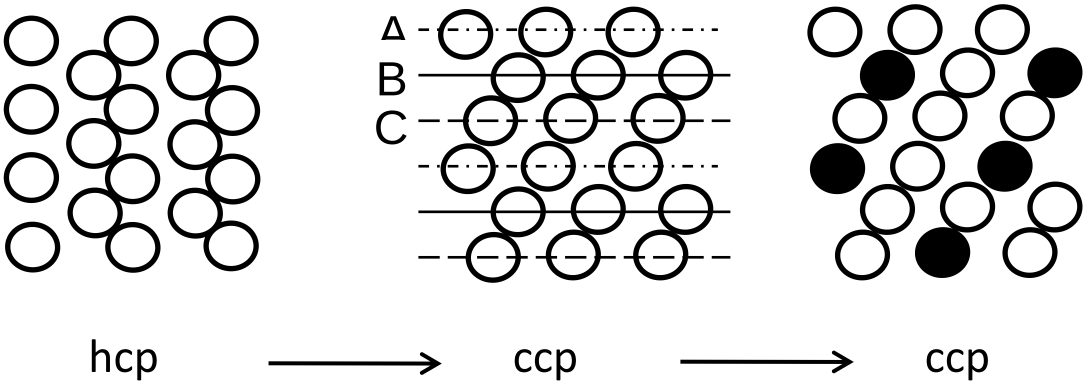

Figure 3.11: Schematic of the conversion of goethite to cubic spinel maghemite and magnetite due to thermal reduction is shown. Stacking sequence of cations gets altered from that of hcp ABAB… as in goethite to cubic close packed as ABCABC resulting in the conversion to maghemite in the annealing interval 375-425 K. Annealing treatments in the interval 550-650 K results in the conversion of some of the Fe^{3+} ions to Fe^{2+} due to desorbed OH- resulting in the reduction of α-FeOOH to Fe_3O_4.

Annealing beyond 550 K results in the conversion of some of Fe^{3+} to Fe^{2+} in γ-Fe_2O_3 lattice which might get formed as explained above leading to the reduction of α-FeOOH to off-stoichiometric magnetite. Hence the role of desorbed hydrogen is imminent in the conversion/ reduction of α-FeOOH to γ-Fe_2O_3 and Fe_3O_4 respectively. Annealing beyond 500 K is seen to result in a predominant conversion of α-FeOOH to α-Fe_2O_3 due to topotactic transformation.

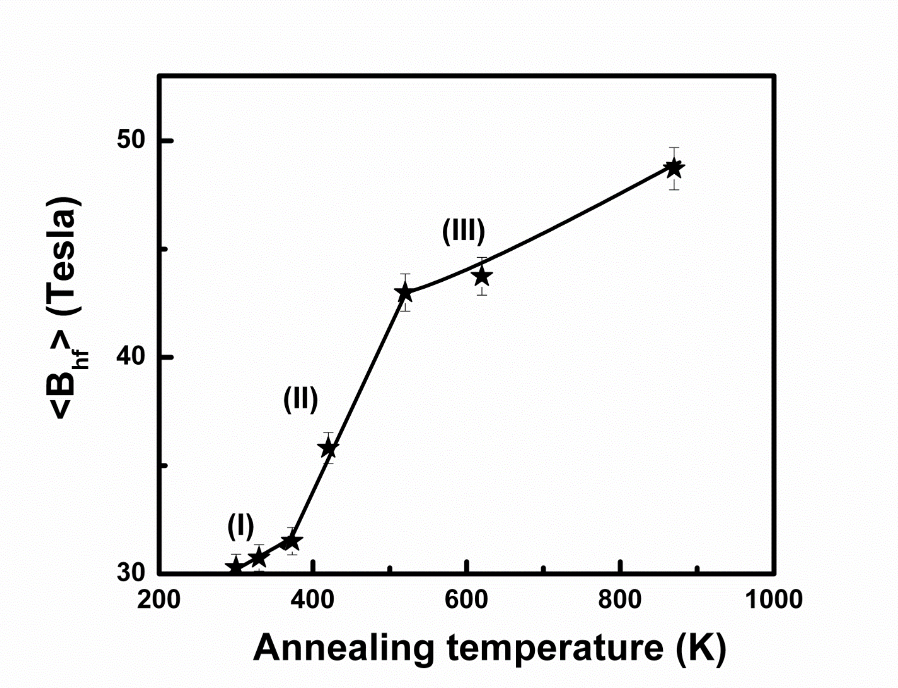

Figure 3.12: Variation of the mean hyperfine field <B_{hf}> with annealing temperature of the starting sample containing α-FeOOH and Fe_3O_4 in the ratio of 0.6:0.4 due to thermal reduction of α-FeOOH to polymorphs of iron oxides. The above variation marks three different slopes (d<B_{hf}>/dT) viz., understood to be due to (I) dissociation of inter dispersed water molecules between α-FeOOH, (II) reduction of α-FeOOH to γ-Fe_2O_3 and (III) due to the formation of Fe_3O_4 and α-Fe_2O_3 respectively.

The role played by oxygen is thus important with respect to the formation of α-Fe_2O_3 from α-FeOOH. Though the dissociation of structural OH^- would take place from α-FeOOH while subjected to annealing at high temperatures ($T > 650$ K) and at moderate partial pressures, the desorbed hydrogen could not result in oxygen vacancies leading to the formation of any cubic phase of iron oxide. Hence annealing beyond 650 K results only in the topotactic transformation of α-FeOOH to α-Fe_2O_3 as elucidated in the previous section (Cf. Figure 3.9). While plotting the variation in the mean hyperfine field which is given as $\langle B_{hf} \rangle = \sum f_i B_{hf}^i / \sum f_i$, with temperature three different regimes could be deduced based on the changes in the slope as shown in Figure 3.12. Mean hyperfine field at 300 K is close to 30 Tesla. This is understood due to the association of 25% of Fe atoms with superparamagnetic particles of α-FeOOH and 40% of Fe atoms with Fe_3O_4. An increase in the mean field in the interval 300-375 K, marked as slope-I in the figure, is understood to be due to the decrease in the mean distance of separation of α-FeOOH particles following dehydration of excess water molecules inter dispersed between them. A steep increase in the value of $d\langle B_{hf} \rangle/dT$ in the interval $400 < T < 500$ K (slope-II) is ascribed to the reduction of as high as 20% of α-FeOOH to γ-Fe_2O_3. Occurrence of slope marked as III is understood to be due to the conversion of α-FeOOH to Fe_3O_4 and α-Fe_2O_3 in the temperature interval $500 \text{ K} < T < 650$ K.

Based on this study it is inferred that the low temperature annealing results in a partial conversion or reduction of α-FeOOH to off-stoichiometric magnetite or maghemite nanoparticles. In order to elucidate further on this finding a two step annealing has been proposed to understand clearly the possibility of nucleation and growth of magnetite from α-FeOOH. In order to make the reduction of α-FeOOH to off stoichiometric magnetite it is essential to start with nanoparticles of size less than or close to 10 nm. A novel annealing method is proposed in the following to study the optimal reduction of α-FeOOH to magnetite.

3.6 Two step annealing of nanocomposites of ironoxyhydroxide (α-FeOOH) and iron oxide (Fe_3O_4)

This annealing study has been carried out on a sample prepared as mentioned earlier which contains superparamagnetic particles of α-FeOOH and off stoichiometric magnetite. (Cf. Figure 3.4 (M1)). Mössbauer spectra obtained in the as prepared sample and subsequent to annealing at 773 K are shown below. Annealing results indicate that the starting sample might be composed of α-FeOOH and off-stoichiometric magnetite in the ratio 70:30. Based on the previous study it has been observed that the annealing of α-FeOOH at low temperature in the interval 373 K – 480 K results in a optimal reduction of α-FeOOH to off-stoichiometric magnetite. Hence the first step of the annealing was carried out at different temperatures spanning between 373 – 573 K while the second step of annealing was carried out at 773 K. Second step would ensure the particles not reduced due to I step are topotactically converted to α-Fe_2O_3. On the other hand α-FeOOH particles reduced due to earlier treatment are likely to be reduced to magnetite. Each annealing step was carried out for 1 h at 2×10^{-6} mbar. The treatments temperature is listed in Table 3.4. From the XRD of the sample M1 (c.f. Figure 3.2) consist of Fe_3O_4 with 6 nm particle size as determine by Scherrer formula with broad humps at the peak position of α-FeOOH. FWHM of the maximum intense peak decrease to large extend after annealing at 773 K signifying a reasonable coarsening of the nanoparticle (cf. Figure 3.14).

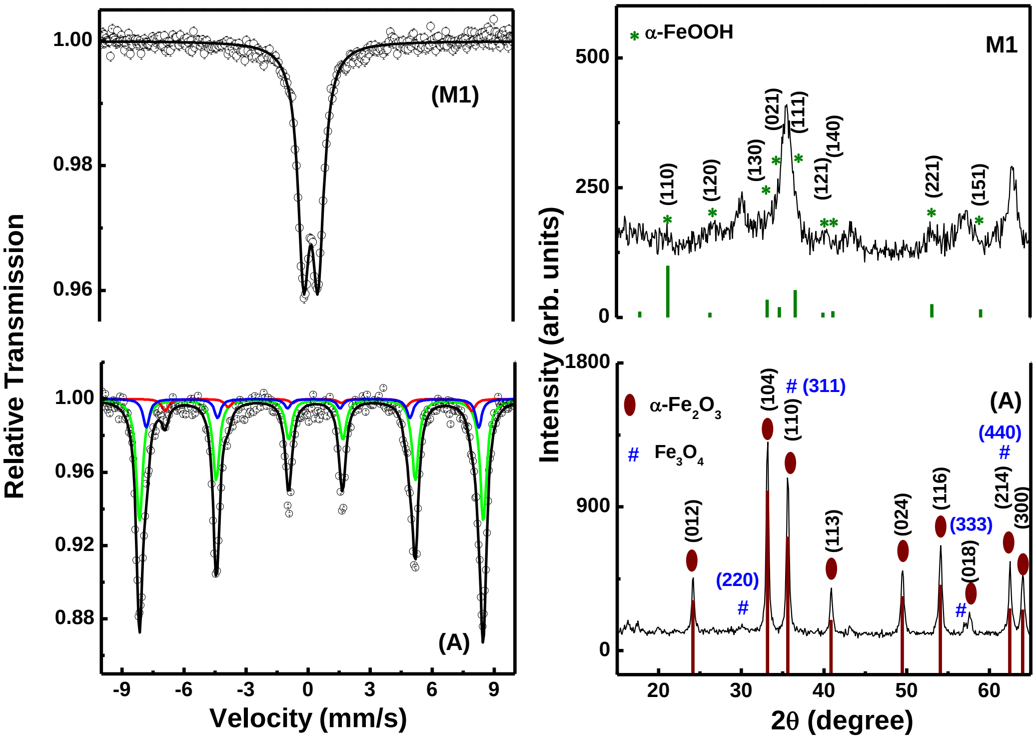

Figure 3.13: Mössbauer spectra of the sample M1 and the annealed at 773 K (A) with the corresponding XRD shown at the right column.

Table 3.4. List of treatments with varying temperature of the first step of annealing. While the second step of all these annealing treatments was carried out at 773 K.

Annealing Treatment	Temperature of I step (K)
A	-
B	373
C	403
D	423
E	448
F	473
G	523

The XRD of the sample after treatment A and G shows a drastic divergence in the final product. In the 'A' treated sample, the XRD peaks can be indexed with α-Fe_2O_3 and trace amount of Fe_3O_4 whereas in the 'G' treated sample Fe_3O_4 dominates over α-Fe_2O_3 which commensurate with the Mössbauer spectra as shown in Fig 3.15.

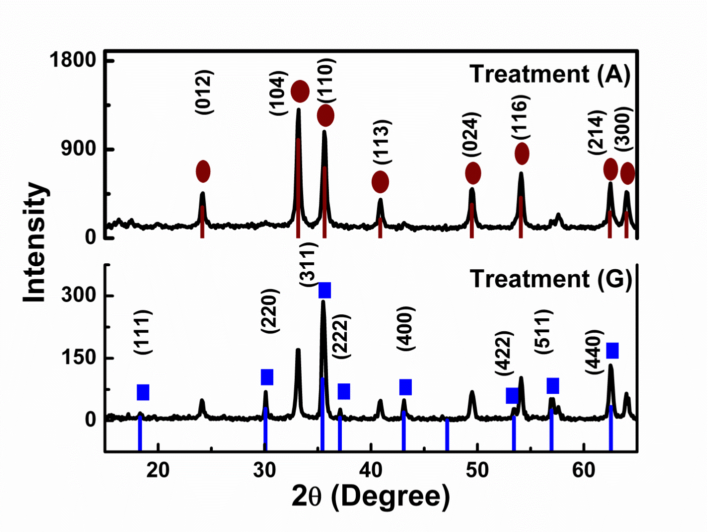

Fig 3.14. XRD spectrum of M1 subsequent to annealing at 773 K for 1 h at 2×10^{-6} mbar is referred to as (A), while the figure G represents M1 subjected to two step annealing treatments at temperature 523 K and 773 K respectively.

The Mössbauer spectra of the M1 after two step annealing are shown in Figure 3.15. Hyperfine parameters of the iron oxides after second step annealing, remains almost constant except for the change in the area fraction under the curve of Fe_3O_4 and α-Fe_2O_3 (c.f. Figure 3.16.). The variation in the area fraction of Fe at octahedral and tetrahedral site of Fe_3O_4 increases as the first step annealing temperature increases. The Fe_3O_4 fraction decreases from a certain first step annealing temperature above 423 K. It is seen that an increase in Fe3O4 is concomitant with a decrease in the fraction of Fe atoms associated with α-Fe_2O_3. H^+ adsorbed on the surface of the nanoparticles of α-FeOOH due to low temperature annealing during I step results in the formation of oxygen vacancies initiating the cubic phase transformation. Subsequent annealing step at higher temperature results in the reduction of these particles to stoichiometric magnetite Fe_3O_4.

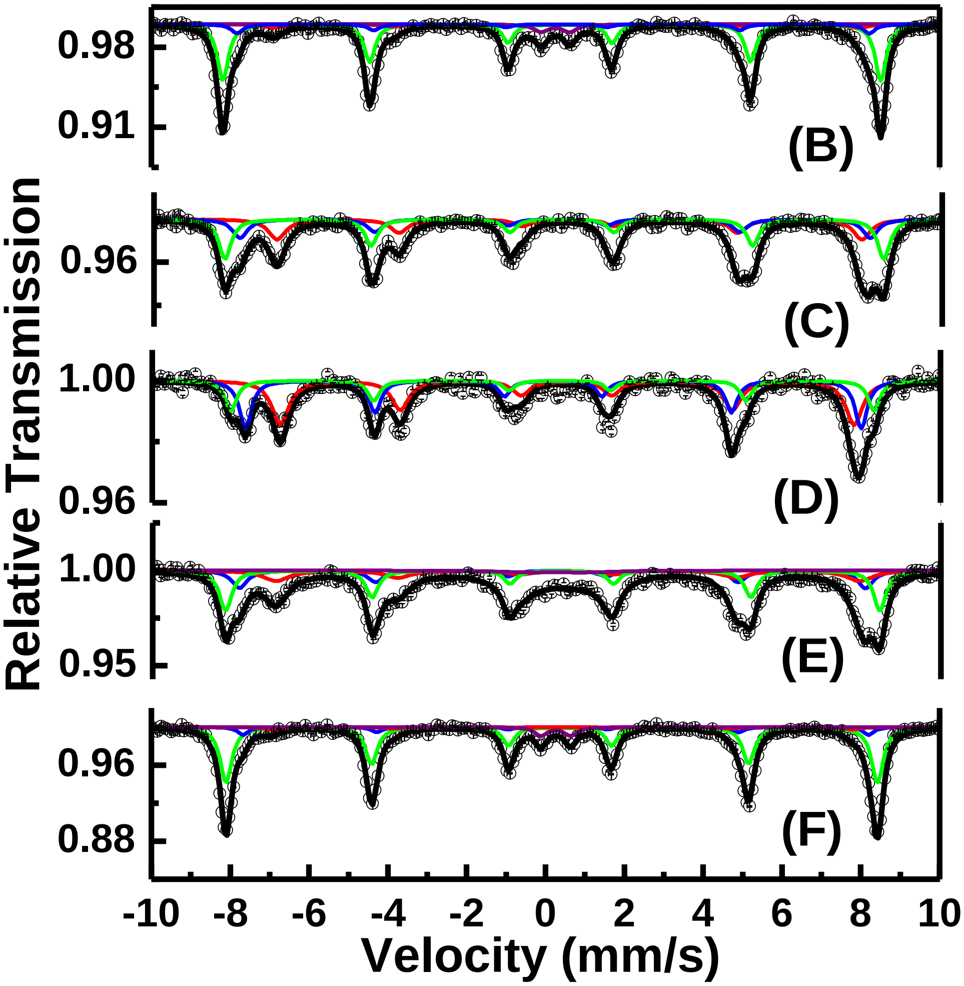

Fig 3.15. Mössbauer Spectra of M1 after treatments B, C, D, E and F as mentioned in Table-3.4 .

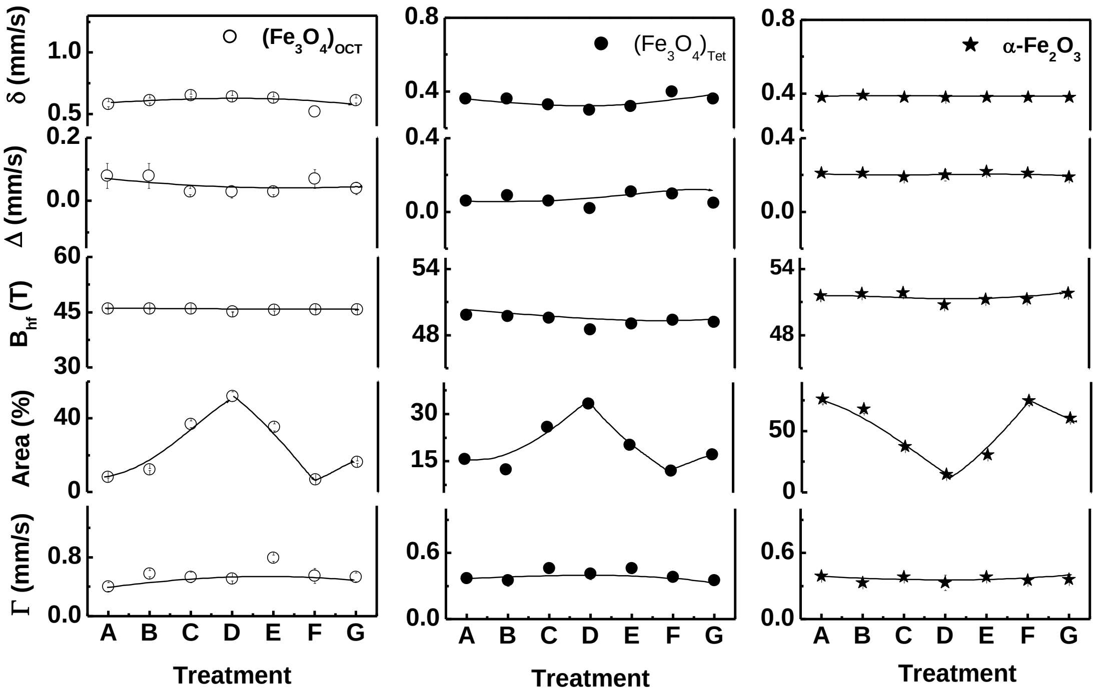

Figure 3.16: Variations of the magnitudes of hyperfine parameters correspond to fractions of Fe atoms occupying tetrahedral, octahedral sites and α-Fe_2O_3 particles after treatment A, B, C, D, E, F and G as mentioned in Table-3.4.

The activation energy required to create oxygen vacancies in α-FeOOH is much higher than 373 K. As the annealing temperature increases the energy was sufficient to drive away oxygen leading to the reduction of the α-FeOOH to a cubic structure iron oxide. Further increase in the annealing temperature beyond 470 K results in oxygen vacancies resulting in a rearrangement Fe in cubic manner leading to the formation of cubic phase as shown schematically in Figure 3.11.

3.7 Conclusion

Summarizing this work brings out a detailed understanding of the evolution of local structure and magnetic properties of α-FeOOH nano particles due to controlled thermal reduction using Mössbauer spectroscopic studies. Important role played by hydrogen in the partial conversion of orthorhombic α-FeOOH to cubic phases such as γ-Fe_2O_3 and reduction to Fe_3O_4 in the temperature regimes 400-460 K and 500-625 K respectively has been elucidated in the present study for the first time using Mössbauer spectroscopy. Proton desorbed from α-FeOOH are understood to create oxygen vacancies thus increasing the concentration of Fe ions locally which diffuse in a stacked manner to result in a partial conversion of α-FeOOH to cubic γ-Fe_2O_3. Variations in hyperfine parameters corresponding to tetrahedral and octahedral sites of associated off stoichiometric magnetite particles due to thermal reduction of α-FeOOH nano particles have been discussed in the present study thus providing a better understanding of the thermal reduction of α-FeOOH and interaction between desorbed species such as OH^-, H_2 and O^{2-} with Fe atoms associated with Fe_3O_4. Topotactical formation of α-FeOOH to α-Fe_2O_3 is observed for annealing treatments above 500 K and this effect becomes predominant for annealing above 650 K. Results of this study might be useful for obtaining anisotropic nano particles of iron oxides from α-FeOOH thus exploiting the large aspect ratio of the nano α-FeOOH particles in a controlled manner.

3.8 References

[1] J.P. Jolivet, C. Chaneac, P. Prene, L. Vayssieres and E. Tronc, *J. Phys. IV France*, **7**, C1-573 (1 997)

[2] Y. Qu, H. Yang, N. Yang, Y. Fan, H. Zhu, G. Zou, *Mater. Lett*., **60**, 3548 (2006)

[3] L. Vayssieres, C. Chaneac, E. Tronc and J. P. Jolivet, *J. Colloid Interf. Sci*., **205**, 205 (1998)

[4] F. Schüth, M. Hesse, K.K. Unger, *Precipitation and coprecipitation*, Handbook of Heterogeneous Catalysis, Wiley-VCH Verlag GmbH & Co. KGaA, Germany (2008)

[5] Y. Qu, H. Yang, N. Yang, Y. Fan, H. Zhu, G. Zou, *Mater. Lett.,* **60**, 3548 (2006)

[6] C. Ban, Z. Wu, D. T. Gillaspie, L. Chen, Y. Yan, J. L. Blackburn, and A. C. Dillon, *Adv. Mater*., **22**, E145 (2010)

[7] J. M. D. Coey, A. Barry, J. Brotto, H. Rakoto et al., *J. Phys.: Condens Matter*, **7**, 759 (1995)

[8] T. K. McNab, R. A. Fox, and A. J. F. Boyle, *J. Appl. Phys.* **39**, 5703 (1968)

[9] B. Zheng, M. Zhang, D. Xiao, Y. Jin, M. M. F. Choi, *Inorg. Mater*., **46**, 1106 (2010)

[10] S.K. Sahoo, K. Agarwal , A.K. Singh, B.G. Polke and K.C. Raha, *Inter. J. Eng., Sci. Tech.*, **2**, 118 (2010)

[11] S. Ayyappan, J. Philip, B. Raj, *Mater. Chem. and Phys*., **115**, 712 (2009)

[12] Baoping Jia and Lian Gao, *J. Am. Ceram. Soc*., **89,** 1739 (2006)

[13] C. B.-Andujar, D. Ortega, Q. A. Pankhurst and N. T. K. Thanh, *J. Mater. Chem*., **22**, 12498 (2012)

[14] T. Ahn, J. H. Kim, H.-M. Yang, J. W. Lee, and J.-D. Kim, *J. Phys. Chem. C,* **116**, 6069 (2012)

[15] G. Gnanaprakash, S. Mahadevan, T. Jayakumar, P. Kalyanasundaram, J. Philip, B. Raj, *Mat. Chem. Phys*. , **103**,168 (2007)

[16] A. Olowe and J. M. R. Genin , Corros sci **32,** 965 (1991)

[17] T. Kamimura, S. Nasu, T. Tazaki, K. Kuzushita and S. Morimoto, *Material Transactions*, **43**, 694 (2002)

[18] G. Wang, G. Whittaker, A Harrison and L. Song, *Mater. Res. Bull*., **33**, 1571 (1998)

[19] O. Ozdemir and D. J. Dunlop, Earth. Planet. Sci. Lett., **177**, 59 (2000)

[20] T. Iwasaki, N. Sato, K. Kosaka, S. Waano *et al.*, *J. Alloys & compounds*, **509**, L34 (2011)

[21] D. E. Madsen, L. C. Gontard, T. Kasama, R. E. D. Borkowski, C. B. Koch et al., *J. Phys.: Condens. Matter*, **21**, 016007 (2009)

[22] H. Naono and R. Fujiwara, *J. Colloid Interface Sci.* **73**, 406 (1980)

[23] L. Diamandescu, D. M. Tãrãbãşanu, and S. Calogero, *Mater. Chem . Phys*., **48**, 170 (1997)

[24] D. Walter, G. Buxbaum, and W. Laqua, *J. Therm. Anal. Calorim*, **63**, 733 (2001)

[25] H. Fan, B. Song, and Q. Li, Mater. *Chem. Phys*., **98**, 148 (2006)

[26] W. J. Zhang, C. F. Huo, G. Feng, Y. W. Li et al., *J. Mol. Struc.: Theochen*, **950**, 20 (2010)

[27]S. Bocquet, R. J. Pollard, and J. D. Cashion, *Phys. Rev. B* **46**, 11657 (1992)

CHAPTER 4

STABILITY OF MAGNETITE NANOPARTICLES CAPPED WITH OLEIC ACID

Chapter 4

STABILITY OF MAGNETITE NANOPARTICLES CAPPED WITH OLEIC ACID

4.1 Introduction

Magnetite nanoparticles are being widely used for a number of applications in medical science and technology [1,2]. It is very important to have mono dispersed particles with size ranging up to a few nm and of required shape depending upon the application. [3,4]. As the particle size decreases the surface effect becomes more significant due to the increase in the surface to volume ratio of the particle [5], therefore the nanoparticles become highly reactive and unstable [6]. Hence along with controlling the size and shape one needs to monitor the stability (i.e. thermal as well as chemical) of the nanoparticles. One way of maintaining the physical and chemical stability of nanoparticle is to cap these with surfactant [6] suitable for the concerned application [7]. Surfactants can modify the magnetic interactions between nanoparticles as the dipole interaction varies inversely as the cube of the interparticle distance. This has been demonstrated using SiO_2 coating on magnetite nanoparticles [7].

Oleic acid (OA) has emerged as one of the most common surfactants exhibiting covalent bonding with magnetite nanoparticles [1,4,7,8]. It has also been reported that the surface canted spins are compensated using oleic acid [8]. Issues related to stability of oleic acid capped magnetite nanoparticles are yet to be understood completely. This chapter focuses on the aspects related to the stability of oleic acid capped magnetite nanoparticles using

Mössbauer spectroscopy. Also this chapter provides an understanding of obtaining different possible core-shell structures of magnetite exhibiting different magnetic ordering.

The bare nano particles were synthesized following the procedure as mentioned in section 2.2 (Cf. Figure 2.1 & 2.2). Precipitate solution formed using co-precipitation method as discussed earlier was separated into two half. In one half of about 150 ml of the precursor solution 8 ml of OA was added and then stirred for 30 min at 348 K. The precipitate is then washed and dried. In both these cases of sample preparation the particles are extracted with magnet. The bare nanoparticle is referred to as M2 as studied in Chapter 3 and M2OA for oleic acid capped nanoparticles.

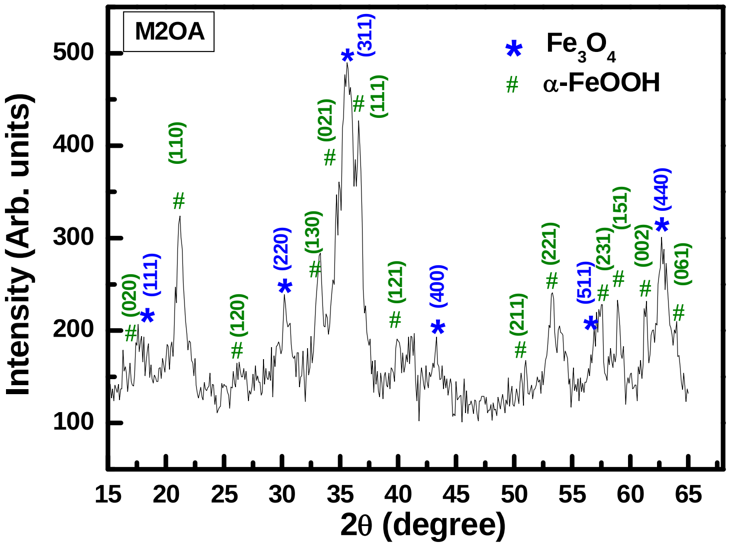

Figure 4.1: XRD spectrum of oleic acid capped nano particles prepared using co-precipitation method indicating the existence of α-FeOOH and Fe_3O_4.

XRD of the bare (Cf. Figure 3.2 corresponding to M2) and OA capped nanoparticles (Cf. Figure 4.1) are almost identical and shows the presence of α-FeOOH and Fe_3O_4. Based on the Scherrer analysis the mean size of uncapped or bare nano particles of α-FeOOH and Fe_3O_4 were deduced to be around 11 nm and 6 nm. The mean size of OA capped nano particles of α-FeOOH and the magnetite were deduced to be around 12 nm and 8 nm respectively. Thus XRD results indicate that the phases and the size of the nano particles obtained in the case of uncoated and oleic acid coated samples are roughly the same providing a good platform for studying in detail about the influence of oleic acid capping on local structure and magnetic properties by means of comparison of the results.

Mössbauer results pertaining to bare nano particles (hence forth referred to as case-A) would be discussed first and would be compared with that of nano particles capped with oleic acid (case-B) in order to understand the influence of oleic acid surfactant on the stability, evolution of local structure and magnetic properties due to controlled annealing treatments.

4.2 Thermal evolution of bare nano particles of Magnetite / oxy hydroxides

Mössbauer spectrum obtained in the as prepared condition of sample containing bare nano particles of magnetite as described in chapter 3 (section 3.2, Figure 3.4(M2)) could be deconvoluted into a doublet and three sextets. Fe atoms exhibiting superparamgnetism consist of 35 %, 45 % of Fe atoms are associated with the surface of nano particles, 18 % of Fe atoms are deduced to be associated with crystallite goethite based on the reported hyperfine parameters [9] and close to 3 % of Fe atoms experience hyperfine parameters as that of γ-Fe_2O_3. Annealing treatment at 423 K results in a decrease in the fraction of iron atoms associated with superparamagnetic particles by 11 %, disordered spins by 7 % and that of γ-Fe_2O_3 by 3 %. Two sextets characterized by hyperfine fields close to 44.8 and 48.5 Tesla and isomer shifts of 0.42 and 0.33 mm/sec could be understood to be due to Fe atoms occupying octahedral and tetrahedral sites of off-stoichiometric magnetite respectively.

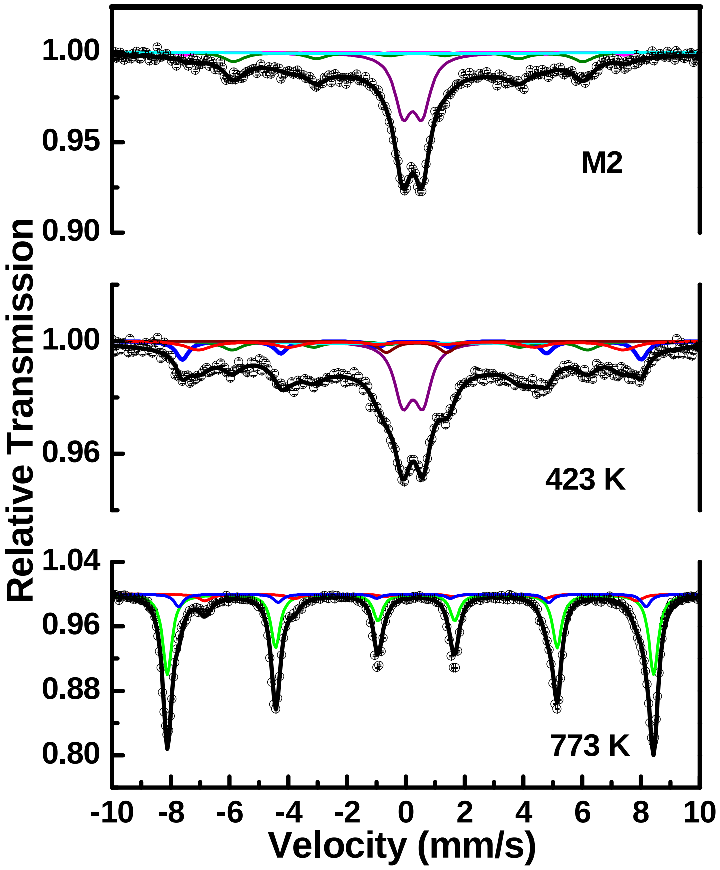

Figure 4.2. Mössbauer spectra obtained in the uncapped nano particles of magnetite prepared using co precipitation method (M2) and subsequent to each annealing treatment at 423 and 777 K at 10^{-6} mbar for 1 hour. These spectral features mainly exhibit the coarsening of super paramagnetic particles resulting mainly in the topotactic conversion of α-FeOOH to α-Fe_2O_3 in addition to showing the occurrence of magnetite. Details are referred to the text.

Table-4.1. Shown are the values of hyperfine parameters as experienced by ^{57}Fe resonant absorber atoms associated with different phases existing in the bare nano particles of magnetite and iron oxyhydroxides in the as prepared condition and annealed at different temperatures as indicated.

Sample /Annealing temperature	**i**	**Γ_i (mm/s)**	**δ_i (mm/s)**	**Δ_i (mm/s)**	**B_{hf}^{i} (T)**	**f_i (%)**
M2	1	0.69(2)	0.35(0)	0.65(1)	-	34(0)
	2	5.10(3)	0.34(9)	-0.32(3)	22.3(5)	45(2)
	3	0.84(9)	0.36(2)	-0.30(4)	36.8(4)	18(0)
	4	0.67(7)	0.34(0)	-0.04(0)	45.9(5)	03(1)
423 K	1	0.85(4)	0.35(1)	0.73(2)	-	24(1)
	2	5.10(0)	0.31(9)	-0.15(8)	18.8(6)	37(2)
	3	1.28(4)	0.39(3)	-0.21(6)	37.8(3)	19(1)
	5	0.78(8)	0.41(0)	-0.07(0)	45.3(3)	12(0)
	6	0.51(8)	0.35(2)	-0.07(3)	48.6(9)	08(0)
773 K	5	0.53(2)	0.60(1)	0.05(1)	45.5(5)	13(0)
	6	0.37(2)	0.36(0)	-0.04(0)	49.3(4)	12(1)
	7	0.37(0)	0.38(0)	-0.20(0)	51.3(1)	75(0)

f_1, f_2 are fractions of Fe atoms associated with super paramagnetic and disordered surface spins of nano particles respectively. Fractions f_3, f_4 and f_7 of Fe atoms are associated with crystallite goethite, γ-Fe_2O_3, haematite respectively, while f_5 and f_6 represent Fe atoms occupying octahedral and tetrahedral interstitial sites of Fe_3O_4.

The occurrence of off stoichiometric magnetite with a relative fraction of 20 % in the sample annealed at 423 K is comprehended mainly due to partial reduction of super paramagnetic particles of α-FeOOH and crystalline off stoichiometric magnetite. Based on this understanding it should result in 21×2/3 ≈ 14 % of Fe atoms associated with octahedral sites and 21×1/3 ≈ 7 % of Fe atoms associated with tetrahedral sites of magnetite, which match well with the observed values of tetrahedral and octahedral fractions associated with magnetite (Cf. Figure 4.2 & Table-4.1). A smaller value of isomer shift (0.42 mm/sec) corresponding to octahedral sites instead of 0.67 mm/sec corresponding to that of bulk magnetite implies that the particles contain lesser Fe^{2+} due to partial oxidation. Subsequent to annealing at 523 K a decrease in the fraction of Fe atoms associated with crystallite goethite by 6 %, surface and core of super paramagnetic particles by 18 % and 14 % respectively is seen. Occurrence of 15% of α-Fe_2O_3 is understood to be due to a topotactic conversion of crystalline α-FeOOH whose relative fraction is close to 17 % in the starting sample. Decrease in the fraction and line width corresponding to Fe atoms associated with disordered spins is understood to be due to coarsening of the nano particles. Annealing at 773 K results in the occurrence of 75 % of α-Fe_2O_3 and 25 % of Fe_3O_4 nano particles. Occurrence of α-Fe_2O_3 by a relative fraction of 75 % could be understood due to a topotactic conversion of α-FeOOH to α-Fe_2O_3 which might be predominantly taking place for annealing beyond 500 K [10-16]. This would mean that the starting sample might be composed of the nano particles of α-FeOOH and off stoichiometric magnetite in the ratio of 75 % and 25 % respectively. The evolution of local structure and magnetic properties of the nano particles of iron oxy hydroxide and magnetite capped with oleic acid will be discussed in the following.

4.3 Thermal evolution of oleic acid (OA) capped nano particles of off-stoichiometric magnetite and hydroxides of Fe

Mössbauer spectrum and hence the hyperfine parameters as experienced by ^{57}Fe absorbers associated with OA coated magnetite nano particles (Cf. Figure 4.3 and Table-4.2) remain closely similar to that of uncoated ones with respect to phases of oxides / oxy hydroxides of

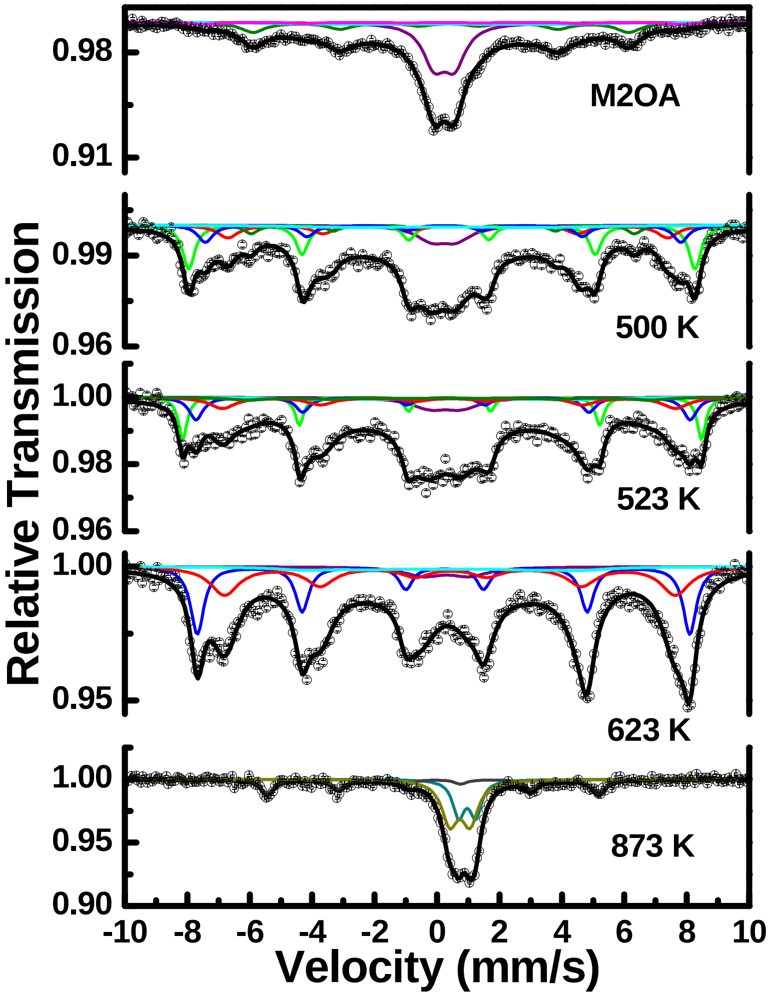

Figure 4.3: Mössbauer spectra obtained in the oleic acid capped nano particles of magnetite prepared using coprecipitation method and subsequent to annealing treatments at different temperatures and a partial pressure of 10^{-6} mbar. Mössbauer spectrum remains almost similar in the OA capped nano particles of magnetite as that of bare ones. Remaining spectra exhibit altogether different features with respect to annealing treatments from that of bare nano particle showing an accelerated reduction of goethite to stoichiometric magnetite, Wustite and Fe. Details are referred to the text.

Fe implying almost a similar local structure, magnetic properties in both the cases. Thus the procedure adopted in this work to prepare uncapped and OA capped nano particles has resulted in almost a similar result with respect to size and phases of the nano particles formed. However there is some important differences *viz.*, the smaller fraction of Fe atoms associated with disordered spins in the case of OA capped than that of bare nano particles implying that the capping has resulted in a reduction in spin fluctuation. This is due to covalent bonding of the carboxylic group of OA molecule with the surface of nano particles. Fraction of crystallite goethite is slightly larger in the case of OA capped than that of bare nano particles, while the relative fractions of magnetite remain almost same in both the cases. Mössbauer results obtained in the sample annealed at 500 K for 4 hrs show that the fraction of Fe atoms associated with crystallite goethite has got reduced by 10 % resulting in a complete topotactical conversion of α-FeOOH to α-Fe_2O_3. As the cover density on the nano particle surface would decrease drastically due to an increase in the particle size, large crystallite particles of α-FeOOH will be very less or nil capped with OA resulting in the topotactic transformation to α-Fe_2O_3 due to annealing at 500 K. The fractions of Fe atoms associated with γ-Fe_2O_3 and superparamagnetic particles of magnetite have been observed to be 0 and 18 % respectively subsequent to annealing at 500 K. As high as 25 % of Fe atoms are observed to be associated with Fe_3O_4 which is understood to be mainly due to partial reduction of superparamagnetic particles of α-FeOOH and γ-Fe_2O_3.

Based on the observed values of hyperfine parameters corresponding to Fe atoms occupying octahedral and tetrahedral sites of magnetite, the reduction of α-FeOOH are mainly understood to be due to decomposition of Oleic acid as bound to nano particles of α-FeOOH.

Table-4.2. Hyperfine parameters as experienced by ^{57}Fe resonant absorber atoms associated with different phases existing in the Oleic acid capped nano particles of magnetite and iron oxy hydroxides in the as prepared condition and annealed at different temperatures.

Sample /Annealing temperature	i	Γ_i (mm/s)	δ_i (mm/s)	Δ_i (mm/s)	B_{hf}^i (T)	f_i (%)
M2OA	1	0.86(3)	0.35(1)	0.65(1)	-	36(1)
	2	3.73(9)	0.34(7)	-0.37(9)	23.9(9)	38(3)
	3	0.97(8)	0.37(2)	-0.26(3)	37.3(8)	22(1)
	4	0.83(8)	0.30(7)	-0.02(0)	47.5(5)	04(1)
500 K	1	1.27(9)	0.32(3)	0.8(3)	-	17(0)
	2	3.80(3)	0.47(3)	-0.05(2)	23.4(9)	34(4)
	3	0.52(3)	0.32(4)	0.06(2)	38.1(8)	05(1)
	5	0.82(4)	0.50(3)	-0.08(3)	43.7(6)	15(1)
	6	0.56(9)	0.34(2)	-0.05(0)	47.1(0.2)	10(2)
	7	0.47(3)	0.38(1)	-0.22(1)	50.2(1)	19(0)
523 K	1	1.42(9)	0.39(3)	1.02(8)	-	19(1)
	2	2.74(7)	0.37(2)	-0.15(3)	26.3(8)	26(3)
	3	1.46(9)	0.38(4)	0.22(5)	39.8(9)	11(1)
	4	1.02(8)	0.54(5)	-0.04(1)	44.9(9)	22(1)
	5	0.56(6)	0.36(3)	-0.06(2)	49.01(9)	12(0)
	6	0.35(3)	0.40(4)	-0.24(5)	51.5(9)	10(1)
623 K	1	1.49(9)	0.41(4)	1.50(6)	-	12(1)
	2	2.23(0)	0.37(9)	-0.21(5)	27.23(9)	19(2)
	3	1.11(3)	0.55(1)	-0.03(2)	44.79(9)	45(0)
	4	0.52(0)	0.35(1)	-0.04(1)	48.91(4)	24(1)
873 K	8	0.60(6)	0.95(2)	0.51(3)	-	64(0)
	9	0.44(3)	0.87(3)	1.08(5)	-	13(1)
	10	0.5(4)	0.02(1)	-0.05(3)	32.9(9)	23(0)

f_1, f_2 are fractions of Fe atoms associated with super paramagnetic and disordered surface spins of nano particles respectively. Fractions f_3, f_4, f_5, f_6 and f_7 of Fe atoms associated with crystallite goethite, γ-Fe_2O_3, octahedral sites of Fe_3O_4, tetrahedral sites of Fe_3O_4 and α-Fe_2O_3 respectively.

Bare nano particles of α-FeOOH were seen to get reduced to off-stoichiometric magnetite (Cf. Table-4.1) for annealing around 425 K.

Annealing at 523 K results in a decrease in the fraction of Fe atoms associated with superparamagnetic particles by 19 %, crystallite γ-Fe_2O_3 by 3 % and canted spin by 13%. Reductions of fractions of Fe atoms as seen above might be resulting in $2/3\times35\ \% \approx 23\ \%$ and $1/3\times35\ \% \approx 12\ \%$ of Fe atoms associated with octahedral and tetrahedral sites of Fe_3O_4. This matches well with the experimental result on the fractions of Fe atoms associated with octahedral (22 %) and tetrahedral sites (12 %) of Fe_3O_4. The values of isomer shifts, hyperfine fields and the ratio of cationic population of octahedral and tetrahedral sites match quite closely with those reported in the literature [17] implying the formation of stoichiometric magnetite. The hyperfine fields corresponding to tetrahedral and octahedral sites in the nano particles of magnetite formed due to reduction of nano particles of α-FeOOH are lesser than that of bulk stoichiometric magnetite.

Occurrence of 35 % of Fe_3O_4 which is about 10 % higher than that of the sample subjected to similar annealing treatment at 500 K for 4 h (Cf. Table-4.2) brings out clearly the decomposition of oleic acid bound to α-FeOOH to result in the reduction of α-FeOOH to Fe_3O_4. Comparison of the results obtained due to annealing treatment at 500 K for 4 h with that of the treatment at 523 K for 1 h thus shows a strong dependence of the binding of oleic acid with the nano particles on the temperature of dissociation of oleic acid. Out of 22 % of the fraction of Fe atoms associated with crystallite goethite in the starting sample, there is a decrease in this fraction by 11 % while the remaining is associated with α-Fe_2O_3 which is understood to be formed due to topotactical conversion of α-FeOOH following annealing at 523 K.

Annealing at 623 K results in the formation of nearly stoichiometric magnetite with the fractions associated with tetrahedral and octahedral sites are 45 % and 23 % respectively. A reduction of fractions associated with super paramagnetic, fine nano particles (10 nm < r < 20 nm), crystallite goethite by about 24 %, 18 % and 22 % respectively accompanied with the reduction of 4 % of γ-Fe_2O_3 is seen subsequent to annealing at 623 K. Hence this is expected to result in the formation of 46 % (≈ 2/3×68 %) and 23 % (≈1/3×68 %) of Fe atoms associated with octahedral and tetrahedral sites of Fe_3O_4 respectively matching quite well with the experimental results. This result elucidates the important role of oleic acid resulting in the reduction of α-FeOOH to Fe_3O_4. The increased formation of the fraction associated with magnetite could be comprehended mainly due to coarsening and subsequent reduction of α-FeOOH to Fe_3O_4 which is dominantly seen for annealing beyond 525 K due to decomposition of OA. This might imply an increase in the interaction cross section between surface of even coarse particles with decomposing oleic acid at high temperature thus resulting in the reduction of both superparamagnetic and fine nano particles along with crystalline α-FeOOH particles to off stoichiometric magnetite due to annealing beyond 525 K. Reduction of α-FeOOH to Fe_3O_4 becomes predominant beyond 550 K due to decomposition of free oleic acid and in addition to the ones bound to α-FeOOH.

The fraction of Fe atoms associated with Fe_3O_4 remain almost constant around 65% in the annealing interval 530 K < T < 725 K. This implies that the Fe_3O_4 nano particles once formed due to reduction of α-FeOOH remain quite stable in the above temperature range comprehended due to a strong binding between the surface of OA and the surface of Fe_3O_4 nanoparticles. The effect of further reduction of Fe_3O_4 to FeO is seen subsequent to the annealing treatment at 773 K. These results in the reduction of the fraction associated with magnetite to 31 %. Component with high isomer shift (0.6 mm/sec) and quadrupole splitting (0.84 mm/sec) is attributed to Fe atoms associated with FeO while the one exhibiting low field, large quadrupole splitting and large line width is understood to be due to Fe atoms occupying the surface of super paramagnetic particles of Fe_3O_4. Surfactant adsorption by nanoparticles is dependent upon the particle size. It has been reported based on single layer adsorption model that the cover density of OA capped Fe_3O_4 nano particles of mean size roughly about 7 nm is as high as 95 % while that for a larger sized particle of the order of 20 nm there is a sharp decrease in the cover density by 60 % [18].

Size dependence of nanoparticles on the concentration of COO^- of OA surfactants as bonded to nanoparticles has been established through the Mössbauer result corresponding to annealing at 523 K in OA capped nano particles. The reduction of α-FeOOH to Fe_3O_4 is seen in the annealing interval $500<T<600$ K. The reduction of Fe_3O_4 is based on the following generalized reaction such as

$$pFe_3O_4 + (q+r)C \rightarrow qCO_2\uparrow + rCO\uparrow + sFe + tFeO$$

The fraction associated with Fe_3O_4 remains constant in the range $600 < T<700$ K, while the reduction of Fe_3O_4 to FeO and Fe is seen only beyond 700 K. This shows that the temperature of dissociation of OA capped to α-FeOOH is much lesser compared to that of Fe_3O_4 particles capped with OA implying importantly that the Fe_3O_4 nano particles are likely to be more strongly bound to OA than that of α-FeOOH particles of same size.

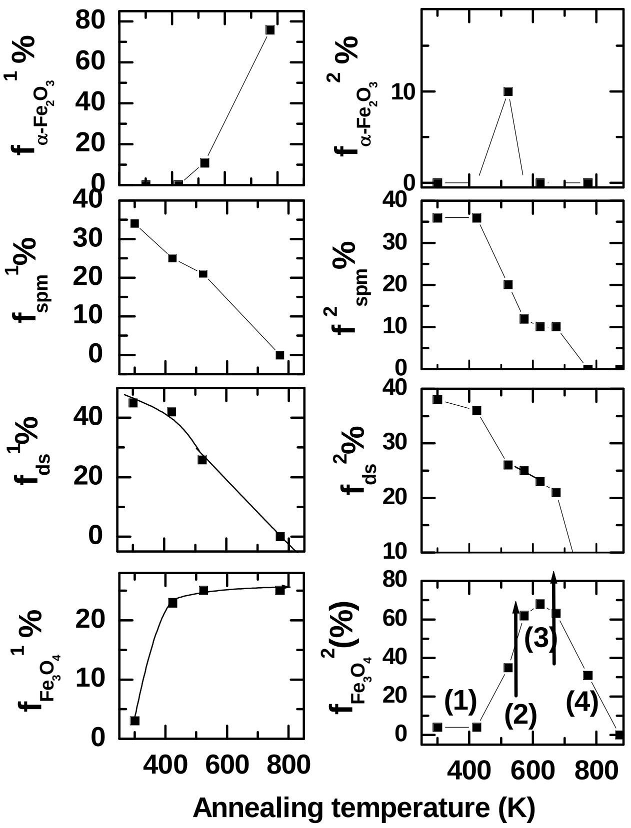

Figure 4.4: Variations of fractions Fe atoms associated with super paramagnetic (SPM) particles composed of α-FeOOH and magnetite, surface of nanoparticles exhibiting disordered spin and off-stoichiometric magnetite (coarsened) of uncapped and OA capped nano particles obtained based on the analysis of Mössbauer spectra. These results exhibit a monotonous change in the case of uncapped nanoparticles in which the topotactic transformation of α-FeOOH to α-Fe_2O_3 takes place predominantly. In the case of OA capped nano particles accelerated reduction of α-FeOOH to Fe_3O_4 occurs in the interval 500-600 K. Annealing treatments beyond 700 K results in a reduction of Fe_3O_4 to FeO and subsequently to α-Fe.

Shown in Figure 4.4 are the variations of fractions of Fe atoms associated with bare and OA capped nano particles with annealing temperature. In the case of bare NP, formation of cubic fraction assigned to off-stoichiometric magnetite has been observed. Annealing at 500 K results in the onset of topotactic conversion of α-FeOOH to α-Fe_2O_3 reaching as high as 75% subsequent to annealing treatment at 773 K. In the case of OA capped nano particles four temperature regime could be deduced based on the variations of fractions of Fe atoms viz., $T< 425$ K, $450 \text{ K} < T < 600$ K, $620 \text{ K} < T < 700$ K and $T > 730$ K. Temperature regime $T < 425$ K indicates a strong binding of OA with super paramagnetic particles of α-FeOOH and Fe_3O_4 thus resulting in constant value of f_{spm}. Annealing results in the temperature regime $450 \text{ K} < T < 600$ K lead to a decrease in the values of f_{spm} and f_{ds}, which is understood due to the reduction of α-FeOOH to Fe_3O_4 due to carbon monoxide that gets dissociated due to partial decomposition of OA bound to α-FeOOH. Though α-FeOOH would tend to get topotactically converted in to α-Fe_2O_3, there would be strong reduction due to carbon monoxide dissociated from OA thus resulting in reduction to Fe_3O_4. This is understood to be due to an increase in the cross section for reduction of even crystalline α-FeOOH particles with increasing annealing temperature. In the annealing interval $550 < T < 700$ K the values of f_{spm} and f_{ds} remain almost constant, concomitant with the constant value of fraction of Fe atoms associated with Fe_3O_4. This shows that the carboxylic group is strongly bound to Fe_3O_4 nano particles in the above temperature regime. Beyond 730 K there is a strong decrease of Fe_3O_4 resulting in its reduction to FeO and α-Fe. These results clearly establish that the nano particles of α-FeOOH and Fe_3O_4 are bound by Oleic acid with different values of binding energy resulting in the reduction of the above particles to Fe_3O_4

and FeO/Fe respectively at widely different annealing temperatures. Variations in the binding of Iron oxy hydroxide and oxide nano particles by Oleic acid are comprehended as follows.

4.4 Binding of α-FeOOH and off-stoichiometric magnetite nanoparticles by OA

TGA derivative curve obtained on magnetite nano particles capped with OA based on the results reported by Zhang et al [18] indicates the occurrence of two distinct transitions in the vicinity of 550 K and 650 K respectively. The two distinct transitions were plausibly interpreted [18] to be due to two possible states of Iron. The present Mössbauer results corresponding to the variation of fractions of Fe atoms associated with super paramagnetic particles, disordered spins show sharp changes around temperatures 550 and 650 K which were understood to be mainly due to reductions of α-FeOOH and Fe_3O_4 respectively. The annealing stages as observed in the Mössbauer results showing the onset of reduction of α-FeOOH to Fe_3O_4 and Fe_3O_4 to FeO match with the temperatures of two distinct transitions as deduced based on TGA results [18]. The present results indicate that the Fe_3O_4 nanoparticles are more strongly bound to OA than that of α-FeOOH particles.

Larger binding energy of Fe_3O_4-OA than that of α-FeOOH-OA is understood as follows. Bonding between a nano particle and a surfactant is quite likely to be dictated by the charge state of the defects at the surface of nano particles and the surface of the surfactant. Size of the nano particles should also be playing an important role in providing the binding to any surfactant in addition to valence effect. Smaller size of Fe_3O_4 than α-FeOOH nano particles might imply more surface area with larger number of dangling bonds in the case of Fe_3O_4 nanoparticles for bonding with OA. Surface of Fe_3O_4 are likely to be characterized with oxygen vacancies which are effectively of charge +2 [19]. Nanoparticles of α-FeOOH are

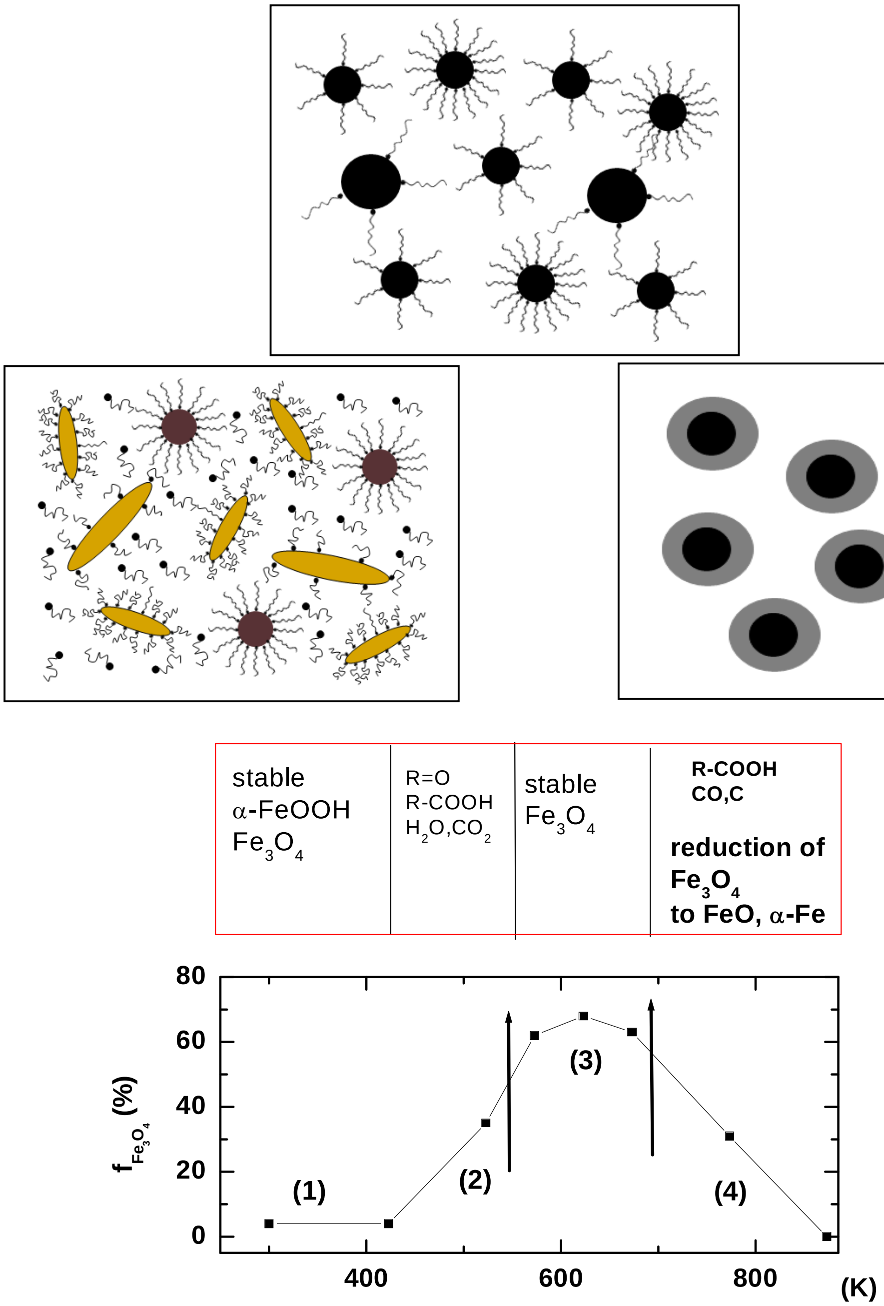

Figure 4.5. Various stages involved in dissociation of oleic acid bound to iron oxy hydroxide and oxide nano particles leading to the reduction of oxyhydroxide of α-FeOOH to Fe_3O_4 then to FeO/Fe.

characterized with OH^- vacancies which carry an effective charge of +1. OA is characterized to be of negatively charged due to occurrence of cationic vacancies at their surface leading to the inference that Fe_3O_4 nanoparticles could be more strongly bound to COO^- group than that of α-FeOOH particles of almost same size. Reduction of a nanoparticle is observed mainly due to the decomposition of OA as bound to the particle. Present results indicate the decomposition of free oleic acid around 520 K based on the partial reduction of crystallite goethite to which almost no oleic acid is likely to be bound. Annealing treatment beyond 550 and 750 K results in the decomposition of oleic acid bound to α-FeOOH and Fe_3O_4 nano particles respectively. Hence a strong binding between a nano particle and a surfactant might imply a significantly high temperature of dissociation of OA leading to reduction of the nano particles concerned. Various stages involved in dissociation of oleic acid bound to iron oxy hydroxide and oxide nano particles leading to the reduction have been schematically presented in Figure 4.5. Controlled annealing treatments cause partial dissociation of oleic acid which in turn results in reduction of a few surface layers of an oxide. This makes possible to obtain different oxides in core-shell configuration with varying structure and magnetic ordering as illustrated in the following discussion.

4.5 Core-shell structures deduced due to annealing treatments of OA capped NP beyond 700 K

Annealing of oleic acid capped nano particles of magnetite beyond 700 K is observed to result in the complete dissociation of oleic acid as shown by TGA result by Zhang et al [18]. Based on this result it is important to note that in addition to significant reduction there would be an appreciable coarsening of magnetite nano particles for annealing beyond 700 K.

Therefore annealing treatments in the range of 800 K and beyond would likely to result in nano particles in core-shell configurations with different structural and magnetic ordering mainly dictated by varying concentration of Fe^{2+} and Fe^{3+}.

Annealing at 820 K is seen to result in two doublets one with the value of isomer shift $\delta \approx 0.98$ mm/sec and a quadrupole splitting $\Delta \approx 0.6$ mm/sec ascribed to Fe atoms associated with close to stoichiometric FeO. On the other hand the other doublet is characterized by a much lower isomer shift $\delta \approx 0.5$ mm/sec and a larger value of quadrupole splitting $\Delta \approx 1.1$ mm/sec and is understood to be due to the presence of Fe^{3+} at the octahedral sites in addition to the occupation at tetrahedral interstitial sites in off stoichiometric wustite. Sample subsequent to the annealing at 820 K is observed to be weakly attractive as the whole by the magnet. Hence this annealing treatment is understood to result in a core-shell structure with core occupied by Fe atoms exhibiting lower isomer shift and higher quadrupole splitting while the shell is associated with Fe atoms experiencing higher isomer shift and lower quadrupole splitting.

4.6 Defects associated with FeO-Fe Core-shell structure

Mössbauer spectrum obtained subsequent to annealing at 873 K could be deconvoluted in to two doublets and a sextet. Two doublets are ascribed to two distinct sites of FeO exhibiting almost a similar value of isomer shift lying in the interval 0.8-1 mm/sec, while the ratio of the fractions experiencing low quadrupole splitting (0.52 mm/sec) to high quadrupole splitting ($\cong 1$ mm/sec) is around 0.83. Sextet exhibiting a hyperfine field close to 33 Tesla is understood to be due to the association of about 23 % of Fe atoms with α-Fe.

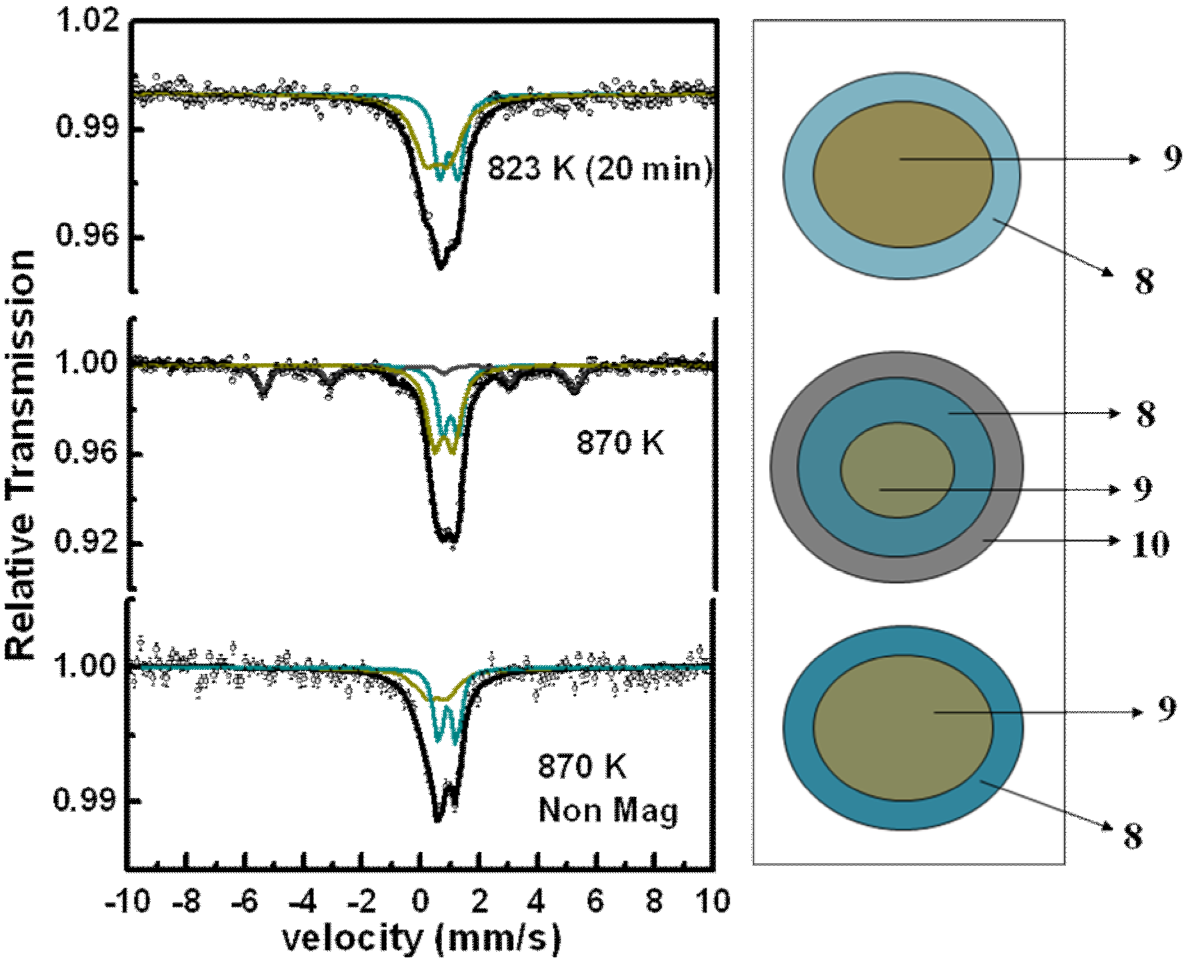

Figure 4.6: Mössbauer spectra of the M2OA annealed at 823 K for 20 min, 870 K for 1h and non magnetic portion of the 870 K treated sample. Schematics of the occurrence of core-shell structure of FeO-Fe particles are represented on the right hand column.

Wustite is understood to be off-stoichiometric (i.e.) $Fe_{1-x}O$ due to Fe^{2+} vacancies resulting in the occurrence of Fe^{3+} at tetrahedral interstitial sites. Also wustite being ionic lattice, the effective valence of oxygen vacancy would remain as +2. Increasing concentration of oxygen vacancies in the sample would result in building up of electrostatic repulsion between Fe cations and oxygen vacancies. Therefore annealing beyond 850 K is understood to result in the formation of Fe shell beyond a certain concentration of these oxygen vacancies in the core corresponding to wustite. Appreciable decrease in the quadrupole splitting of this defect associated doublet corresponding to wustite is expected to occur with increasing concentration of oxygen vacancies. At the cost of the fraction of Fe atoms associated with this defect component there would be an increasing formation of the shell of α-Fe.

The above sample could be separated in to two parts using a magnet viz., magnetically attractive and non-attractive. Mössbauer spectrum in the magnetically attractive part of the sample could be resolved in to two doublets and a sextet corresponding to FeO and Fe respectively with the hyperfine parameters remaining almost close to that of the total sample subjected to annealing at 870 K. This result implies the occurrence of core-shell structure of FeO-Fe particles as shown schematically in Figure 4.6. The occurrence of such core-shell structured particles of FeO-Fe could be comprehended due to the fact that annealing beyond 850 K should result in multiple stages of reduction due to decomposition of a large concentration of the carboxylic acid. The ratio of fractions experiencing low quadrupole splitting to high quadrupole splitting corresponding to two distinct doublet sites of FeO from the magnetically attractive part of the sample is seen to be around 0.78 which is close to that of the value of the above ratio as observed in the case of the complete sample.

Mössbauer spectrum obtained in magnetically non-attractive portion of the sample subsequent to annealing at 870 K shows the absence of sextet corresponding to α-Fe. Comparison of the results obtained in magnetically attractive and non-attractive portions of the samples shows that the fraction of Fe associated with wustite exhibiting higher isomer shift and lower quadrupole splitting is much smaller than that of the core component characterized by lower isomer shift and higher quadrupole splitting in the case of magnetically non-attractive than that of the attractive portion of the sample. From the non-attractive portion of the sample it is observed that the ratio of fractions experiencing low quadrupole splitting to high quadrupole splitting is deduced to be around only around 0.42. This means that off stoichiometric wustite core associated with doublets having a relatively large concentration of oxygen vacancies (i.e. larger fraction of doublet characterized by low quadrupole splitting compared to that of the doublet associated with high quadrupole splitting) could result in the Fe vacancies thus causing the occurrence of shell of α-Fe. Hence α-Fe is associated with off-stoichiometric wustite having appreciable concentration of oxygen vacancies. Therefore it is understood that the core wustite is composed of two regions viz., inner and outer core are understood to be due to $Fe_{1-x}O$ and $Fe_{1-x-\delta1}O_{1-\delta2}$ respectively. Inner $Fe_{1-x}O$ is understood to exhibit higher quadrupole splitting than that of outer core composed of $Fe_{1-x-\delta1}O_{1-\delta2}$. Increase in the concentration of oxygen vacancies results in an increase in Fe vacancies due to charge compensation which results in the formation of Fe at the shell.

It is seen from Figure 4.4 that the optimal formation of stoichiometric magnetite occurs following the annealing treatment at 623 K. Hence it is important to study the microstructure of the nanoparticles and to study the magnetic interactions. In the following the aspects related to microstructure and magnetic interactions between the nanoparticles of stoichiometric magnetite would be discussed based on the TEM, VSM and Mössbauer studies carried out on these stoichiometric magnetite nanoparticles.

4.7 Microstructural characterization of stoichiometric magnetite Nanoparticles

It is seen from the results on oleic acid coated sample that the annealing treatment at 623 K results in the association of about 70% of fraction of Fe atoms with stoichiometric Fe_3O_4 and the remaining with the superparamagnetic particles of magnetite.

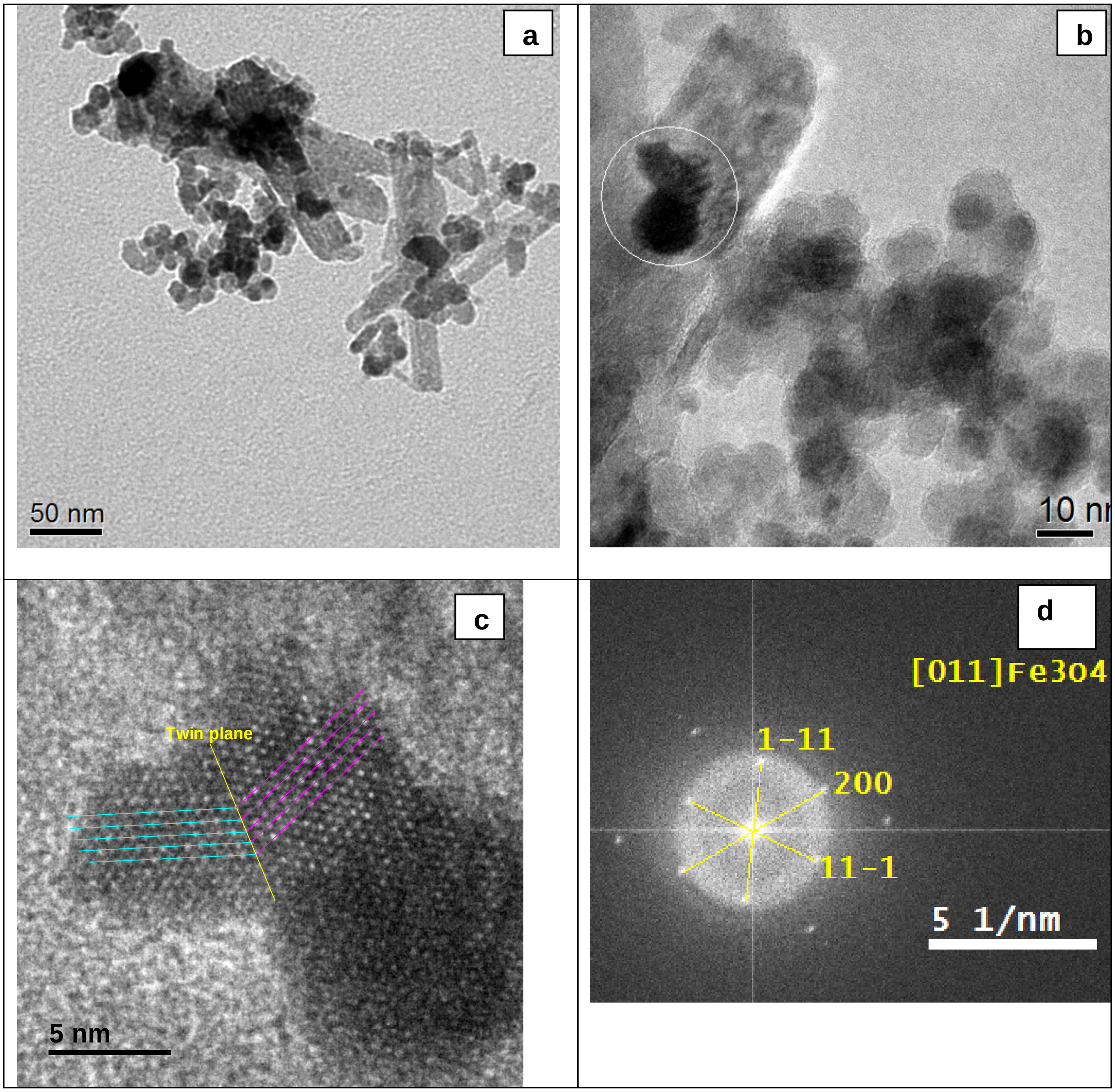

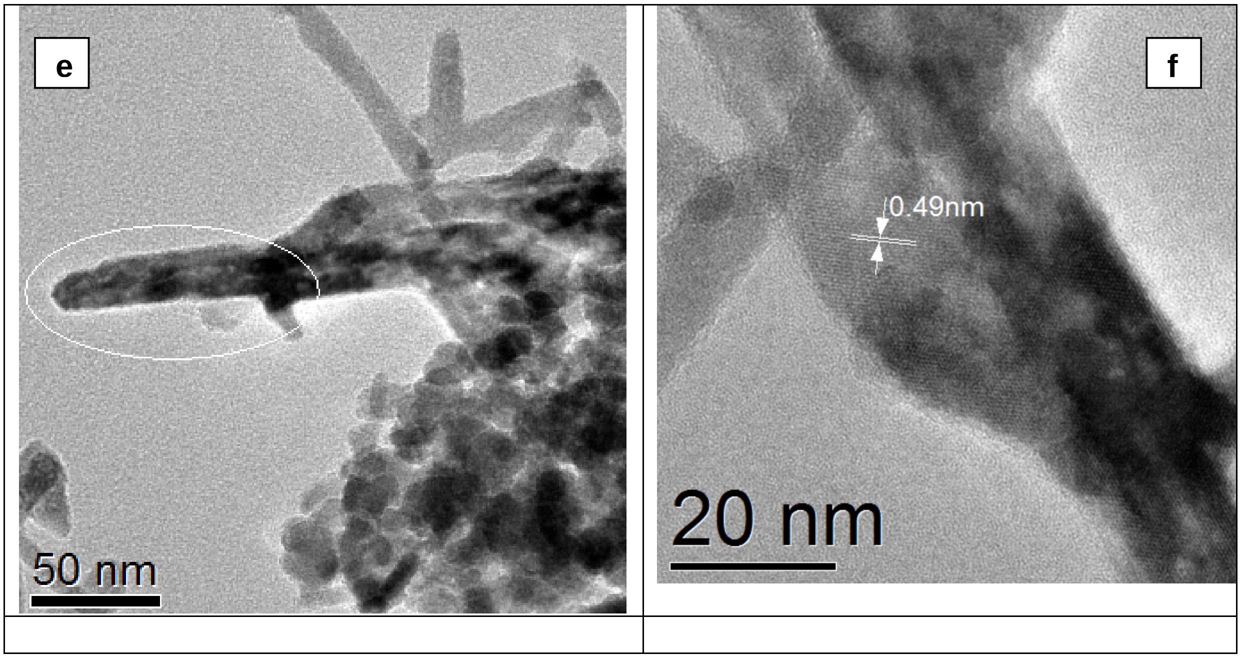

Figure 4.7: (a) shows a low magnification image showing the presence of both spherical and acicular particles, (b) shows a higher magnification image highlighting the particle from which Figure 4.7(c) is acquired. Figure 4.7(c) clearly shows the twinned crystals of Fe_3O_4 as confirmed by the FFT analysis shown in Figure 4.9(d). The zone axis is [011] and the twin plane is {111}, which is the most common twinning plane in fcc. The corresponding {111} planes are marked in Figure 4.7(b). The FFT analysis, shows the particle to be Fe_3O_4 along [011] zone axis. This clearly confirms that these rod shaped particles are also Fe_3O_4. Figure 4.7.(e) shows the image from a rod shaped particle, whose HREM image is shown in Figure (f).

TEM results indicate only the presence of Fe_3O_4 particles even in the rod as well as the spherical configurations.

4.8 Low temperature studies on Fe_3O_4 stoichiometric magnetite

M-H loop and magnetization measurements were carried out using VSM-SQUID. M-H loop measurements carried out under varying magnetic fields up to 5 Tesla shows that the sample exhibits ferromagnetism as evidenced by a hysteresis loop. The values of coercivity and retentivity are seen to be very small characteristic of nanometric nature of the sample concomitant with the XRD results showing that the average size of the magnetite particle lies around 12 nm. Magnetization results under zero field and field cooled conditions of the sample are presented in Figure 4.9. It is evident from the results that the bifurcation of ZFC and FC curves occur around 300 K implying that the particles are mostly of size in the range 10 nm < r < 20 nm. This also matches with the particle size profile as deduced using TEM studies.

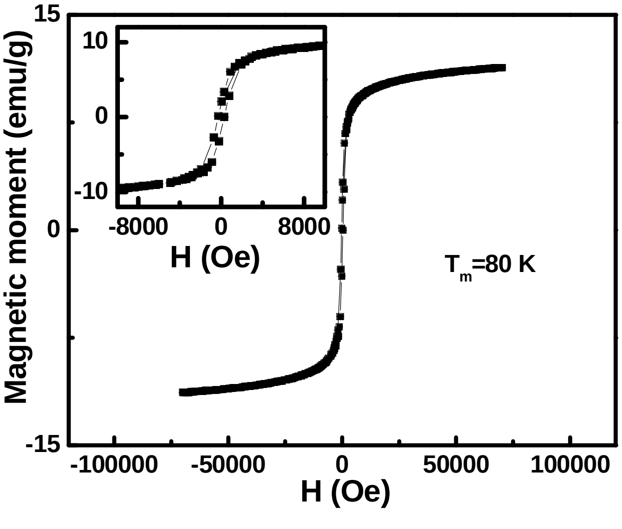

Figure 4.8: Result of M-H loop measurement carried out at 80 K in oleic acid coated magnetite nanoparticles subsequent to annealing treatment at 623 K.

The magnetization measurement carried out at 80 K shows an occurrence of hysteresis loop with a low value of coercivity and retentivity typical of magnetite nanoparticles. From the zero field cooled and field cooled magnetization curves it could be seen that the point of bifurcation occurs around 300 K. This is commensurate with the results of Mössbauer analysis indicating the association of about 75 % of ^{57}Fe atoms with magnetite nanoparticles of size close 20 nm. In the following the results of low temperature Mössbauer studies are discussed to understand verwey transition (i.e.) metallic to insulating transition which takes place around 120 K (Cf. Figure 1.3).

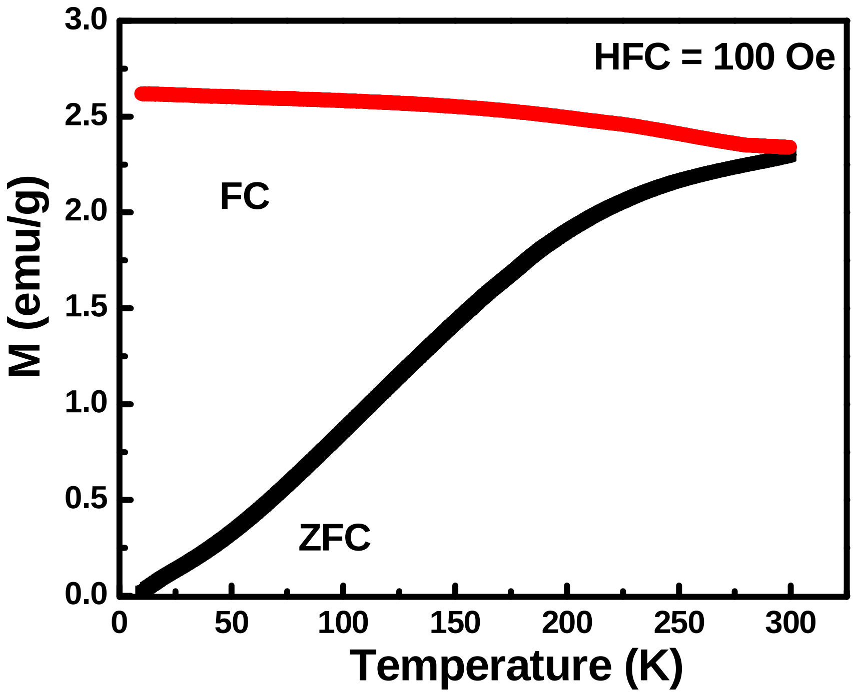

Figure 4.9: ZFC and FC of the 623 K annealed M2OA sample.

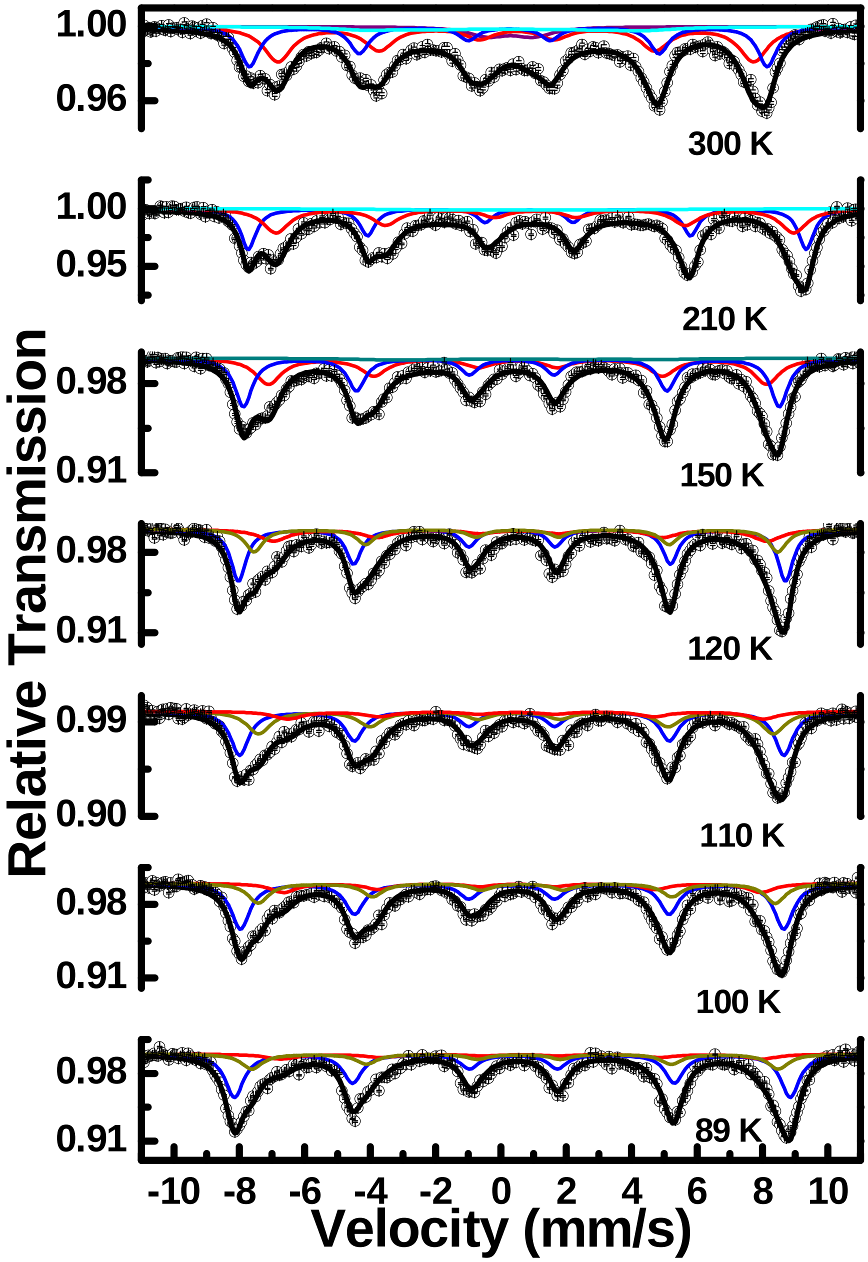

Figure 4.10: Mössbauer spectra obtained in stoichiometric magnetite nanoparticles at different temperature as mentioned.

Table 4.3: Hyperfine parameters as experienced by ^{57}Fe resonant absorber atoms of stoichiometric magnetite at different temperatures. The stoichiometric magnetite is obtained by means of annealing the OA coated magnetite nanoparticles at 623 K at partial pressure of 2×10^{-6} mbar.

Measurement temperature	**Γ (mm/s)**	**δ (mm/s)**	**Δ (mm/s)**	**B_{hf} (T)**	**f (%)**
300 K	1.42(9)	0.40(3)	1.41(8)	-	11(1)
	2.30(9)	0.42(0)	-0.26(9)	26.4(5)	20(2)
	1.05(4)	0.59(1)	-0.04(2)	45.1(7)	46(0)
	0.70(0)	0.36(1)	-0.02(1)	49.1(6)	23(1)
210 K	3.57(0)	0.45(f)	0.41(9)	19.9(7)	19(2)
	0.92(3)	0.62(1)	-0.02(1)	46.9(9)	51(1)
	0.54(3)	0.42(1)	-0.05(1)	50.5(0)	30(0)
175 K	4.79(9)	0.46(0)	-0.10(0)	18.9(9)	16(3)
	0.97(4)	0.58(1)	-0.01(1)	47.2(1)	52(0)
	0.60(3)	0.45(1)	-0.04(1)	51.3(1)	32(0)
150 K	1.16(4)	0.63(1)	0.04(3)	45.5(0)	38(0)
	0.60(5)	0.62(1)	-0.10(2)	48.6(1)	23(1)
	0.62(2)	0.43(0)	0.02(1)	51.0(1)	39(0)
120 K	1.07(6)	0.68(2)	-0.11(4)	46.8(2)	33(0)
	0.66(8)	0.62(1)	-0.08(3)	49.6(1)	26(2)
	0.56(2)	0.46(1)	0.00(1)	51.9(1)	41(1)
110 K	1.00(0)	0.70(2)	0.05(3)	46.8(1)	36(1)
	0.72(0)	0.50(0)	-0.01(2)	49.9(2)	31(2)
	0.63(4)	0.47(1)	-0.03(1)	52.0(1)	33(1)
100 K	1.11(7)	0.72(0)	-0.01(1)	47.0(2)	35(0)
	0.77(6)	0.50(0)	-0.01(2)	50.1(2)	33(1)
	0.63(0)	0.48(1)	-0.04(2)	51.9(1)	32(2)
89 K	1.19(7)	0.75(3)	-0.06(3)	47.4(2)	28(0)
	0.75(0)	0.49(1)	-0.01(2)	50.7(1)	30(2)
	0.57(0)	0.50(1)	-0.06(1)	52.9(0)	42(1)

Mössbauer spectra obtained at different temperatures varying from 300 – 80 K are shown in Figure 4.10. Mössbauer spectrum corresponding to stoichiometric magnetite could be deconvoluted in to two sextets corresponding to the occupation of iron at octahedral and tetrahedral sites in the ratio 2:1 (Cf. Figure 2.13). Mössbauer spectrum as obtained at 300 K shows that close to 70 % of Fe atoms are associated with nearly crystallite magnetite particles of size close to 15 nm and the remaining are associated with particles of size less than or close to 10 nm. Other two fractions are composed of non-interacting (SPM) and interacting magnetite nanoparticles of size less than 10nm. Mössbauer spectrum corresponding to 210 K shows that there is an increase in the fractions associated with octahedral and tetrahedral sites commensurately maintaining the ratio of 2:1 while only close to 20 % of Fe atoms are exposed to disordered surface spins. From the above spectra it is clear that these features are present for measurement temperature up to 150 K. The spectrum obtained at 120 K shows that there is an increase in the fraction experiencing higher hyperfine field as indicated by an increase in the magnitude of splitting. The value of the maximum splitting progressively increases with decreasing temperature as in the figure representing Mössbauer spectra.

The evolution of hyperfine parameters of all the fractions of Fe atoms would contribute for the overall variation in magnetic, electronic and structural property of the bulk such as Verwey transition. Hence the variation in the mean values of isomer shift associated with these fractions would be considered in the following discussion. Mean value of hyperfine field exhibits a steady increase with decreasing temperature which is typical of any ferromagnetic material.

Main results of this measurement in terms of the variation of mean value of isomer shift are plotted in the following Figure 4.11 Mean value of isomer shift exhibits an increase with decreasing temperature. Below 150 K the value of the mean isomer shift remains constant. Due to hopping of electrons from Fe^{2+} to Fe^{3+} in octahedral sites at room temperature the isomer shift of Fe occupying B sites remains close to 0.6 mm/s corresponding to a net valence of $Fe^{2.5}$. Isomer shift at A sites occupied by Fe^{3+} remains close to 0.3 mm/s. At room temperature mean value of isomer shift corresponding to a stoichiometric magnetite should be close to 0.5 mm/s. Any increase in the mean value of isomer shift could be understood only due to a reduction in the hopping of electrons. This causes a further reduction in the mean valence of Fe at octahedral sites slightly below +2.5. This is commensurate with an increase in resistivity as has been reported in the nano magnetite, although a significantly sharp increase in resistivity has been reported in the bulk.

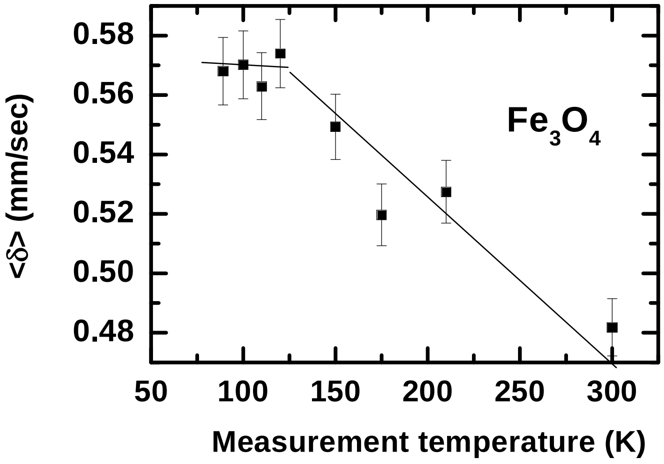

Figure 4.11: Showing the variation of mean isomer shift with measurement temperature. A steady increase in <δ> with decreasing temperature from 300 K up to 150 K is observed. A step like behavior is seen in the variation of <δ> below 125 K.

Interestingly there is a change of trend in the variation of the mean value of isomer shift below 150 K which remains almost constant. This could be understood to point out a much lesser or nil mobility of electrons from Fe^{2+} to Fe^{3+} below 125 K.

4.9 Conclusion

Summarizing the evolution of local structure and magnetic properties at Fe sites associated with bare and oleic acid capped nano particles of iron oxyhydroxide and magnetite has been studied in a detailed manner based on hyperfine parameters as deduced using Mössbauer spectroscopy. Mutually opposite variation of the mean values of quadrupole splitting and hyperfine fields with respect to of mean isomer shift have been deduced in this study which exhibit the maximum value of hyperfine field at the mean isomer shift around 0.46 mm/sec corresponding to the occurrence of maximum concentration of Fe_3O_4 in the sample. Interestingly the above variation manifests as an inverse linear correlation between the mean values of magnetic hyperfine fields and quadrupole splitting. Physics of stronger binding and hence higher temperature of dissociation of oleic acid bound to Fe_3O_4 nano particles than that of OA bound to α-FeOOH has been elucidated in the present study. The results of the present study on Oleic acid capped nano particles of magnetite and hydroxides might be useful for obtaining core-shell structures of different phases of magnetite with desired magnetic properties by controlled annealing treatments.

4.10 References:

[1] A. K. Gupta and M. Gupta, *Biomaterials*, **26**, 3995 (2005)

[2] S. Laurent, D. Forge, M. Port, A. Roch, C. Robic, L. V. Elst and R. N. Muller, *Chem. Rev.*,**108**, 2064 (2008)

[3] P. Tartaj, M. d. P. Morales, S. V.-Verdaguer, T. G.-Carreno and C. J. Serna, *J. Phys. D: Appl. Phys*., **36**, R182, (2003)

[4] A. K. Gupta and M. Gupta, *Biomaterials*, **26**, 3995 (2005)

[5] An-Hui Lu, E. L. Salabas, and Ferdi Schmith, *Angew. Chem*. **46**, 1222 (2007)

[6] A. Warland, C. Antoniak, M. Darbandi, C. Weis, J. Landers, W. Keune, and H. Wende, *Phys. Rev. B*, **85**, 235113 (2012)

[7] G. C. Papaefthymiou, E. Delin, A. Simopoulos, D. K. Yi, S. N. Riduan, S. S. Lee and J. Y. Ying, *Phys. Rev. B*, **80**, 024406 (2009)

[8] H. Duan, M. Kuang, X. Wang, Y. A. Wang, H. Mao, and S. Nie, *J. Phys. Chem. C*, **112**, 8127 (2008)

[9] M. Gotic and S. Music, *J. Molecular structure*, **834**, 445 (2007)

[10] T. Iwasaki, N. Sato, K. Kosaka, S. Waano et al., *J. Alloys & Compds*., **509**, L34 (2001)

[11] D. E. Madsen, L. C. Gontard, T. Kasama, R. E. D. Borkowski, C. B. Koch et al., *J. Phys.: Condens. Matter*, **21**, 016007 (2009)

[12] H. Naono and R. Fujiwara, *J. Colloid Interface Sci.*, **73**, 406 (1980)

[13] L. Diamandescu, D. M. Tãrãbãşanu, and S. Calogero, *Mater. Chem. Phys*., **48**, 170 (1997)

[14] D. Walter, G. Buxbaum, and W. Laqua, *J. Therm. Anal. Calorim*, **63**, 733 (2001)

[15] H. Fan, B. Song, and Q. Li, Mater. *Chem. Phys*., **98**, 148 (2006)

[16] W. J. Zhang, C. F. Huo, G. Feng, Y. W. Li et al., *J. of Molecular structure; Theochem,* **950**, 20 (2010)

[17] T. K. McNab, R. A. Fox, and A. J. F. Boyle, *J. Appl. Phys.*, **39**, 5703 (1968)

[18] L. Zhang, R. He, H.-C. Gu, *Appl. Surf. Sci*., **253**, 2611 (2006)

[19] Herojit singh, L.; Govindaraj, et. al.. (to be published)

CHAPTER 5

MAGNETIC INTERACTIONS BETWEEN MAGNETITE NANOPARTICLES FORMED IN ZEOLITE

Chapter 5

Magnetic interactions between magnetite nanoparticles formed in zeolite

5.1 Introduction

Several synthesis methods including hot injection, sonochemistry and thermal decomposition of organometallic compounds have been employed for the fabrication of various metal and metal oxides nanoparticles [1-3]. These methods often result in particles with large size (≈ 50 nm and above) with a wide distribution and irregular shape [4]. Such magnetic nanoparticles exhibit low magnetic moments. An effective way to finely control the particle size and shape is to encapsulate magnetic particles inside a porous inorganic template matrix [4] with defined pore size and shape. The size and the magnetic properties of the nanoparticles can easily be controlled by simply tuning the pore size of the nanoporous silica matrix. The loading of a metal source in nanoporous matrix also plays a critical role in controlling the particle size in the confined nanoporous matrix and significantly affects the magnetic properties of the particle [4].

Apart from the above mentioned advantages of templated nanoparticles, one can very well tune the particle – particle distances. By tuning the mean interparticle distance the physics of the magnetic interactions between the particles can be understood in a greater detail. Unlike to that of the surfactant coated nanoparticles as discussed in Chapter 4 where the particle starts agglomerating since the surfactant providing the stability dissociates above 600 K. To maintain the stability of the nanoparticles, (i.e.) to prevent coarsening of the nanoparticles it is required to bind these particles strongly in a suitable template. This study has been motivated at exploring the possible binding of magnetite nano particles by Zeolite which is also a suitable template with respect to biocompatibility. It has been reported that Zeolites could bind cations strongly [5]. Zeolite 13X is chosen as a template for the present study which belongs to a group of crystalline alumino silicate with the basic tetrahedral structural units of SiO_4 and AlO_4 with Si or Al in the center of the tetrahedron Cf. Figure 5.1.

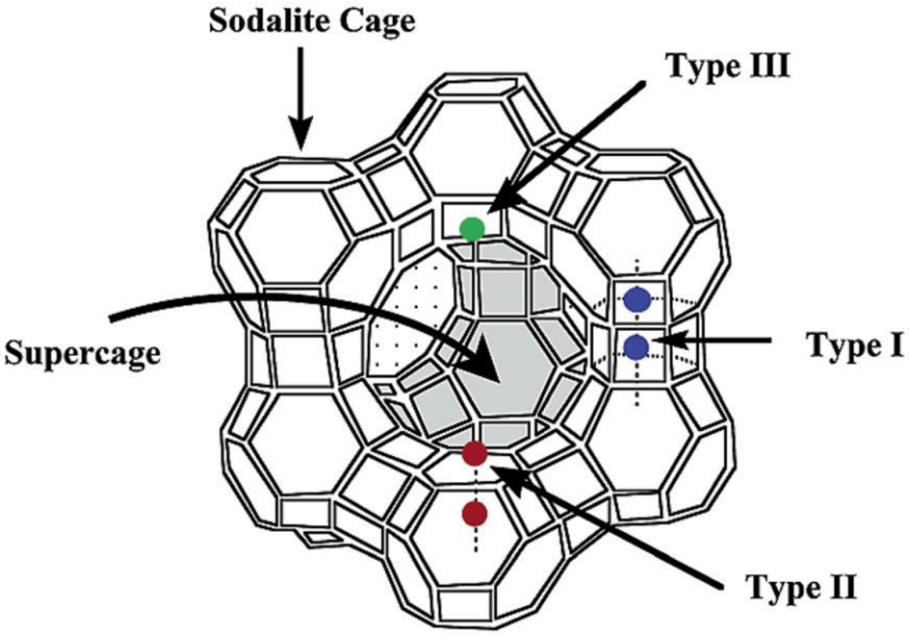

Figure 5.1: Drawing of the framework structure of Zeolite X is shown. Non-equivalent oxygen atoms numbered 1-4 lie at the centre of each line segments while Si and Al atoms are alternatively present at tetrahedral intersections. Positions of cations other than Si, Al presents in the frame work structures are shown in terms of Roman symbols I-III.

These groups are joined to form a larger unit called sodalite unit (SU) with [Si]/[Al] ratio close to 1.23, and the cavity inside SU is known as β cage. SU arrangement forms α cage with the entrance windows having a diameter close to 8 A while the maximum diameter of the empty α cage is around 13 A. In the aluminosilicate structure each tetrahedral group of AlO_4 has an uncompensated charge of -1 and hence remains attractive to positive ions such as Na^+, Ca^+ resulting in their occupation at sites nearby AlO_4 groups. This property of Zeolite has been extensively used for binding heavy cations in pores and cages. In addition binding of nano particles of different metals and insulting oxides by zeolites have been carried out in the literature [5-10]. In spite of a number of works being reported on magnetite nano particles dispersed in zeolite [7,11,12], issues related to detailed understanding of structural and magnetic properties of nano particles of magnetite and the binding of these particles by zeolite are yet to emerge.

This work is motivated at studying the binding of magnetite nanoparticles by zeolites. This is addressed by means of studying the local structure and magnetic properties of these nanoparticles of size less than 10 nm as formed in zeolite by means of Mössbauer spectroscopy. This is done by exploiting the power of Mössbauer spectroscopy to distinguish between isolated superparamagnetic particles of magnetite as bound in templates and after coarsening subsequent to detrapping and migration from the bound sites in templated structures due to thermal treatment. These results are compared with that of bare Fe_3O_4 in order to clearly elucidate the role of binding by Zeolite.

5.2 Thermal stability of bare and zeolite templated Magnetite nanoparticles

The fine crushed 5 gm of fine powder Zeolite using agate mortar was heated at 200 ^oC for 1 h then rise the temperature at 250 ^oC for 2 h. The dried Zeolite is immersed in the Fe precursor's solution where $[Fe^{+2}] : [Fe^{+3}] \approx 1:2$ then ultrasonicated for 1 h. NaOH solution was added rapidly to raise the PH upto 10. As soon as NaOH solution was added the solution turns into brownish colour. The solution was stirred using a glass rod just to mix it properly. After stirring for an hour the precipitate is separated by sedimentation process. The precipitate was washed with ultra high pure water until it achieve PH 7 and then by acetone. It was dried at 100 ^{o}C for 10 h. the synthesis was carried out with two different concentration of Fe precursor’s solution.

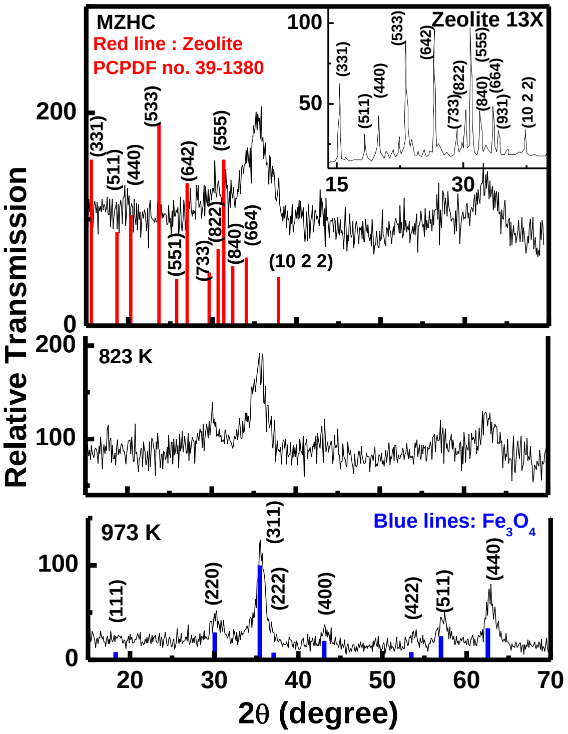

Figure 5.2: XRD spectra of magnetite nano particles as grown in zeolite and subsequent to different annealing treatments as mentioned.

XRD spectrum corresponding to magnetite nano particles prepared in Zeolite as shown in Figure 5.2 show the peaks corresponding to Fe_3O_4 while the mean size of the particles is deduced to be around 4 nm. M-H loop measurement at 80 K in magnetite dispersed zeolite (Cf. Figure 5.3) exhibits a hysteresis loop with a low value of coercivity and retentivity typical of a superparamagnetic particle of off-stoichiometric magnetite [13]. This indicates the ferrimagnetic nature of the magnetite nanoparticles dispersed zeolite.

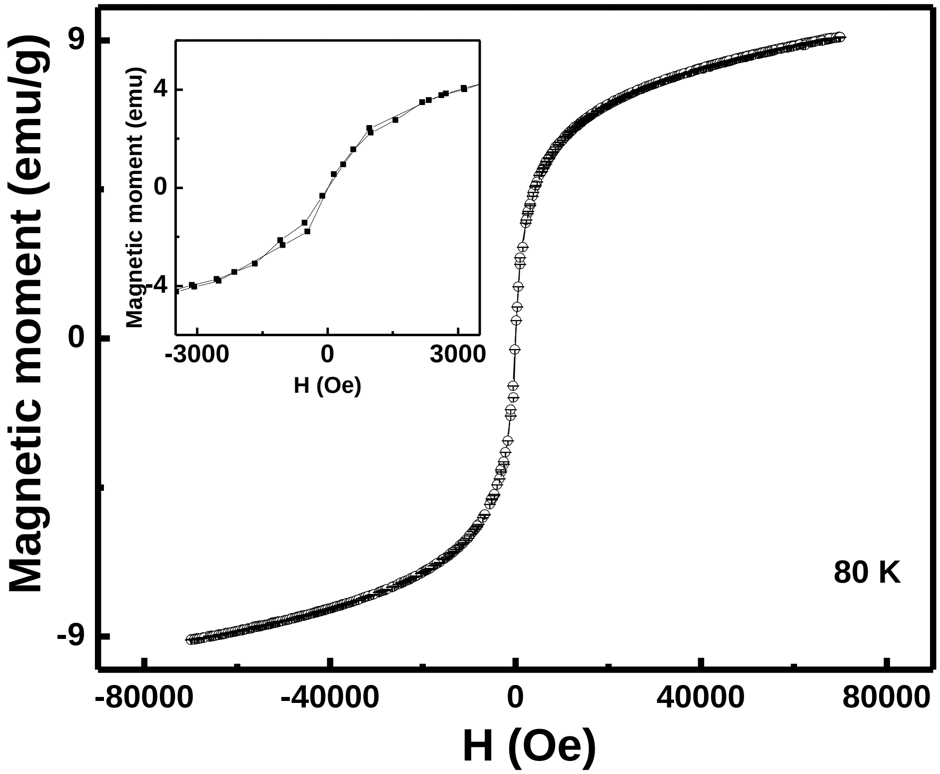

Figure 5.3: M-H loop as obtained at 80 K in magnetite nanoparticles dispersed zeolite. The weight corresponds to that of both Fe_3O_4 and zeolite.

Annealing treatment at 823 K results only in a slight narrowing of FWHM of the maximum intense peak in XRD spectrum implying an increase in the mean size of particles by only about 1.5 nm. The mean size of the particles has been deduced to be around 8 nm subsequent to annealing at 973 K. Thus the XRD results imply that the particles coarsen for annealing treatments beyond 950 K.

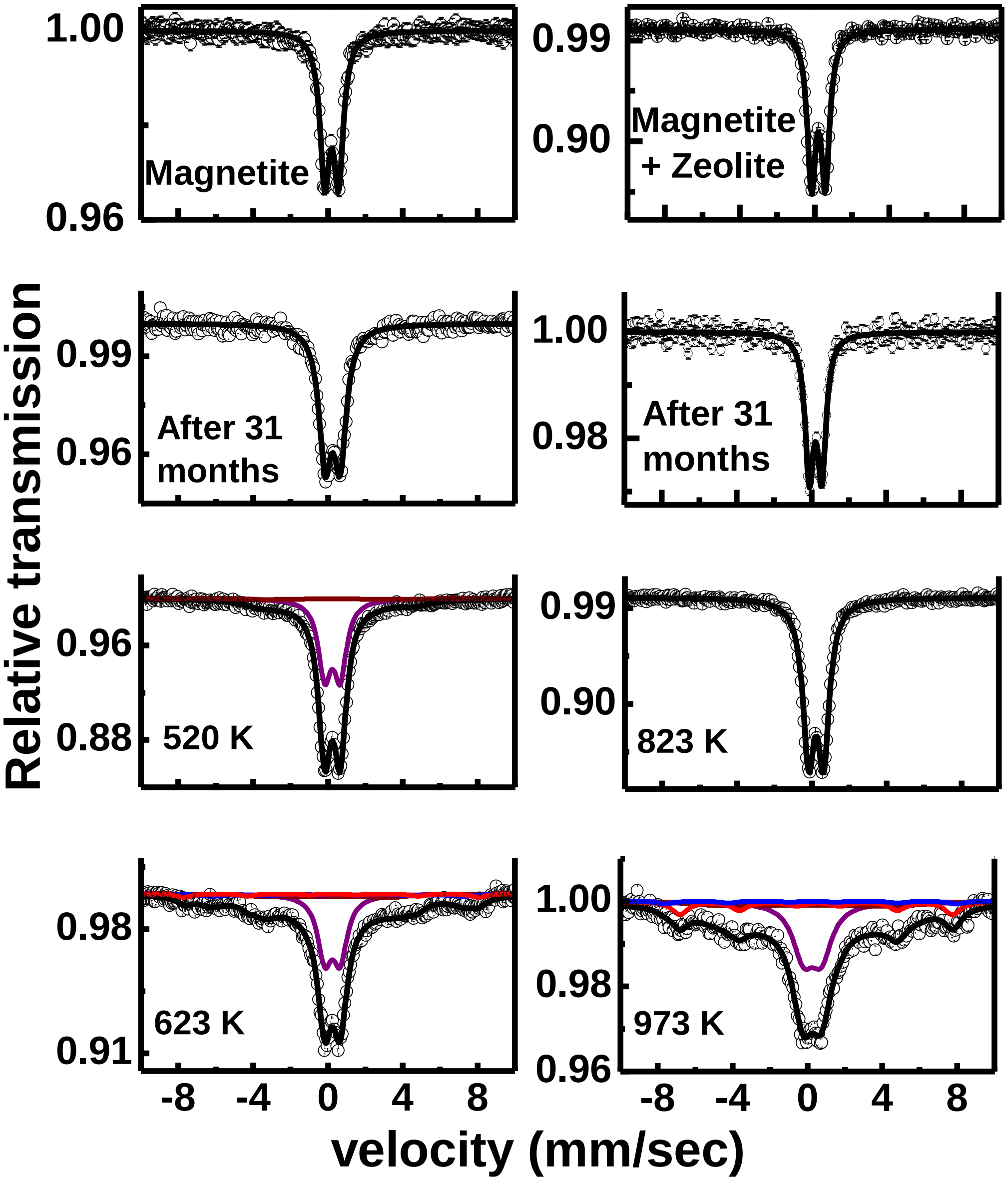

Figure 5.4: Mössbauer spectra obtained at 300 K in the bare and zeolite dispersed super paramagnetic particles of magnetite in the as prepared condition and subsequent to annealing at different temperatures are shown in left and right panels respectively in the figure.

Table 5-1: Mössbauer results on the sample containing bare and zeolite dispersed magnetite nanoparticles prepared using co-precipitation method subjected to annealing treatments as explained in this work.

Sample treatment	i	Γ_i (mm/s)	δ_i (mm/s)	Δ_i (mm/s)	B^i_{hf}	f_i (%)
Bare magnetite nanoparticle	1	0.67(5)	0.34(2)	0.73(4)	-	100(2)
After 31 months	1	0.82(7)	0.37(3)	0.82(3)	-	100(2)
T_a = 520 K	1	0.81(4)	0.37(4)	0.83(5)	-	70(1)
	2	2.2(4)	0.37(6)	0.44(9)	25.5(0)	30(2)
T_a = 623 K	1	0.91(7)	0.40(8)	0.82(2)	-	53(0)
	2	2.2(3)	0.48(9)	0.28(3)	22.0(0)	29(3)
	3	1.9(1)	0.47(3)	0.12(4)	41.8(1)	10(1)
	4	1.0(1)	0.42(4)	0.08(3)	48.8(1)	08(1)
Magnetite nanoparticles as prepared in Zeolite	1	0.58(5)	0.34(2)	0.73(4)	-	100(0)
T_a = 823 K	1	0.62(5)	0.37(5)	0.80(8)	-	100(1)
T_a = 973 K	1	1.3(2)	0.44(7)	0.96(9)	-	42(1)
	2	3.80(4)	0.5(1)	0.16(3)	25.7(1.1)	33(2)
	3	2.10(6)	0.66(9)	0.12(3)	41.2(1)	15(1)
	4	1.30(4)	0.44(9)	0.10(5)	47.0(2.0)	10(1)

f_1, f_2 are fractions of Fe atoms associated with super paramagnetic and disordered surface spins of nano particles respectively. Fractions f_3 and f_4 represent Fe atoms occupying octahedral and tetrahedral interstitial sites of off-stoichiometric magnetite.

Mössbauer spectrum corresponding to bare nanoparticles of magnetite shows the occurrence of a broad sextet in addition to a predominant doublet subsequent to annealing treatment at 523 K indicating that around this temperature the onset of migration of bare nano particles could be taking place (Cf. Figure 5.4 (left column)). Annealing at 623 K clearly shows the occurrence of a broad sextet along with a much lower relative fraction of Fe atoms (29 %) associated with super paramagnetic nano particles. This implies that as large as 71 % of Fe atoms are associated with sextets corresponding to coarsened magnetite particles. Mössbauer measurements on bare nano particles close to 31 months after preparation show that there is an increase in the values of line width and isomer shifts by roughly about 0.15 mm/sec as compared to that of the as prepared oxide nano particles. This implies the important role that might be played by water molecules in stabilizing the bare nano particles [14]. Bare nano particles kept at 300 K for a long time close to 31 months results in dehydration of water molecules at a slow rate resulting in an almost similar effect equivalent to annealing at 523 K in the as prepared sample.

Mössbauer spectra acquired in the as prepared condition and after a period of 31 months and hence the deduced quadrupole parameters remain the same in the case of magnetite nanoparticles as prepared in zeolite. This establishes the stability of the nano particles of magnetite as prepared in zeolite. Mössbauer spectra acquired subsequent to annealing at different temperature up to 823 K remain as doublet representative of the entire fraction (100 %) of Fe atoms associated with super paramagnetic nano particles. Importantly slight increases in the values of line width (Γ and Δ) of the doublet are seen subsequent to annealing at 820 K. It is seen that the variation in the size of magnetite particles match with that of the line width corresponding to super paramagnetic particles of magnetite. It is seen from Figure 5.2 that there is a slight increase in the size of magnetite particles subsequent to annealing at 823 K and the variation of size is seen to match quite well with that of the variation in Γ corresponding to that of super paramagnetic particles as deduced using Mössbauer spectroscopy. The slight increase in Γ and Δ point to an important interpretation that the super paramagnetic particles of magnetite are of unique structural configuration in the as formed condition and with slight coarsening there is an onset of uniqueness associated with structural distortions. This further implies the important role played by zeolite template in the formation of super paramagnetic particles of magnetite in the as prepared condition of the

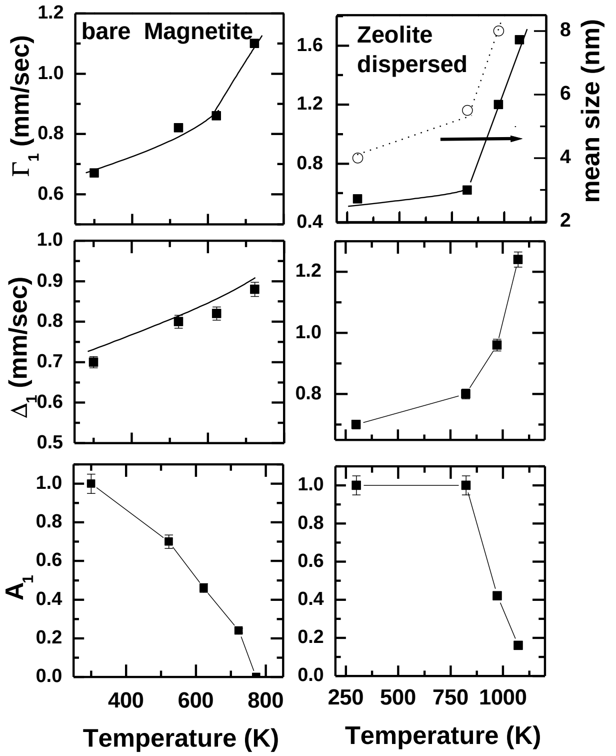

Figure. 5.5: Variations of hyperfine parameters viz., Γ_1, Δ_1 and relative fraction f_1 of iron atoms associated super paramagnetic particles which are bare and zeolite dispersed with annealing temperature are shown in left and right panels respectively. Monotonous changes are seen in the case of bare nano particles while the hyperfine parameters as experienced by 57Fe atoms associated with super paramagnetic particles of magnetite as dispersed in zeolite remain constant for annealing treatments up to 820 K and exhibit sharp change beyond 850 K implying the onset temperature of detrapping of magnetite nano particles.

same [7,15]. Annealing at 870 K is seen to result in a sharp reduction of the fraction of Fe atoms associated with super paramagnetic particles of magnetite. Concomitantly a sharp increase in the mean size of the particles as deduced using XRD is seen for annealing treatments beyond 920 K.

Variation of quadrupole parameters such as line width, quadrupole splitting and the relative fraction of Fe atoms associated with SPM particles corresponding to bare and zeolite dispersed magnetite particles with annealing temperature is shown in Figure 5.5. In the case of bare nano particles it is seen that there is a steady increase in line width and quadrupole splitting in association with a decrease in the corresponding fraction for annealing treatments above 400 K. Occurrence of a damped sextet in a Mössbauer spectrum implies the onset of coarsening of the nano particles. This must be preceded by two processes viz., detrapping of bound nano particles and migration of less bound nano particle to a more strongly bound nano particle which are closely separated.

Hence coarsening of nano particles is dependent upon two parameters viz., onset temperature of migration which in turn is dictated by the binding of particles and the density of nano particles. Annealing at 520 K results in a decrease in the super paramagnetic fraction by 35% with the appearance of a sextet associated with 35 % of Fe atoms. This result could be understood due to dehydration of water molecules. Consistently similar results obtained in the sample containing bare magnetite nano particles subsequent to 31 months after preparation imply that the water molecules might be playing an important role of stabilizing the magnetite nano particles.

In the case of zeolite dispersed magnetite particles the value of the fraction of Fe atoms associated with super paramagnetic doublet remains stable at 100% for annealing treatment up to 820 K while there is a slight increase in the values of line width (Γ_1) and quadrupole splitting (Δ_1) corresponding to super paramagnetic doublet subsequent to annealing at 820 K. The variation of Γ_1 is observed to be consistent with that of the mean size of the particles as deduced using XRD exhibiting a slight increase in the mean size of the particles around 820 K. Nano particles comprising of ferro/ferri magnetic materials with domain size close to 10 nm can have moments larger than 10^4 μ_B. Hence dipole-dipole interaction between these magnetic nano particles would be predominant. As the dipole-dipole interaction varies as μ^2/r^3, the spins of particles which are closely spaced would be polarized experiencing a strong dipole-dipole interaction resulting in a suppression of super paramagnetic relaxation under the application of a moderate magnetic field. Assuming that the nano particles are mono dispersed it is possible to independently estimate the relative fraction of nano particles which are closely spaced based on above discussion. Application of external magnetic field of 0.3 T (Cf. Figure 5.6) results in a decrease in the fraction associated with superparamagnetic doublet resulting in an appearance of a sextet with the association of as much as 35 % of Fe atoms experiencing a hyperfine field close to 10 Tesla. This result shows that close to 35 % of nano particles are spaced closely so that they could experience a strong dipole-dipole interaction between the spins which are polarized by external field. Annealing at 875 K results in appearance of damped sextet with almost ≈ 40 % of Fe atoms experiencing a mean hyperfine field close to 28 Tesla. As the magnitude of the fractions of Fe atoms match in the above cases we interpret that the magnetite nano particles are bound in zeolite matrix with a binding energy close to 870 K. This interpretation is consistent with the observation of a sharp increase in both Γ_1, Δ_1 beyond 870 K. This also point to the observation that the magnetite nano particles are selectively bound to a unique trap in zeolite. This might indicate that the magnetite particles could be bound to zeolite by a binding energy ≈ 2.5 eV.

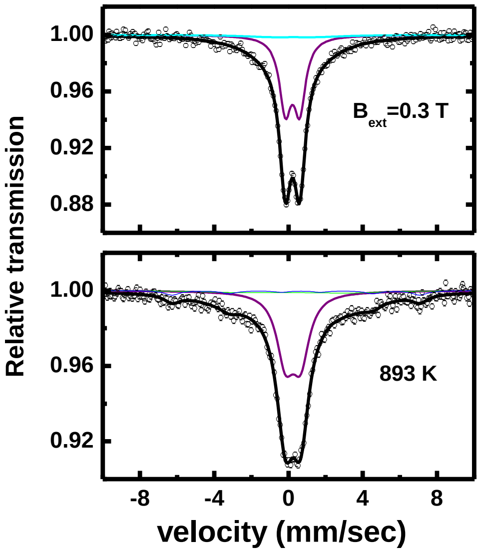

Figure 5.6: Mössbauer spectra corresponding to magnetite nanoparticles formed in Zeolite (a) with the application of magnetic field parallel to γ ray direction on the as prepared sample and (b) subsequent to annealing treatment at 893 K

This value is almost close to the binding energy of Au cluster on to the surface of silica with defects as experimentally deduced by G. M. Veith et. al. to be around 2.8-3.5 eV [16]. Such a strong binding of Au cluster was comprehended due to negative surface of silica caused by H^+ vacancy at the surface, with positive charge of Au cation. Similarly the present result could be understood due to a strong electro static attraction between negative surface charge of silica due to removal of H^+ from the surface and positive surface charge of Fe_3O_4 due to the occurrence of oxygen vacancy at the surface. Other plausible understanding could be due to electro static attraction between Fe_3O_4 nano particles with oxygen vacancies with oxygen ions of water molecules which are in turn strongly bound to AlO_4 of zeolite templates. It has been reported that water molecules are very strongly bound to certain sites in zeolites [17]. Thus there could be a strong binding of negatively charged AlO_4 with the positively surface charged Fe_3O_4 with or without the mediation of water molecules.

The interactions of Fe_3O_4 superparamagnetic bare and templated nanoparticles and the growth kinetics as due to heat treatment were discussed. A huge improvement in the stability of the nanoparticles in terms of agglomeration or coarsening was observed in the case of zeolite templated nanoparticles as compared to bare nanoparticles. The detrapping energy of the nanoparticles with same composition from a similar template would be same as it is considered to be 890 K in the case of Fe_3O_4 templated in zeolite matrix. Considering the coarsening of the particles due to migration would vary as the density of the nanoparticles decrease.

5.3 Magnetic Interactions between nanoparticles formed in Zeolite

As the particle size decreases the anisotropy energy decreases, and for a grain size lower than a characteristic value, the thermal energy (i.e. kT, where k and T signifies Boltzmann constant and temperature) dominates over the anisotropy energy leading to the fluctuation of the total magnetic moment. The fluctuation time of magnetic moment (i.e.) Neel's relaxation time, $\tau = \tau_o \exp(KV/kT)$, where τ_o is of the order of 10^{-10}-10^{-13} s and depends weakly on temperature [18]. The blocking temperature decreases with decreasing particle size. In the Neel's relaxation of magnetic moments the interaction between nanoparticles is assumed to be negligible or not taken in to account. However in practice, magnetic interactions between the particles are very important to be considered and often significant. The magnetic interaction strength is inversely proportional to the square of the distance between the particles [19]. In this study the magnetic interactions between the magnetite nanoparticles grown in zeolite template is addressed and compared with that of bare magnetite nanoparticles using Mössbauer spectroscopy.

Under the application of an external magnetic field of 100 Oe, the variation of Magnetic moment under zero field cooled and field cooled with measurement temperature is shown in the Figure 5.7. These two curves get bifurcated around 50 K implying the Blocking temperature of the system. Between 300 – 150 K there is only an increase in magnetic moment by 0.19 emu/g while the value of (ΔM / ΔT) in the interval 150 – 100 K is significantly larger than that of 300 – 150 K. In the temperature interval of 100-50 K a much larger increase in magnetic moment (≈ 0.89 emu/g) with decreasing temperature has been observed as seen in Figure 5.7.

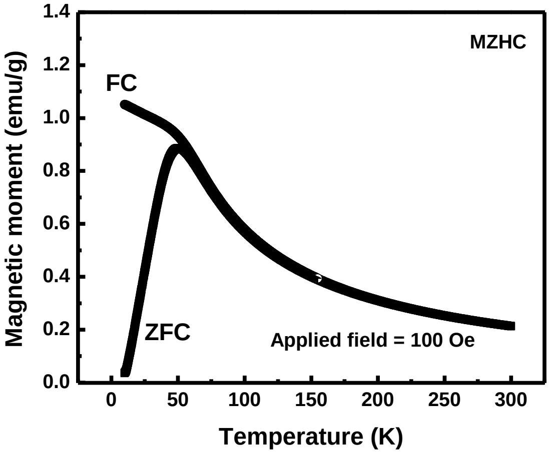

Figure 5.7: Showing the variation of magnetization in zero field cooled and field cooled conditions of the magnetite formed in zeolite

Mössbauer studies have been carried out in the temperature interval 300 – 85 K in the samples composed of bare nanoparticles of magnetite and in the magnetite nanoparticles formed in zeolite template as explained earlier. The corresponding Mössbauer spectra are shown in Figure 5.8.

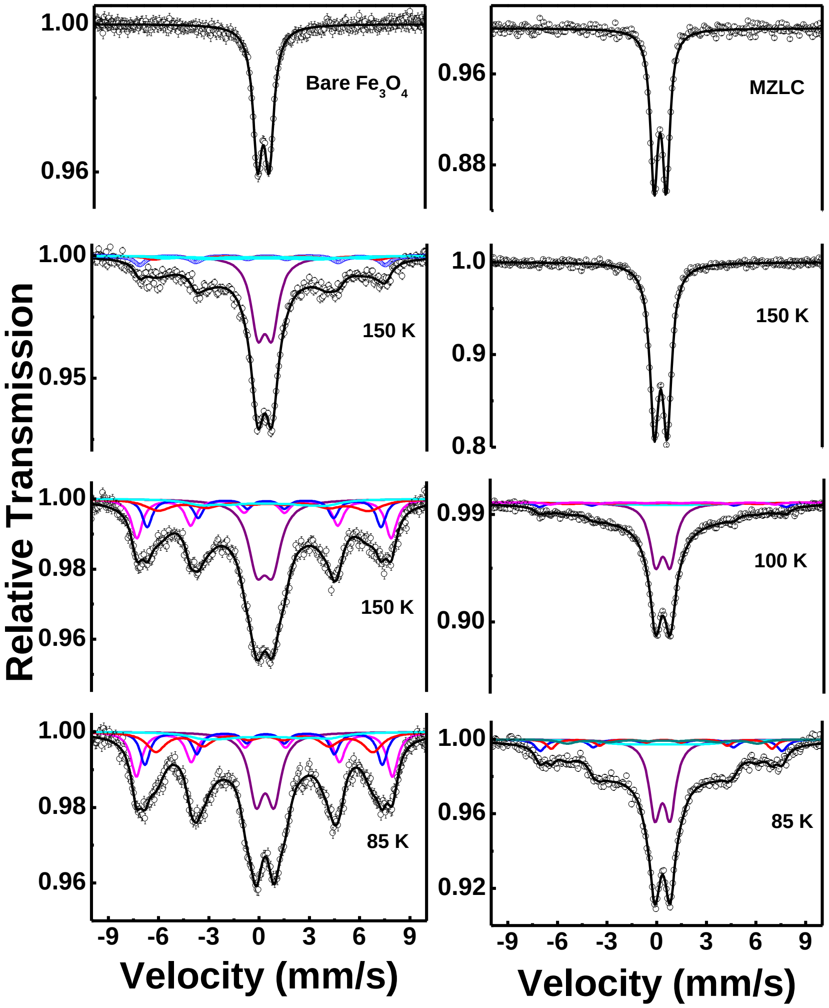

Fig 5.8 Mössbauer spectra of bare and zeolite templated magnetite nanoparticles at various low temperatures, left column spectra are for bare magnetite and the right corresponds to templated nanoparticles.

Mössbauer spectra obtained at different temperatures in the case of bare and zeolite templated magnetite nanoparticles are shown in the above figure. In the case of bare nanoparticles the Mössbauer spectrum which remains as a doublet due to superparamagnetic relaxation of spins evolves into a sextet below the temperature at which the anisotropy energy becomes comparable and greater than the thermal energy. This occurs just below 200 K onwards in the case of bare nanoparticles manifested as a broadening of the Mössbauer spectrum as compared to the spectrum obtained at 300 K (Cf. Figure 5.8). It is important to note that in the case of magnetite nanoparticles formed in zeolite template, which is of typically of same size as the previous case with the only difference being in the particle concentration, the temperature below which there is an onset of magnetic ordering occurs around 130 K. In contrast to the Mössbauer spectrum obtained at 150 K which remains as a doublet, the spectrum corresponding to 100 K exhibits large line width which is understood due to an appreciable relative fraction of Fe atoms experiencing ferromagnetic interaction (Cf. Figure 5.8 & Table 5.2). This effect is commensurate with the temperature dependent magnetic moment as shown in Figure 5.7. This large difference between the blocking temperatures as observed in these two cases clearly elucidates the predominant role of magnetic interactions between nanoparticles as dictated by the concentration and hence mean interparticle distances. This is further illustrated with the Mössbauer results obtained in magnetite nanoparticles of lower concentration i.e. with ($[Fe^{2+}] \approx 0.083$ M, $[Fe^{3+}] \approx 0.166$ M) as compared to the previous case ($[Fe^{2+}] \approx 0.5$ M, $[Fe^{3+}] \approx 1$ M) formed in zeolite template as shown below. In both these cases the size of the magnetite nanoparticles are same and close to 5 nm. In this case Mössbauer spectrum obtained at 87 K remains as a superparamagnetic doublet clearly illustrating the effect of dipolar interactions between particles which is dependent inversely upon the cube of the distance between the particles. With the lower concentration and hence a larger distance of separation between different particles of magnetite nanoparticles has resulted in a much reduced dipolar interactions.

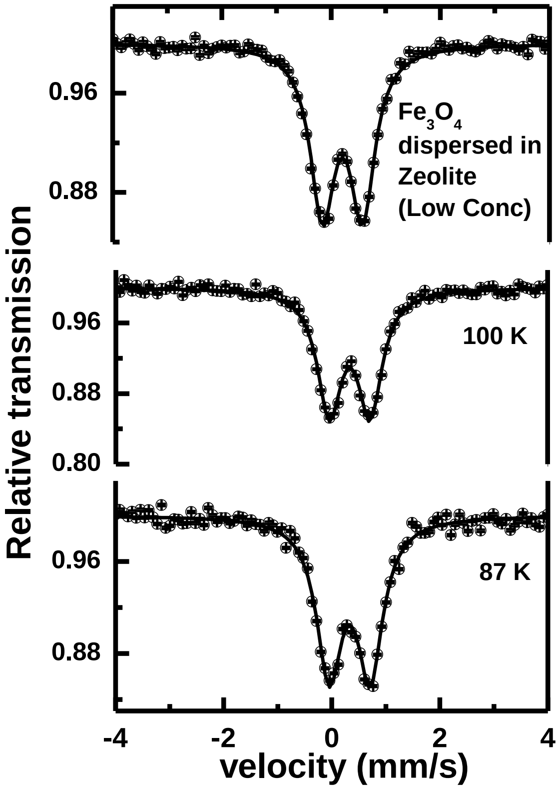

Figure 5.9: Mössbauer spectra of the magnetite dispersed in zeolite (low conc.) at RT, 100 K and 87 K.

Having illustrated the significant dependence of dipolar interactions between magnetite nanoparticles on the magnetic relaxation effects based on the Mössbauer results, in the following the variation in the hyperfine parameters corresponding to the Fe atoms associated with superparamagnetic and magnetically ordered components in the case of MZHC will be discussed.

Table 5.2: Results of Mössbauer studies carried out at different temperature on the sample containing magnetite (high concentration and low concentration) nanoparticles in zeolite prepared using co-precipitation.

Temperature (K)	**Γ_i (mm/s)**	**δ_i (mm/s)**	**Δ_i (mm/s)**	**B^i_{hf} (T)**	**f_i (%)**
MZHC (300 K)	0.56(1)	0.33(3)	0.69(2)	-	100(2)
150	0.64(0)	0.37(0)	0.78(0)	-	100(1)
130	0.72(1)	0.46(0)	0.80(0)	-	83(0)
	2.88(f)	0.46(0)	0.08(9)	20.5(1.3)	17(1)
110	0.89(1)	0.46(0)	0.81(0)	-	66(2)
	3.78(0)	0.46(9)	0.01(9)	22.0(7)	34(1)
100	0.71(14)	0.46(1)	0.82(2)	-	29(2)
	1.12(10)	0.53(6)	-0.11(9)	5.2(1.5)	20(1)
	3.95(0)	0.46(0)	0.12(9)	19.6(1.1)	35(3)
	2.08(20)	0.53(8)	0.02(9)	43.1(4)	16(1)
85	0.63(3)	0.46(1)	0.82(0)	-	18(1)
	0.88(16)	0.52(0)	-0.02(4)	5.8(3)	16(3)
	3.60(50)	0.53(5)	-0.01(9)	20.8 (7)	45(2)
	1.54(15)	0.51(0)	-0.10(0)	42.8(2)	21(1)
Fe_3O_4 in zeolite Low conc. (300 K)	0.54(1)	0.33(0)	0.73(1)	-	100(2)
100	0.53(1)	0.45(0)	0.75(5)	-	100(0)
87	0.57(1)	0.45(1)	0.76(1)	-	100(2)

With a decrease in the measurement temperature there is an enhanced dipole-dipole interaction between particles leading to an increase in the fraction of Fe atoms exposed to magnetic interactions at the cost of the fraction associated with superparamagnetic particles. In the above figure mainly the variation of hyperfine parameters pertaining to two main fractions viz., fraction of Fe atoms associated with superparamagnetic particles experiencing zero hyperfine field along with the dominant fraction which gets exposed to a hyperfine field due to an enhancement in the magnetic interaction.

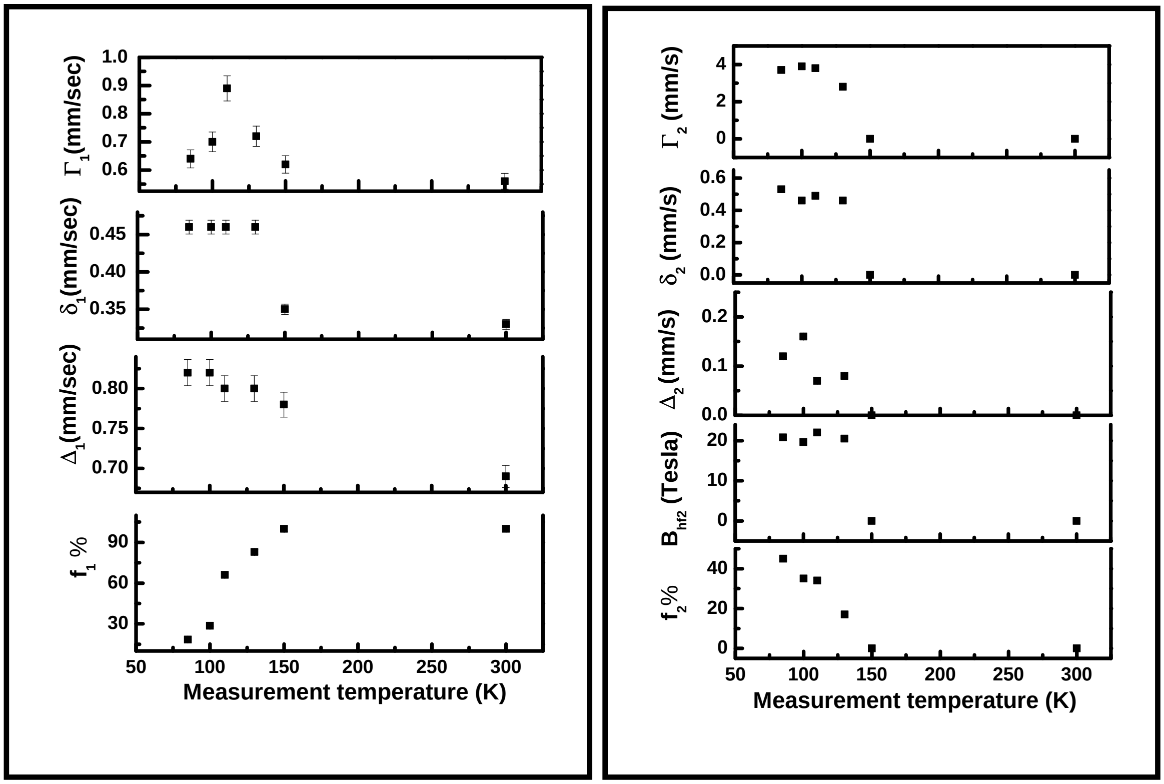

Figure 5.10: Hyperfine parameters of Fe associated with superparamagnetic doublet and the dominant fraction which gets exposed to a hyperfine field due to an enhancement in the magnetic interaction.

As the distance between particles do not vary with decreasing temperature only an enhanced magnetic interaction between nanoparticles result in a decrease in the superparamagnetic fraction f_1, as illustrated in the above figure (Figure 5.10). Concomitant with the decrease in f_1 below 150 K there has been an increase in both δ_1 and Γ_1. While δ_1 remains constant at 0.46 mm/sec below 150 K the value of Γ_1 exhibits a max around 120 K and decreases at lower temperatures. The values of δ_1 remains close to 0.35 mm/s around 150 K and increases to 0.46 close to 130 K. δ_1 remains constant in the interval 130 – 85 K. The second component which is deduced to be a sextet exhibiting low hyperfine field is observed only below 130 K having the value δ_2 close to 0.5 mm/s. This might indicate a decrease in the itinerancy of the electrons from Fe^{2+} to Fe^{3+}. A large value of Γ_2 could be understood due to varying mean distance of separation between the particles leading to a distribution in the values of hyperfine field Bhf^2. The hyperfine field Bhf2 reaches close to 20 Tesla below 150 K.

5.4 Conclusion

Magnetite nanoparticles of size of the order of 4-5 nm could be grown in zeolite template. Comparison with bare Fe_3O_4 nanoparticles almost about 400 K difference in temperatures corresponding to the onset of the occurrence of sextet due to coarsening of nanoparticles in zeolite is observed based on the controlled annealing measurements. A strong binding with a typical value close to 2.8-3 eV and hence the stability of the nanoparticles is established in the present Mössbauer study. Measurements carried out in the temperature interval 300-80 K establishes a strong dependence of magnetic dipolar interactions on the observed hyperfine parameters in particular the hyperfine fields at the sites of absorber atoms. This is further illustrated based on the comparison of Mössbauer results as obtained in zeolite dispersed with magnetite nanoparticles of same mean size but with different concentration. Evolution of hyperfine parameters due to enhanced magnetic dipolar interactions with decreasing temperature has been presented.

5.5 Reference

[1] de M. Donegá, C., Liljeroth, P. and Vanmaekelbergh, D., *Small*, **1**, 1152 (2005)

[2] A.-L. Morel, S. I. Nikitenko, K. Gionnet, A. Wattiaux, J. L.-K.-Him, C. Labrugere, B. Chevalier, G. Deleris, C. Petibois, A. Brisson and M. Simonoff, *ACS Nano*, **2**, 847 (2008)

[3] S. Sun and H. Zeng, *J. Am. Chem. Soc.*, **124**, 8204 (2002)

[4] S. Alam, C. Anand, K. Ariga, T. Mori and Ajayan Vinu, *Angew. Chem*. **121**, 7494 (2009)

[5] K. Barquist and S. C. Larsen, *Microporous Mesoporous Mater*., **130**, 197 (2010)

[6] W. Guo, D. Wang, J. Hu, Z. K. Tang, and S. Du, *Appl. Phys. Lett*., **98**,043105 (2011)

[7] F. J. Lazaro, J. L. Garcia, V. Schunemann, Ch. Butzlaff, A. Larrea, and M.A. Zaluska-Kotur, *Phys. Rev. B*, **53**, 13934 (1996)

[8] W. Chen, Z. Wang, Z. Lin, J. N. Qian, and L Lin, *Appl. Phys. Lett*., **68**,1990 (1996)

[9] T. M. Davis, T. O. Drews, H. Ramanan, C. He, J. Dong, H. Schnablegger, M. A. Katsoulakis, E. Kokkoli, A. V. Mccormick, R. L. Penn, and M. Tsapatsis, *Nature Mater*. **5**, 400 (2006)

[10] Y. Lee, B. A. Reisner, J. C. Hanson, G. A. Jones, J. B. Parise, D. R. Corbin, B. H. Toby, A. Freitag, J. Z. Larese, and V. Kahlenberg, *J. Phys. Chem. B*, **105**, 7188 (2001)

[11] J. Dong, Z. Xu and S. M. Kuznicki, *Adv. Funct. Mater*., **19**, 1268 (2009)

[12] I. W. Nah, K.-Y. Hwang, Y.-G. Shul, *Powder Technol.*, **177**, 99 (2007)

[13] G. F. Goya, *Solid State Commun.*, **130**, 783 (2004)

[14] L. Herojit singh, R. Govindaraj, R. Mythili, G. Amarendra and C. S. Sundar, *AIP Advances*, **3**, 022101 (2013)

[15] V. R. Elías, M. I. Oliva, S. E. Urreta, S. P. Silvetti, K. Sapag, A. M. M. Navarrod, S. G. Casuscellia, G. A. Eimer, *Appl. Catal., A: General*, **381**, 92 (2010)

[16] G. M. Veith, A. R. Lupini, S. Rashkeev, S. J. Pennycook, D. R. Mullins, V. Schwartz, C. A. Bridges, and N. J. Dudrey, *J. Catal.*, **262**, 92 (2009)

[17] J. E. Kim, K. Kato, M. Takata, T. Shibata, and Y. Morotomo, *Phys. Rev.B*, **79**, 132105 (2009)

[18] F. Bodker, M. F. Hansen, C. B. Koch, K. Lefmann, and S. Morup, *Phys. Rev. B*, **61**, 6826 (2000)

[19] J. Stohr, H.C. Siegmann , "*Magnetism From Fundamentals to Nanoscale Dynamics*", Springer (1983)

CHAPTER 6

POINT DEFECTS STUDIES IN NANO AND BULK FERRITES

Chapter 6

Point defects studies in nano and bulk Ferrites

6.1 Introduction

Spinel ferrites are generally represented as $(A_{1-x}B_x)_T\ \{A_xB_{2-x}\}_O\ O_4$, where suffices T and O refer to tetrahedral and octahedral sites respectively. The cation distribution is said to be normal if all the A cations having +2 oxidation state occupy tetrahedral sites while B cations with +3 oxidation state occupy octahedral sites respectively (i.e) when $x = 0$, or inverse if $x =1$. When $x = 2/3$, it results in a random distribution of cations at A and B sites and are known as random or mixed ferrites [1]. Selective substitution of cations at different sites depends upon certain factors such as electrostatic and short range contribution, ion size, crystal field effects, coordination number and ordering of cations [1].

Magnetite (Fe_3O_4) was predicted to be an inverse spinel oxide where eight numbers of Fe^{2+} ions occupy octahedral sites and 16 numbers of Fe^{3+} ions are equally distributed among octahedral and tetrahedral sites giving the ratio of Fe^{2+}:Fe^{3+} as 1 : 2. The cationic distribution in Fe_3O_4 can be modified due to the application of pressure and heat treatment [2,3]. The inverse state of Fe_3O_4 has been reported to transform to normal ferrite under the application of external pressure above 6 GPa [2,4]. The site occupancy of Fe^{2+} was also reported to be altered with respect to temperature, as Fe^{2+} favors the tetrahedral site at higher energy state [3]. As nanoparticles are characterized by high surface to volume ratio they are largely associated with point defects. Therefore, in nano spinel ferrites the cationic distribution is observed to be different from that of the bulk analogue [5-8]. Hence it is important to probe the cationic distribution in off-stoichiometric magnetite nanoparticles using Mössbauer spectroscopy in order to understand the plausible role of point defects in modifying the cationic charge distribution if any in nano magnetite.

Bulk Zinc ferrite (b-ZFO) with a normal spinel configuration having A and B sites populated only with Zn^{2+} and Fe^{3+} respectively exhibits antiferromagnetic ordering with Neel temperature 10 K [9]. In contrast the nano particles of ZFO display ferrimagnetic ordering [9] which is understood to be due to partial inversion in the population of Fe^{3+} and Zn^{2+}. Ferrimagnetic ordering has been reported in the b-ZFO synthesized using molten salt displaying high magnetization [10].

Point defects aspects in terms of antisites, cationic and anionic vacancies have been addressed in nanoparticles of magnetite and zinc ferrite in this chapter. In addition the study has been extended to the bulk $ZnFe_2O_4$ to understand the role of point defects if any to induce ferrimagnetic ordering.

6.2 Point defects in off-stoichiometric magnetite nanoparticles

XRD spectrum of the as prepared magnetite nanoparticles prepared by coprecipitation method (C.f. Figure 6.1) referred to as M3 in Chapter 3 is indexed to magnetite phase. Mean size of the magnetite nanoparticles is deduced to be around 12±2 nm. Mössbauer spectrum in the as prepared sample could be deconvoluted into four components viz., a doublet and three sextets (c.f. Figure 6.2(a) and Table 6.1). Based on the values of isomer shifts and the fractions of iron atoms associated with the sites 1 and 2 it could be understood that the as prepared magnetite nanoparticles are off stoichiometric [11]. This implies the presence of cationic vacancies at the octahedral sites associated with nano particles. The tetrahedral and octahedral sites in the nano particles of these off stoichiometric magnetite are appreciably distorted as indicated by non-zero values of quadrupole splitting.

Fe ions occupying site (3) experience hyperfine field much smaller than that of sites (1) and (2), are interpreted to be associated with surface of the nano particles experiencing disordered spins. These sites exhibit higher isomer shift which could probably be attributed to a larger concentration of Fe^{2+} at the surface of the nanoparticles. A large value of quadrupole splitting indicates that these sites are highly distorted due to cationic and anionic vacancies. 11 % of Fe ions, as indicated by site (4) are associated with superparamagnetic particles contributing for the doublet.

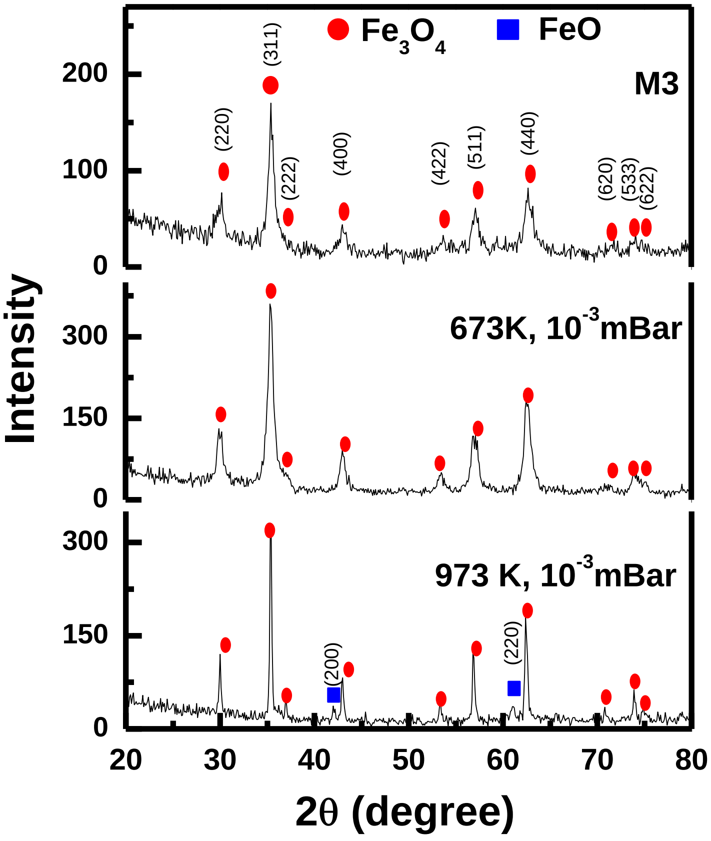

Figure 6.1. XRD spectra of of M3, heat treated at 673 K and 973 K

In this study the as prepared off stoichiometric magnetite nanoparticles are subjected to controlled annealing treatments at different temperature and at partial pressure of 10^{-3} mbar in order to understand the evolution of hyperfine parameters while the nanoparticles undergo conversion from off stoichiometric to stoichiometric magnetite.

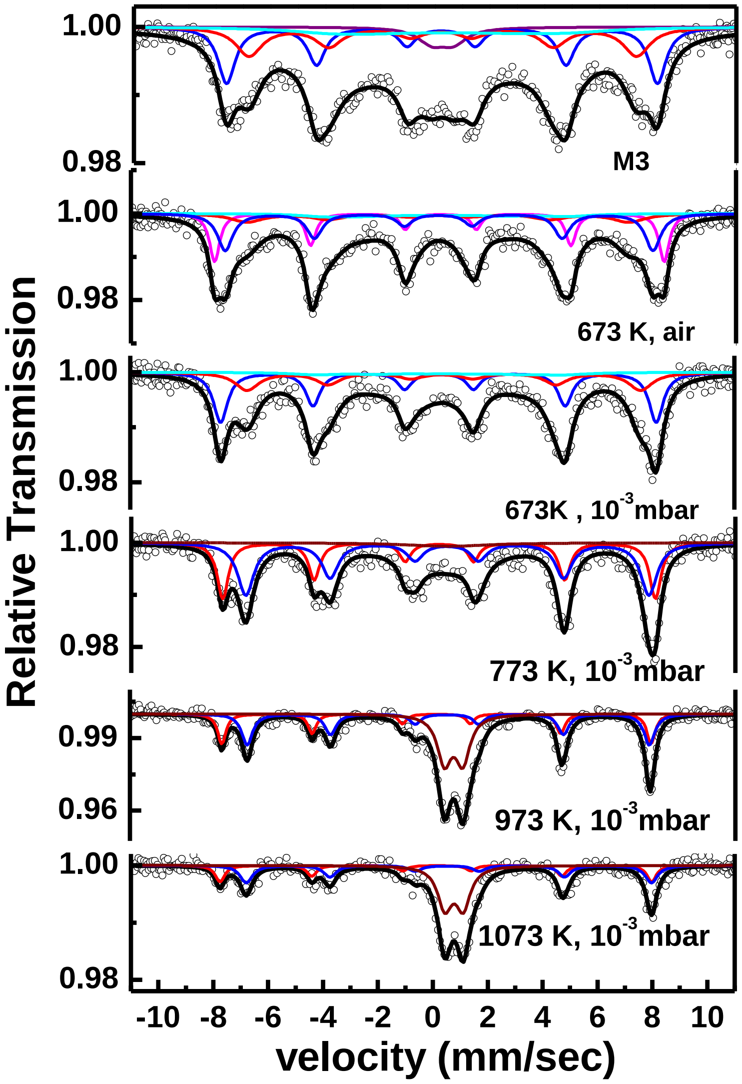

Figure 6.2. Mössbauer spectra of M3, heat treated at 673 K in air and 10^{-3} mbar respectively, 773 K, 973 K and 1073 K in 10^{-3} mbar.

Table 6.1. Fitted parameters of Mössbauer spectra with specific sites f_1, f_2 representing the fractions of Fe atoms associated with the octahedral and tetrahedral interstitial sites of Fe_3O_4, f_3 represents the disordered surface spins of nano particles, while f_4 and f_5 and f_6 represent Fe atoms experiencing superparamagnetism, γ-Fe_2O_3, FeO respectively.

Annealing Temp. (K)	**i**	**Γ_i mm/s**	**δ_i mm/s**	**Δ_i mm/s**	**B_{hf}^i T**	**f_i %**
M3	1	0.78(2)	0.36(1)	0.04(0)	48.72(4)	22(0)
	2	1.3(0)	0.38(0)	0.07(0)	43.82(3)	32(0)
	3	3.5(3)	0.47(3)	0.27(1)	27.25(6)	35(3)
	4	1.4(1)	0.38(1)	1.12(1)	0	11(1)
673, 10^{-3} mbar	1	0.62(0)	0.34(1)	0.02(0)	49.7(8)	26(1)
	2	1.2(1)	0.49(2)	0.08(1)	44.5(6)	42(0)
	3	4.2(6)	0.46(1)	0.30(6)	23(9)	32(3)
773, 10^{-3} mbar	1	0.50(5)	0.33(1)	0.00(2)	48.8(1)	27(1)
	2	0.71(4)	0.64(1)	0.02(2)	45.5(1)	52(0)
	3	0.93(f)	0.35(9)	0.09(9)	26.7(7)	09(2)
	6	1.28(9)	0.58(8)	1.50(9)	0	12(1)
973, 10^{-3} mbar	1	0.37(2)	0.26(1)	0.00(1)	48.80(1)	25(1)
	2	0.48(1)	0.66(1)	0.04(1)	45.30(1)	46(1)
	6	0.62(2)	0.88(1)	0.66(1)	0	29(1)
1073, 10^{-3} mbar	1	0.41(1)	0.24(2)	0.03(1)	48.78(6)	17(1)
	2	0.55(2)	0.67(4)	0.06(2)	45.78(9)	32(1)
	6	0.63(2)	0.89(0)	0.67(2)	0	50(1)
673, air	1	0.65(0)	0.31(0)	0.02(1)	48.2(2)	27(1)
	2	1.26(3)	0.31(3)	0.06(01	43.1(4)	26(1)
	3	2.66(5)	0.37(2)	0.36(3)	27.7(9)	24(1)
	4	2.02(4)	0.29(2)	1.02(2)	0	05(1)
	5	0.46(0)	0.36(1)	0.05(0)	50.6(4)	18(1)

XRD results show the occurrence of only the magnetite phase subsequent to annealing at 673 K while a partial reduction of Fe_3O_4 to FeO is also observed in the sample subjected to annealing treatment at 973 K (Cf. Figure 6.1). The particle size increases roughly to 14 nm subsequent to annealing at 673 K while annealing at 973 K results in a significant increase in the size of the particles to about 35 nm. The sample has been subjected to annealing at different temperatures viz., 673, 773, 973 and 1073 K and at a partial pressure of 10^{-3} mbar and subsequent to each annealing treatment Mössbauer measurement has been carried out at 300 K. Corresponding Mössbauer spectra and the hyperfine parameters as obtained based on the analysis were shown in Figure 6.2 and Table 6.1 respectively.

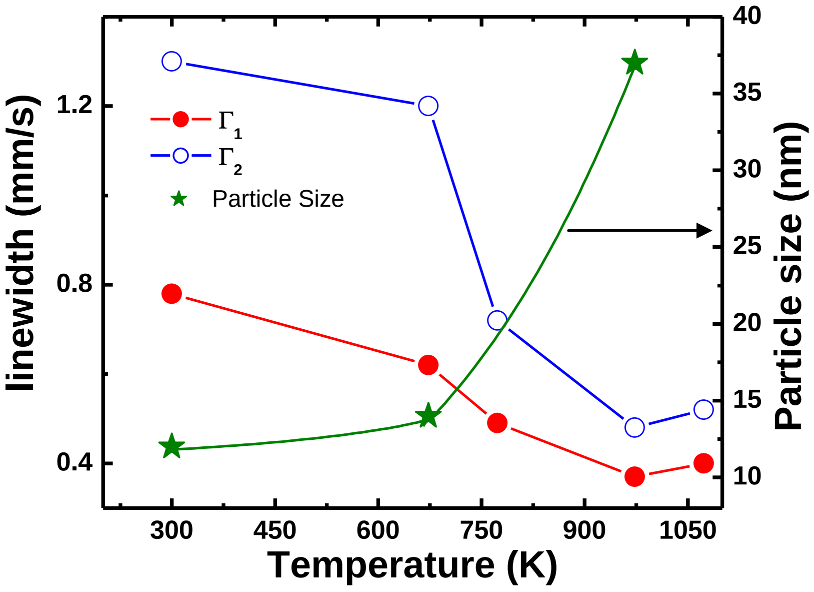

Figure 6.3. Width of the Mössbauer spectrum corresponding to Fe_{Tet} ($\Gamma 1$), Fe_{Oct} (Γ_2) and the particle size with respect to temperature.

Annealing results (Cf. Table-I) show the narrowing down of Mössbauer linewidth of deconvoluted spectra corresponding to tetrahedral and octahedra sites and the disappearance of doublet due to the coarsening of the nanoparticles. This variation is seen to correlate with an increase in particle size as deduced using XRD results shown in Figure 6.3.

The variation of hyperfine parameters corresponding to the fractions of absorber atoms occupying tetrahedral and octahedral sites viz., δ1, δ2 and the population ratio of the fractions of Fe occupying octahedral to tetrahedral sites (f_2/f_1) of the magnetite nanoparticles is shown in Figure 6.4. Other parameters such as hyperfine field and quadrupole splitting remain almost constant and hence are not presented in the figure.

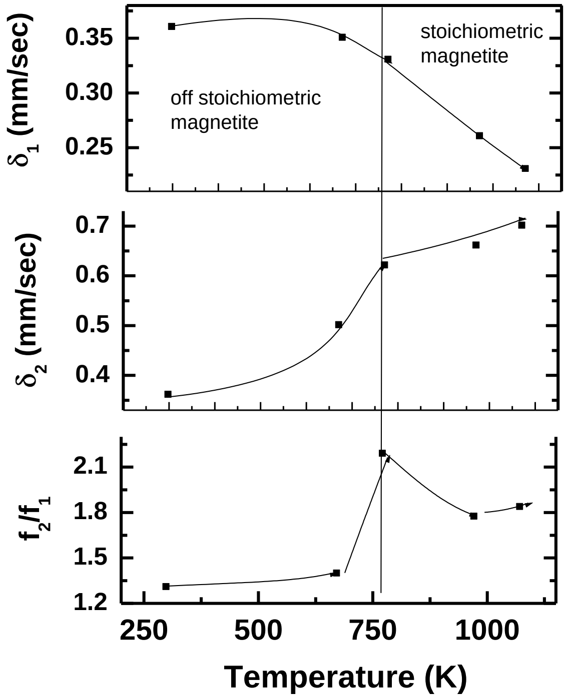

Figure 6.4. Isomer shift of Fe at tetrahedral, octahedral, ratio of area of sextets corresponding to octahedral and tetrahedral site occupation of Fe in off stoichiometric magnetite with respect to annealing temperature (top to down).

The population ratio of the fractions of Fe occupying octahedral to tetrahedral sites (f_2/f_1) remains almost constant till 700 K. Subsequent to annealing at 773 K results in the ratio of $f_2/f_1 \approx 2$, implying that the magnetite nanoparticles become stoichiometric. The mean size of the nanoparticles become close to 20 nm due to the annealing treatment as deduced from Figure 6.3. Another interesting result emerges from the variation of isomer shift. The isomer shift corresponding to Fe atoms occupying tetrahedral sites (δ_1) decreases while that of octahedral sites δ_2 exhibits an increase. An increase in δ_2 with increase in the annealing temperature could be comprehended due to an increase in the fractional population of Fe^{2+} at octahedral sites. It is important to notice that there is a decrease in the value of δ_1 concomitant to the observed increase in f_2 / f_1 and δ_2. This might indicate a finite occupation of Fe^{2+} at tetrahedral sites in nanoparticles of off-stoichiometric magnetite. Thus the present Mössbauer studies indicate the occurrence of Fe^{2+} antisite defects (i.e. occupying tetrahedral sites) in nanoparticles of off-stoichiometric magnetite. Annealing beyond 800 K results in a continuous decrease in δ_1 down to 0.28 mm/sec. A slight decrease in f_2 / f_1 beyond 870 K implies a decrease in the fraction of iron atoms occupying octahedral sites due to partial reduction of magnetite to wustite. The present result pointing to Fe^{2+} antisite defects with the partial occupation of Fe^{2+} at tetrahedral sites in nanoparticles of magnetite is consistent with the theoretical prediction of magnetite to be normal spinel ferrite based on density functional approximation [12] and also based on the experimental results reporting the similar spinel ferrites such as Mn_3O_4 and Co_3O_4 to be exhibiting normal spinel configurations [12,13]. In the following the point defects aspects in nano zinc ferrite would be reported and a comparison would be made with the bulk analogue.

6.3 Defect induced ferromagnetic ordering in Nano $ZnFe_2O_4$

It has been established in the literature that the nano zinc ferrite particles exhibit ferrimagnetic ordering due to population inversion in the site of occupation of Fe^{3+} (i.e.) the probable occupation of Fe^{3+} at A sites leading to an enhanced J_{AB} compared to J_{BB} and J_{AA}. In the case of bulk $ZnFe_2O_4$ the superexchange interactions between A – A and A-B become zero viz., $J_{AB} = J_{AA}=0$ and J_{BB} is non-zero leading to the observed anti ferromagnetic ordering with a Neel temperature close to 10 K. Bulk $ZnFe_2O_4$ either prepared through pulsed laser ablation or subjected to ball milling is also observed to exhibit magnetic ordering [14,15]. In the following these aspects will be studied in nano and bulk zinc ferrite using Mössbauer spectroscopy. The results on nano zinc ferrite would be discussed and would be compared with those obtained in bulk zinc ferrite subjected to non-equilibrium treatments.

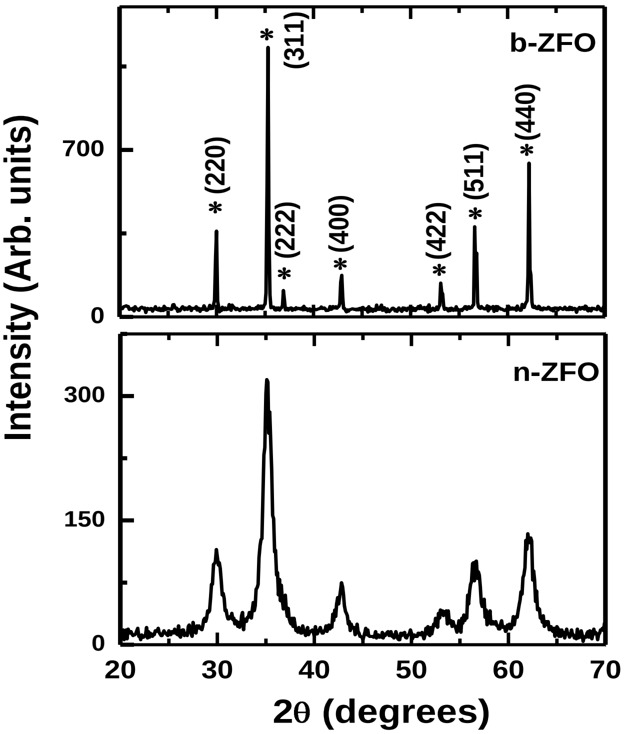

Figure 6.5: XRD spectrum of the as prepared bulk and nano $ZnFe_2O_4$.

Bulk $ZnFe_2O_4$ (b-ZFO) is synthesized through solid state reaction [16]. Pellets made of the homogeneously mixed stoichiometric ZnO and Fe_2O_3 powders were subjected to annealing at

1073 K for 8 hrs (referred to section 2.2, Figure 2.3). Subsequently the pellets were annealed at 1473 K. Nano ZFO (n-ZFO) was prepared by co-precipitation method. Solution of $ZnCl_2$ and $FeCl_3$ of the molar ratio 1 : 2 was vigorously stirred for 30 min then NaOH solution was added to obtain pH 10 and maintained (referred to section 2.2, Figure 2.2). The synthesis was carried throughout at 343 K. XRD spectra obtained in the bulk and nano ZFO (Cf. Figure 6.5) show that the peaks could be indexed with cubic (Fd3m) group. Based on the Scherrer analysis, the mean size of the bulk and nano particles of $ZnFe_2O_4$ has been deduced to be roughly equal to 49 and 7 nm respectively.

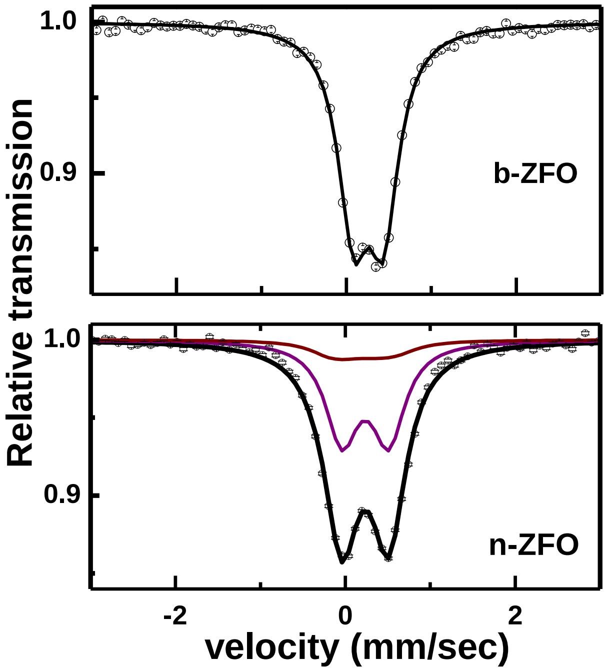

Figure 6.6: Shown are the Mössbauer spectra corresponding to bulk and nano zinc ferrite. Broadening of the spectra as seen in the nano zinc ferrite is understood due to partial inverse in the population of Fe^{3+} and Zn^{2+} sites as explained in the text.

The Mössbauer spectra as deduced in the bulk and nano ferrite are shown in Figure 6.6 for comparison. The line width of Mössbauer spectrum in the case of nano ZFO is evidently much larger than that of the bulk ZFO (Cf. Figure 6.6).

Mössbauer measurements have been carried out in nano zinc ferrite around 80 K without and with the application of a magnetic field of 0.3 Tesla in a direction parallel to that of γ-ray emission. It can be observed that the broadening effects are significantly larger with decreasing temperature and with the application of magnetic field in nano zinc ferrite. This evidently points out that the observed broadening of the spectra is due to magnetic ordering which sets in partially due to the nano size of $ZnFe_2O_4$ close to 7 nm. Hence the Mössbauer spectra corresponding to nano $ZnFe_2O_4$ were fitted with a doublet and a broad sextet in nano zinc ferrite. Mössbauer spectrum corresponding to the bulk $ZnFe_2O_4$ could be fitted with a single doublet implying the paramagnetic nature of the sample at room temperature. Mössbauer spectrum (Cf. Figure 6.6) of n-ZFO could be deconvoluted into a doublet and sextet whose parameters are shown in the table 6.2. Both of these components exhibit similar value of isomer shift typical of Fe^{3+} valence of absorber atoms. The doublet which is associated with a relative area of 78 % is characterized by a higher quadrupole splitting 0.55 mm/sec than that of the bulk analogue with a quadrupole splitting 0.39 mm/sec. A broad sextet with a relative area of 22 % is characterized by a low value of quadrupole splitting and a hyperfine field close to 3 Tesla at 300 K. Mössbauer measurement at 87 K shows that about 74 % of the relative area of the spectrum could be fitted with sextets while the remaining 26 % with a doublet. Under the application of magnetic field of 0.3 Tesla is observed to result in an increase in the splitting of the sextets leading to a larger fraction of Fe atoms experiencing much higher values of hyperfine fields compared to the results obtained at 300 and 87 K.

Occurrence of the observed magnetic ordering is understood to be due inverse population of cations viz., $(Zn^{2+})_A$ and $[Fe^{3+}]_B$. The resultant occupation of Fe^{3+} at both at A and B sites leads to an increase in the magnitude super exchange interaction J_{AB} [10] i.e. $Fe_A - O - Fe_B$.

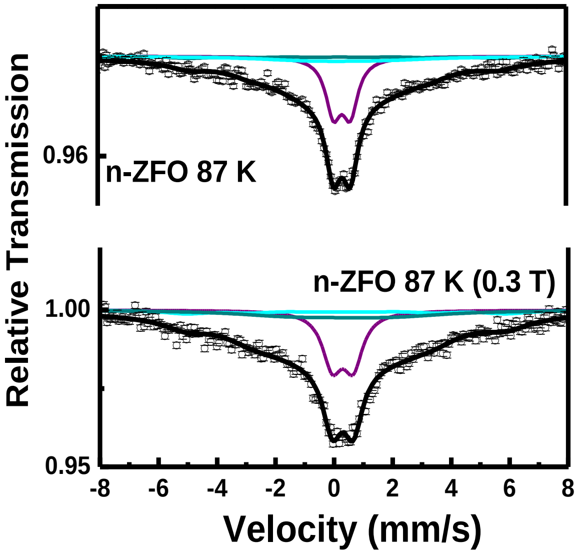

Figure 6.7. Mössbauer spectra of n-ZFO at 87 K, d n-ZFO at 87 K with an external magnetic field of 0.3 Tesla is shown

Table 6.2. Results of Mössbauer Parameter, where Γ: linewidth, δ : Isomer shift, Δ :Quadrupole splitting, Bhf : Hyperfine field.

Sample details	Γ (mm/s)	δ (mm/s)	Δ (mm/s)	B_{hf} (T)	f %
b-ZFO	0.39(1)	0.34(1)	0.39(0)	-	100(2)
n-ZFO	0.46(2)	0.35(5)	0.55(0)	-	78(1)
	0.59(4)	0.32(3)	0.05(1)	2.5(3)	22(2)
n-ZFO 87 K	0.64(0)	0.46(3)	0.71(1)	-	26(1)
	3.95(9)	0.50(0)	0.19(3)	9.9(6)	63(0)
	1.54(3)	0.46(1)	0.08(2)	33.0(9)	11(2)

An enhanced fraction of Fe atoms experiencing magnetic ordering and hence largely distributed magnetic hyperfine field at 87 K implies that there is a varying degree of partial inversion in the population of Zn^{2+} and Fe^{3+} cations. As these particles are largely of size close to 7 nm, there occurs a superparamagnetic relaxation of spins at 300 K resulting in as high as 78 % of Fe atoms exposed to purely quadrupole interaction. In the following study the possible restoration of normal ferritic configuration by means of coarsening of the nanoparticles as studied using Mössbauer spectroscopy is reported.

6.4 Recovery of normal ferritic configuration due to coarsening of $ZnFe_2O_4$ nanoparticles

Nano zinc ferrite is subjected to annealing at different temperatures in air between 673 K to 1073 K and the Mössbauer measurements have been carried out at 300 K. The fitted spectra and the parameters are presented in Figure 6.8 and Table 6.3. The results corresponding to the evolution of the two main components viz., doublet and a broadened sextet is shown in Figure 6.9. Which exhibit important and interesting changes in the hyperfine parameters. An increase in the fraction corresponding to doublet (f1) and a concomitant decrease in (f2) is seen for annealing beyond 650 K which is understood to be due to the coarsening of the particles resulting in a normal ferritic configuration and hence the decrease in f2 experiencing magnetic hyperfine interaction. This effect becomes dominant beyond 800 K and subsequent to annealing at 923 K the Mössbauer spectrum obtained at 300 K remains as a doublet with hyperfine parameters similar to that of the bulk analogue.

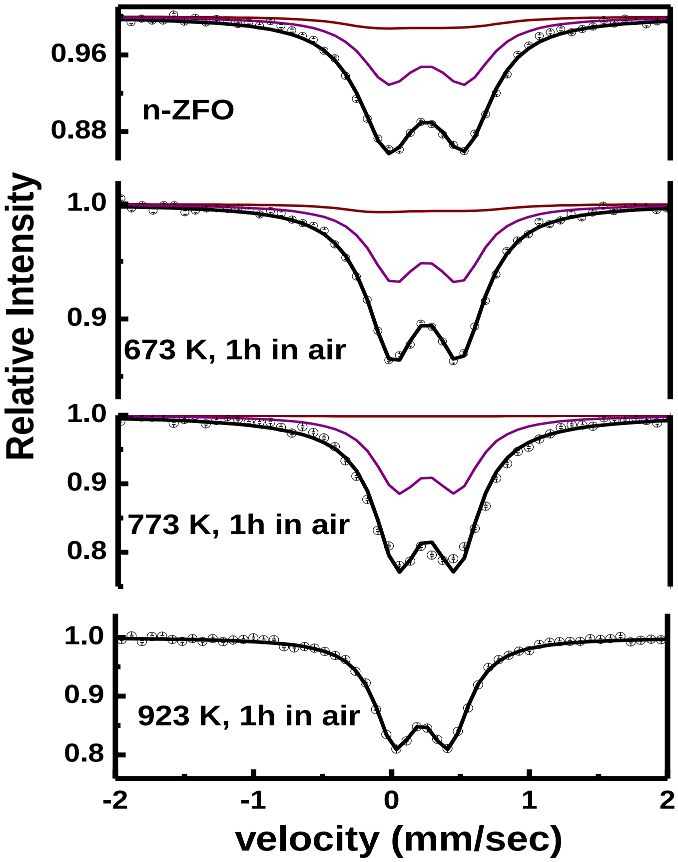

Figure 6.8: Mössbauer spectra of n-ZFO and the subsequent annealed sample at 673, 773, 923 K in air.

Table 6.3 – Mössbauer parameters of the n-ZFO and the air annealed samples.

Sample details	**Γ (mm/s)**	**δ (mm/s)**	**Δ (mm/s)**	**B_{hf} (T)**	**f %**
673 K in air	0.41(2)	0.35(0)	0.48(1)	-	85(1)
	0.53(0)	0.31(3)	0.07(0)	2.6(4)	15(1)
773 K in air	0.39(0)	0.36(0)	0.42(0)	-	85(0)
	1.59(0)	0.29(0)	-0.01(4)	3.19(f)	15(1)
923 K in air	0.36(1)	0.34(0)	0.39(0)	-	100(3)

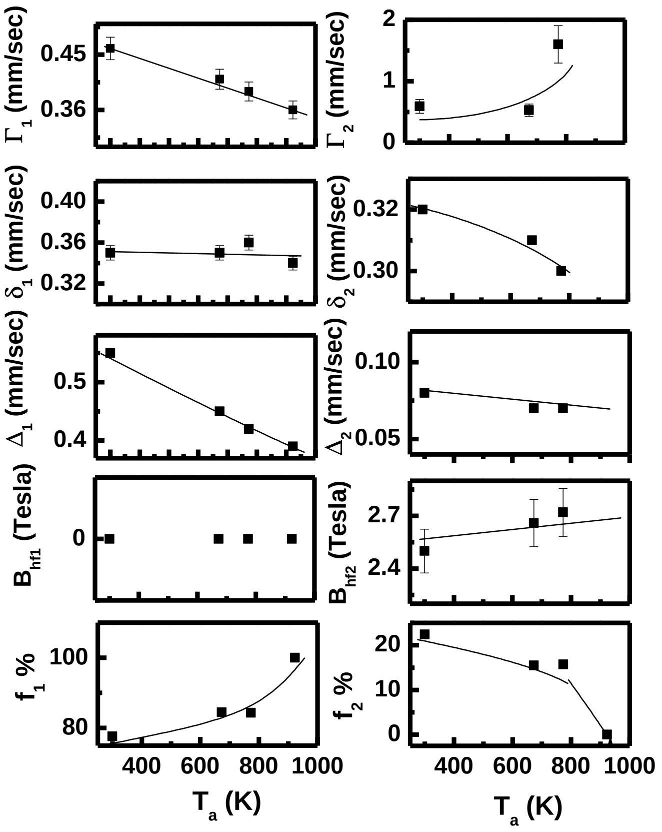

Figure 6.9: Mössbauer hyperfine parameters of the paramagnetic doublet (left column) and the magnetically ordering component (right column) in the n-ZFO as due annealing in air.

To this effect a gradual decrease in line width and quadrupole splitting Γ_1 and Δ_1 are seen while Γ_2 and Δ_2 almost remain constant. Summarizing the Mössbauer study clearly implies that the observed line broadening of Mössbauer spectrum in nano zinc ferrite is understood due to the onset of ferromagnetic ordering which is understood to be due to a partial inversion in the population of $(Zn^{2+})_A$ and $(Fe^{3+})_B$ sites. Mössbauer results obtained based on the measurements carried out at 300 and 87 K in the as prepared nanoparticles imply that the doublet as observed at 300 K is largely due to superparamagnetic relaxation effects in addition to a certain paramagnetic fraction. Subsequent to annealing treatment at 923 K results in a complete restoration of the paramagnetic doublet similar to that of the bulk. In the following defects studies is carried out on the bulk of ZnF_2O_4 using Mössbauer spectroscopy.

6.5 Point defects induced variation in local structure and magnetic properties of bulk $ZnFe_2O_4$

Bulk $ZnFe_2O_4$ prepared through combustion and ball milling are reported to exhibit ferromagnetic ordering [14,17]. The role of point defects leading to the observed structural and magnetic properties of these ferrites is yet to be understood. This study is on the bulk $ZnFe_2O_4$ subjected to a non-equilibrium effect viz., quenching from high temperature and at a low partial pressure to modify the cationic distribution and hence to look for the changes in the local magnetic properties.

Bulk $ZnFe_2O_4$ has been subjected to annealing at 1373 K for 7 hrs at a partial pressure of 10^{-6} mbar. XRD spectrum obtained in the annealed sample shows only the peaks characteristic of $ZnFe_2O_4$ (Cf. Figure 6.10). Mössbauer spectrum obtained subsequent to the above annealing treatment as shown in Figure 6.11 implies a large increase in linewidth of the spectrum. The spectrum obtained in the as prepared bulk $ZnFe_2O_4$ is also provided for a comparison. Based on the arguments used for the analysis of the results corresponding to nano $ZnFe_2O_4$, the spectra were fitted with a doublet and one or more sextets depending upon the spectrum. The corresponding Mössbauer spectrum (Cf. Fig 6.11) could be fitted with a doublet of relative area of 46 % while the remaining area could be fitted with three sextets. The results in terms of the hyperfine parameters as experienced by different relative fractions of absorber atoms are shown in the Table 6.4. Fraction of iron atoms occupying site 3 representing the relative area of 46 % of the Mössbauer spectrum, can be understood to be associated with disordered spin configurations implied by a low value of hyperfine field ≈ 23 Tesla and a large value of linewidth 4.6 mm/sec.

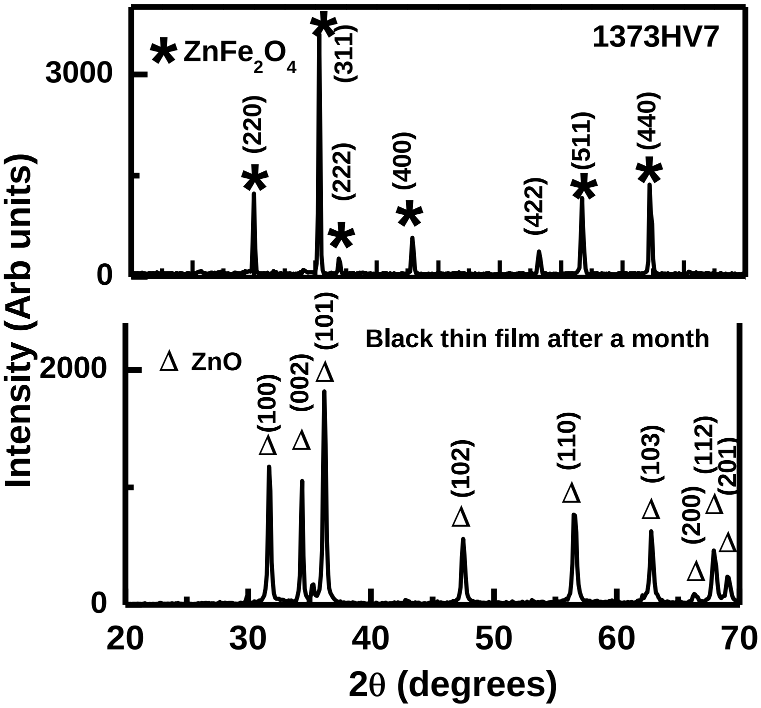

Figure 6.10. XRD spectra obtained in the bulk $ZnFe_2O_4$ subsequent to annealing at 1373 K for 7 Hrs at a partial pressure of 10^{-6} mbar and in the black film which got coated on the sides of quartz tube during the process of annealing.

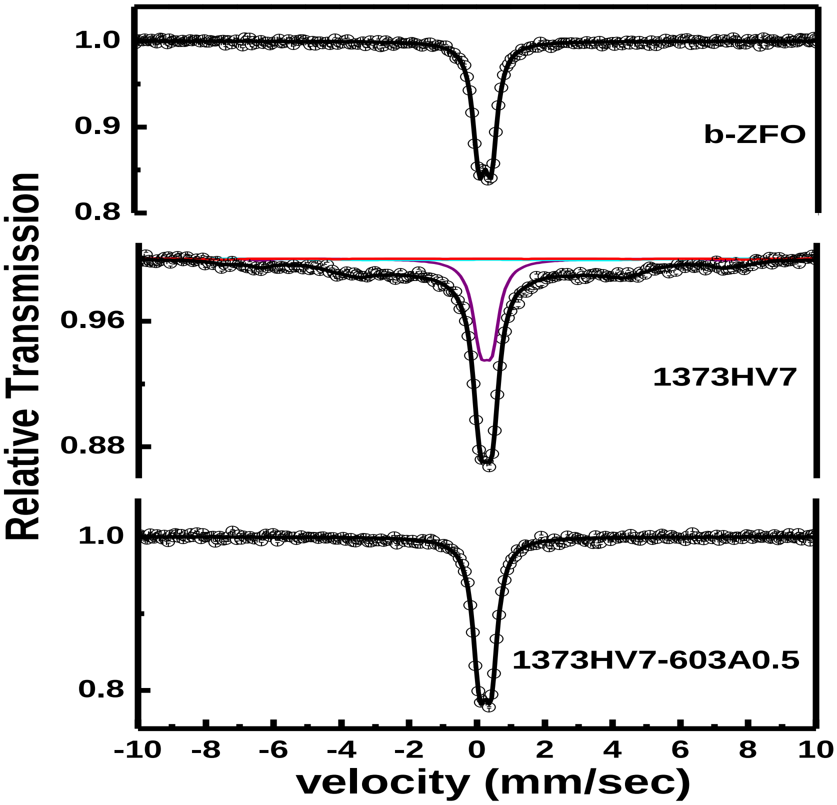

Figure 6.11: Mössbauer spectra of b-ZFO, b-ZFO annealed at 1373 K for 7 h in 10^{-6} mbar (1373HV7), post heat treatment of the sample 1373HV7 at 700 K for 30 min.

A large linewidth of this component might imply a high degree of non-unique configuration of this defect. In addition two sextets could also be fitted with a relative area of 2 % and 6 % with the fractions of Fe atoms experiencing hyperfine fields 47.4 and 43 Tesla respectively. These are understood to arise due to Fe atoms associated with unique defect configurations resulting in magnetic interaction. It is important to notice that the sites 2 and 4 are associated with Fe atoms experiencing high value of isomer shift 0.55 mm/sec and hence could be of valence close to +2.5. A mild black coating on the quartz tube was present soon after annealing treatment at elevated temperature which got turned in to white in a few days. The coated particles were collected and were confirmed to be of ZnO based on XRD spectrum (Cf. Figure 6.10).

Table 6.4: Mössbauer results on the sample b-ZFO and subjected to various treatments as explained in this work.

Sample details	**Γ (mm/s)**	**δ (mm/s)**	**Δ (mm/s)**	**B_{hf} (T)**	**f (%)**
b-ZFO	0.43(4)	0.34(7)	-0.32(2)	-	100(3)
1373HV7	0.51(1)	0.37(0)	0.34(0)	-	46(1)
	4.61(9)	0.55(8)	-0.26(7)	22.9(9)	46(4)
	0.70(0)	0.33(9)	-0.07(5)	47.4(9)	02(1)
	0.87(8)	0.55(5)	0.10(7)	42.8(8)	06(0)
1373HV7-603A0.5	0.47(1)	0.37(0)	0.34(0)	-	100(3)

1373HV7 implies b-ZFO subjected to annealing at 1373 K at 10^{-6} mbar for 7 hrs. This sample subsequent to annealing in air for 30 min at 603 K is referred to as 1373HV7-603A0.5 in the table.

The sample previously subjected to quenching treatment at 1373 K was annealed in air at 673 K and Mössbauer measurement has been carried out at 300 K. Mössbauer measurement carried out at 300 K shows that all the fractions of Fe atoms experience pure quadrupole interaction with quadrupole parameters almost similar to that of the bulk.

Towards a better comprehension of the point defects induced magnetic effects, Mössbauer measurements have also been carried out at 87 K on the sample subsequent to vacuum annealing at 1373 K. Mössbauer measurement was also carried out at 87 K on the vacuum annealed bulk $ZnFe_2O_4$ sample following the annealing treatment in air at 603 K (Cf. Figure 6.12). The fitted Mössbauer spectra obtained at 87 K on these samples were presented below and the fitted hyperfine parameters are listed in the Table 6.5.

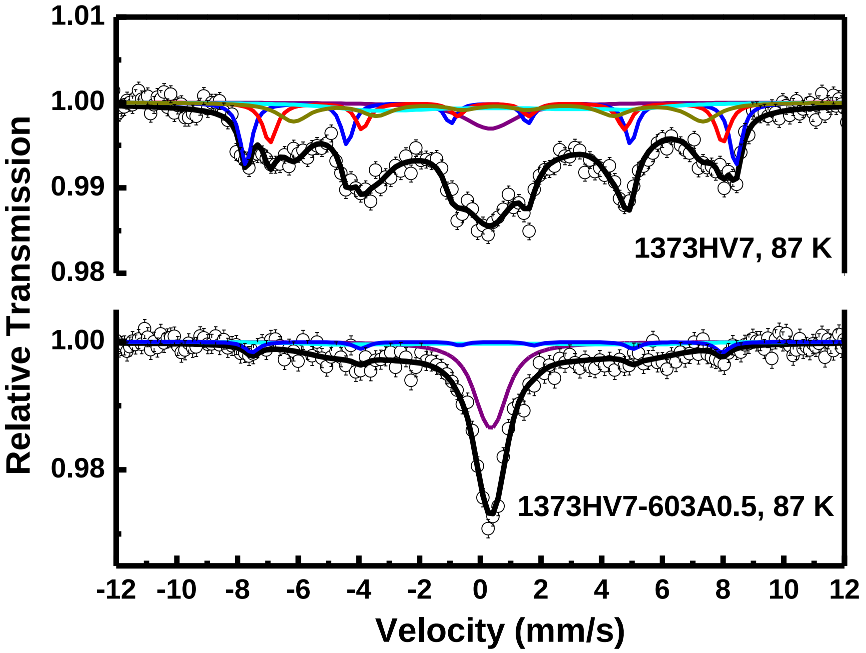

Figure 6.12. Mössbauer spectra of the sample 1373HV7 and 1373HV7-603A0.5 at 87 K.

Table 6.5: Fitted Mössbauer parameters of the sample b-ZFO subjected to various treatments as obtained at 87 K.

Sample details	**Γ (mm/s)**	**δ (mm/s)**	**Δ (mm/s)**	**B_{hf} (T)**	**f %**
1373HV7 at 87 K	1.92(8)	0.45(4)	0.42(0)	-	11(0)
	2.83(9)	0.49(8)	0.34(6)	27.0(9)	39(2)
	1.24(9)	0.66(5)	0.10(9)	41.8(5)	26(1)
	0.55(7)	0.59(3)	0.09(4)	46.2(2)	11(0)
	0.47(8)	0.43(2)	0.06(4)	50.0(1)	13(0)
1373HV7-603A0.5 at 87 K	1.09(0)	0.47(1)	0.37(0)	-	57(1)
	2.85(8)	0.52(0)	0.05(8)	32.8(8)	36(0)
	0.55(0)	0.50(0)	-0.32(8)	48.0(5)	07(0)

Mössbauer measurement at 87 K on the vacuum annealed sample indicates that as high as 89 % of Fe atoms are exposed to magnetic hyperfine interactions. On comparison of the results obtained at 300 and 87 K, It is important to observe based on the hyperfine parameters that only about 11 % of Fe atoms are still associated with normal ferritic configuration exhibiting a paramagnetic doublet while the remaining 89% of Fe atoms experience magnetic interaction. About 39% of Fe atoms experience a low value of hyperfine field close to 25 Tesla and with a large value of linewidth similar to the result obtained at 300 K. The component with large linewidth and a low hyperfine field is understood to emanate from different off-stoichiometric configurations leading to occupation of Fe^{3+} at A sites and with varying degree of population inversion. Based on the large value of the observed linewidth, this defect component is understood to mainly arise from regions close to grain boundaries of the crystallites and experiencing disordered spin configuration. The remaining 50% of Fe atoms are exposed to magnetic interactions with moderate values of linewidth might imply that these off-stoichiometric and varying inverse configurations are associated with the bulk of the sample. An appreciable concentration of Zn vacancies are likely to have been formed in the sample occurring in a large concentration close to grain boundaries which decreases inside the grains. This is mainly understood to result in the occupancy of Fe^{3+} at tetrahedral sites with the resulting cation vacancy at octahedral site. The occurrence of Fe^{3+} at both A and B sites lead to an appreciable value of J_{AB} resulting in the observed ferromagnetic ordering.

On the other hand the Mössbauer measurement carried out at 300 K on the air annealed sample shows the complete restoration of normal ferritic configuration with a doublet. While Mössbauer measurement at 87 K on this sample shows that only close to 60 % of Fe atoms are restored to that of normal configuration while the remaining 40 % of Fe atoms are exposed to defects induced ferromagnetic ordering. This might imply that in the bulk sample subjected to vacuum annealing at elevated temperatures close to 1370 K there is a significant degree of off stoichiometry due to Zn deficiency which has resulted in varying degree of inverse spinel configuration. In the vacuum annealed condition the Zn vacancies formed in the sample result in an inverse spinel configuration with varying degree ranging from high concentration close to grain boundaries and becoming zero at the core of the grains. These defective zones with inverse spinel configurations exhibiting magnetic ordering might be occurring in length scale of the order of a few nanometers and might be occurring in an appreciable concentration close to grain boundaries and decrease towards the core of the grains.

Summarizing the vacuum annealing of bulk $ZnFe_2O_4$ at 1373 K is seen to introduce Zn vacancies in the sample resulting in off-stoichiometry. This is understood to result in a partial inversion in the population of Fe^{3+} to A sites of varying degree in the sample thus resulting in the occurrence of ferrimagnetic ordering due to predominant A-O-B super exchange interaction. In addition the defect treatment also results in the occurrence of Fe^{2+} in predominant concentration based on Mössbauer results. Occurrence of Fe^{2+} in thin film of $ZnFe_2O_4$ has been reported [15]. Zn vacancies are understood to have been formed in a large concentration close to grain boundaries. A large value of linewidth associated with these sextets implies a large degree of non-uniqueness of these defects. Occurrence of Zn vacancies results in the partial occurrence of Fe^{3+} at A sites resulting in an enhanced J_{AB} thus leading to the observed ferromagnetic ordering. An appreciable concentration of Zn cations are understood to be segregated nearby grain boundaries. Annealing in air results in a partial restoration of Zn to tetrahedral sites followed by the diffusion of Fe^{3+} back to octahedral sites. This results in a normal ferritic configuration with the reappearance of a doublet at 300 K subsequent to annealing in air. While the Mössbauer measurement carried out on this sample at 87 K shows that about 60 % of the Fe atoms are associated with paramagnetic doublet. This might imply that the remaining 40 % of Fe atoms are associated with defective zones exhibiting magnetic ordering extending over a few nm.

Based on the results of Mössbauer studies the schematics of the point defects contributing for the ferromagnetic ordering in the case of nano and bulk $ZnFe_2O_4$ is shown below.

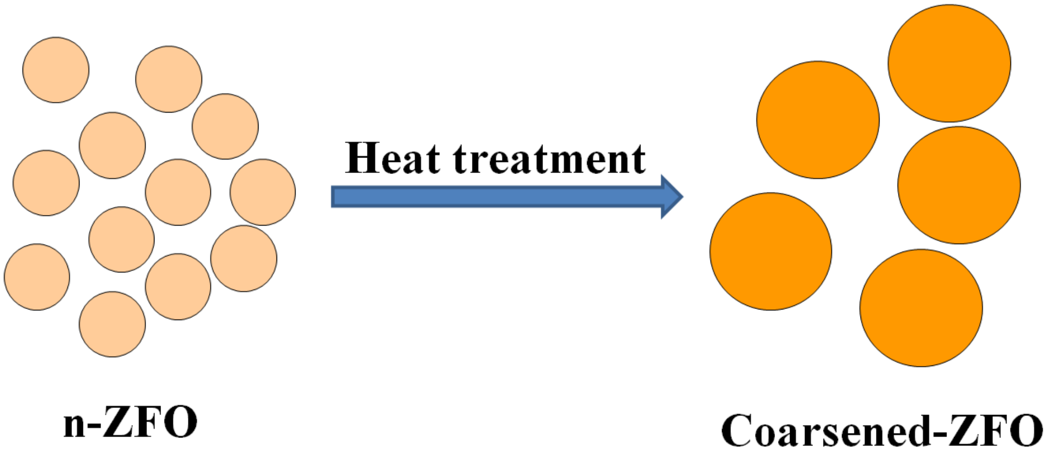

Figure 6.13: Schematic of nanoparticles of $ZnFe_2O_4$ and their restoration to normal ferrite and paramagnetic particles due to coarsening due to annealing is shown.

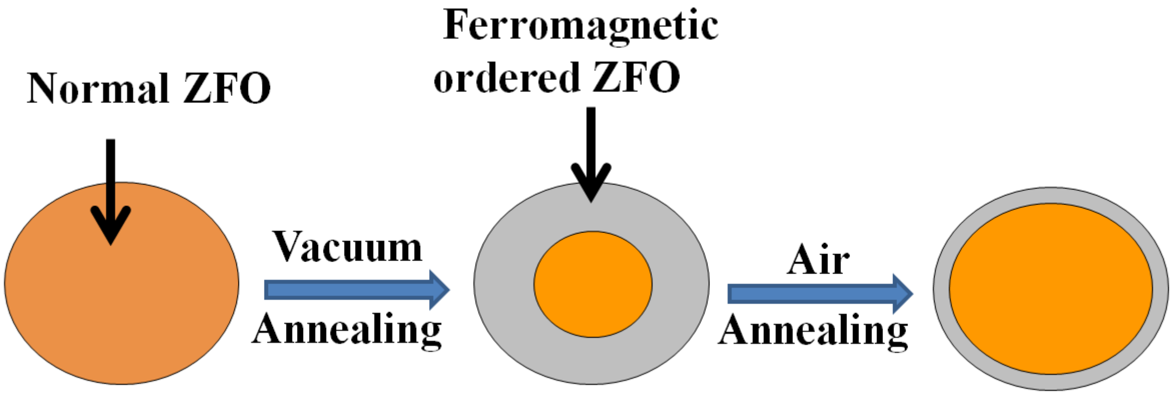

Figure 6.14: Vacuum annealing of Bulk $ZnFe_2O_4$ results in a shell of ferromagnetic ordered zones at grain boundaries. This is depicted to be due to Zn vacancies created in the sample. These Zn^{2+} largely occur at the grain boundaries. This results in population of Fe^{3+} at both A and B sites at a large volume fraction of sample close to grain boundaries. Annealing in air leads to back diffusion of Zn^{2+} to A sites with a concomitant back population of Fe^{3+} to B sites restoring back the normal ferritic configuration in a large volume fraction of the sample.

In the case of nanoparticles the observed ferromagnetic ordering is understood to emerge from the partial inversion in the population of Zn^{2+} and Fe^{3+} leading to the occurrence of Fe^{3+} at both A and B sites. This results in an enhanced J_{AB} leading to the observed ferromagnetic ordering. Evidenced by Mössbauer measurement at 77 K and also based on the fact that the mean particle size is of the order of a few nm it is understood that these particles are subjected to superparamagnetic relaxation of spins at 300 K. Annealing at elevated temperatures in air results in an increase in the size of the particle leading to a paramagnetic doublet at 300 K with quadrupole parameters as that of the bulk. Here the nanoparticles are schematized to have core and shell with shell characterized to have J_{AB} >> 0 and a core with J_{AB} = 0. Coarsening results in a normal ferritic behavior similar to that of the bulk.

Bulk $ZnFe_2O_4$ subjected to vacuum annealing results in the occurrence of Zn vacancies with varying off-stoichiometry and hence the occupation of Fe^{3+} at Zn sites. This case also results in a varying degree of the inversion in the population of Fe^{3+} at A sites. Hence an enhanced J_{AB} along with non-zero and an appreciable J_{AA} and J_{BB} cause the occurrence of other ferrimagnetic components. The fractions of Fe atoms associated with magnetic ordering increases due to enhanced magnetic interaction due to orientation of disordered surface spins as were existing at 300 K. Annealing in air at 623 K for 30 minutes results in an appreciable restoration of Zn^{2+} to tetrahedral sites. This leads to an increased population of Fe^{3+} back at B sites resulting in a J_{AB} = 0 in an appreciable volume of the sample. A relative fraction close to 40 % of Fe sites are still associated with magnetic interaction deduced based on the measurement carried out at 87 K in the air annealed sample. The schematic shows the occurrence of Zn deficient grain boundary zones having Fe^{3+} occurring at both A and B sites leading to J_{AB} >> 0 leading to the observed ferromagnetic ordering. Zn^{2+} are occurring in an appreciable fraction at the grain boundaries. Annealing in air largely result in the back occupation of Zn^{2+} at A sites concomitant to the back population of Fe^{3+} to B sites. This results in a large volume fraction of the sample the normal configuration of cationic population leading to J_{AB} = 0. A small volume fraction (≈ 35%) close to grain boundary is seen to exhibit magnetic ordering close to 87 K as shown schematically.

6.6 Conclusion:

Evolution of hyperfine parameters across off-stoichiometric to stoichiometric magnetite has been studied due to controlled annealing treatments of the nanoparticles using Mössbauer spectroscopy. Besides the occurrence of cationic vacancies at octahedral sites the plausible occupation of Fe^{2+} at tetrahedral sites in off stoichiometric magnetite nanoparticles has been pointed out by the Mössbauer results. Nanoparticles of $ZnFe_2O_4$ are shown to exhibit ferrimagnetic ordering which is understood to be due to an inversion in the population of Fe^{3+} and Zn^{2+} which are known to occupy only B and A sites respectively in bulk $ZnFe_2O_4$. Observation of ferromagnetic ordering in vacuum annealed bulk $ZnFe_2O_4$ has also been reported in this chapter which is understood to be due to Zn^{2+} vacancies in regions close to grain boundaries resulting in a segregation of Zn^{2+} at grain boundaries. This is accompanied by the occurrence of Fe^{3+} at both tetrahedral and octahedral sites leading nonzero value of J_{AB} understood to result in a ferromagnetic shell and a paramagnetic core. Annealing in air predominantly results in the back diffusion of Zn^{2+} to tetrahedral sites preceded by the back diffusion of Fe^{3+} from tetrahedral sites to vacant octahedral sites resulting in restoration of normal ferritic configuration.

6.7 References

[1] A. N. Cormack, G. V. Lewis, S. C. Parker and C. R. A. Catlow, *J. Phys. Chem. Solids*, **49**, 53 (1988)

[2] G. Kh. Rozenberg, Y. Amiel, W. M. Xu, M. P. Pasternak, R. Jeanloz, M. Hanfland and R. D. Taylor, *Phys. Rev. B*, **75**, 020102(R) (2007)

[3] S. Wibmann, V. v. Wurmb, F. J. Litterst, R. Dieckmann and K. D. Becker, *J. Phys. Chem. Solids*, **59**, 321 (1998)

[4] M. P. Pasternak, S. Nasu, K. Wada and S. Endo, *Phys. Rev. B*, **50**, 6446 (1994)

[5] A. Yang, C N Chinnasamy, J M Greneche, Y. Chen, S. D Yoon, Z. Chen, K. Hsu, Z. Cai, K. Ziemer, C Vittoria and V G Harris, *Nanotechnology*, **20**, 185704, (2009)

[6] M. Younas, M. Nadeem, M. Atif and R. Grossinger, *J. Appl. Phys*., **109**, 093704 (2011)

[7] J. H. Shim, S. Lee, J. H. Park, S.-J. Han, Y. H. Jeong and Y. W. Cho, *Phys. Rev. B*, **73**, 064404 (2006)

[8] S. Nakashima, K. Fujita, K. Tanaka, K. Hirao, T. Yamamoto and I. Tanaka, *Phys. Rev. B*, **60**, 75, 174443 (2007)

[9] S. A. Oliver, H. H. Hamdeh and J. C. Ho, *Phys. Rev. B*, **60**, 3400 (1999)

[10] J. Wu, N. Li, J. Xu, Y. Jiang, Z.-G. Ye, Z. Xie, and L. Zheng, *Appl. Phys. Lett*., **99**, 202505, (2011)

[11] G. F. Goya, T. S. Berquo, F. C. Fonseca and M. P. Morales, *J. Appl. Phys*., **94**, 3520 (2003)

[12] M. Penicaud, B. Siberchicot, C.B. Sommers and J. Kubler, *J. Magn. Magn. Mater*., **103**, 212 (1992)

[13] P. Ravindran, R. Vidya, H. Fjellvåg and A. Kjekshus, *Phys. Rev. B*, **77**, 134448 (2008)

[14] J. H. Shim, S. Lee, J. H. Park, S.-J. Han, Y. H. Jeong and Y. W. Cho, *Phys. Rev. B*, **73**, 064404 (2006)

[15] C. E. Rodriguez Torres, F. Golmar, M. Ziese, P. Esquinazi and S. P. Heluani, *Phys. Rev. B*, 84, 064404 (2011)

[16] W. Schiessl et al, *Phys. Rev. B*, **53**, 9143 (1996)

[17] H. Xue, Z. Li, X. Wang and X. Fu, *Materials Letters*, **61**, 347 (2007)

CHAPTER 7

SUMMARY AND FUTURE PERSPECTIVES

CHAPTER 7

SUMMARY AND FUTURE PERSPECTIVES

7.1 Summary

The conclusions of the work carried out in the present thesis with respect to the local structure and magnetic properties of nano / bulk cubic spinel ferrites and iron oxyhydroxides are summarized as bellow:

- Partial conversion of orthorhombic α-FeOOH to cubic phases such as γ-Fe_2O_3 and reduction to Fe_3O_4 in the temperature regimes 400-460 K and 500-625 K respectively have been deduced based on Mossbauer results. This is comprehended due to the role of hydrogen which gets dissociated from water molecule bound to OH vacancies of α-FeOOH. This creates oxygen vacancies thus increasing the concentration of Fe ions locally which diffuse in a stacked manner to result in a partial conversion of α-FeOOH to cubic γ-Fe_2O_3. Topotactical formation of α-FeOOH to α-Fe_2O_3 is observed for annealing treatments above 500 K and this effect becomes predominant for annealing above 650 K [1]. These results have been discussed in chapter 3.

- The role of oleic acid as a surfactant stabilizing the nanoparticles of iron oxyhydroxide and cubic iron oxides has been studied in a detailed manner based on the evolution of hyperfine parameters with respect to controlled annealing treatment has been deduced using Mossbauer spectroscopy. Physics of strong binding and hence higher temperature of dissociation of oleic acid bound to Fe_3O_4 nano particles than that of OA bound to α-FeOOH has been elucidated in this study presented in chapter 4. Formation of different phases of iron oxides in core-shell structure is elucidated due to controlled annealing treatments of oleic acid capped nano particles of iron oxides and hydroxides [2].

- A strong binding of magnetite nanoparticles of size of the order of 4-5 nm in zeolite template has been established based on the Mossbauer results as presented in chapter 5. Measurements carried out in the temperature interval 300-80 K establishes a strong dependence of magnetic dipolar interactions on the observed hyperfine parameters in particular the hyperfine fields at the sites of absorber atoms. This is further illustrated based on the comparison of Mössbauer results with that obtained in the zeolite sample dispersed with much lower concentration of almost same sized magnetite nanoparticles. Evolution of hyperfine parameters due to enhanced magnetic dipolar interactions with decreasing temperature has been presented [3].
- Mossbauer results as obtained in vacuum annealed off stoichiometric magnetite sample point to a possibility of the occupation of Fe^{2+} at tetrahedral sites in nanoparticles of off-stoichiometric magnetite as presented in chapter 6. With an increase in the size of the particle due to controlled annealing treatment in vacuum the particles get reduced to stoichiometric magnetite [4].
- In the case of $ZnFe_2O_4$ nanoparticles the observed ferromagnetic ordering is understood to emerge from the partial inversion in the population of Zn^{2+} and Fe^{3+} leading to the occurrence of Fe^{3+} at both A and B sites. This results in an enhanced J_{AB} leading to the observed ferromagnetic ordering. Evidenced by Mossbauer measurement at 77 K and also based on the fact that the mean particle size is of the order of a few nm it is understood that these particles are subjected to superparamagnetic relaxation of spins at 300 K. Annealing at elevated temperatures in air results in an increase in the size of the

particle leading to a paramagnetic doublet at 300 K with quadrupole parameters as that of the bulk.

- Bulk $ZnFe_2O_4$ subjected to vacuum annealing results in the occurrence of Zn vacancies with varying off-stoichiometry and hence the occupation of Fe^{3+} at Zn sites. This case also results in a varying degree of the inversion in the population of Fe^{3+} at A sites. Hence an enhanced J_{AB} along with non-zero and an appreciable J_{AA} and J_{BB} cause the occurrence of other ferrimagnetic components. The fractions of Fe atoms associated with magnetic ordering increases due to enhanced magnetic interaction due to orientation of disordered surface spins as were existing at 300 K. Annealing in air at 623 K for 30 minutes results in an appreciable restoration of Zn^{2+} to tetrahedral sites. This leads to an increased population of Fe^{3+} back at B sites resulting in a $J_{AB} = 0$ in an appreciable volume of the sample. A relative fraction close to 40 % of Fe sites are still associated with magnetic interaction deduced based on the measurement carried out at 87 K in the air annealed sample [5].

7.2 Future perspective

With the understanding obtained in the investigation on the cubic spinel iron oxides and iron oxyhydroxide, the following some of the proposed studies could form a future perspective.

- Adsorption / immobilizing of heavy metallic ions from the solution using magnetized iron oxyhydroxide or cubic spinel iron oxide nano particles / rods followed by Mossbauer studies to study the evolution of hyperfine parameters. As the adsorbed metallic ions are non-magnetic and of different ionic size than Fe^{2+}/Fe^{3+}, these might result in a change in local structure and magnetic properties.

- Studies of magnetite interaction between magnetite nanoparticles prepared through different methods to result in different anisotropic shapes.
- Kinetics of cationic vacancies evolution with respect to sintering effect in nanoparticles.
- Cationic arrangement of the interstitial sites in various normal, mixed and inverse ferrites subjected to different non-equilibrium treatments such as ion implantation, fast neutron irradiation..

7.3 References

[1] L. Herojit singh, R. Govindaraj, R. Mythili, G. Amarendra and C. S. Sundar, *AIP Advances*, **3**, 022101 (2013)

[2] L. Herojit singh, R. Govindaraj, G. Amarendra and C. S. Sundar, *J. Phys. Chem. C*, 117, 25042−25051 (2013).

[3] L. Herojit singh, R. Govindaraj, G. Amarendra and C. S. Sundar, *Appl. Phys. Lett*., **103**, 193104 (2013).

[4] L. Herojit singh, R. Govindaraj, G. Amarendra and C. S. Sundar, *AIP Conf. Proc*., **1447**, 445 (2012)

[5] L. Herojit singh, R. Govindaraj, G. Amarendra and C. S. Sundar, "Defect induced ferromagnetism in $ZnFe_2O_4$", (Manuscript under preparation)

LIST OF PUBLICATIONS

PUBLICATIONS PERTAINING IN THESIS:

1. "Atomic scale study of thermal reduction of nano goethite coexisting with magnetite", **L. Herojit. Singh**, R. Govindaraj, R. Mythili, G. Amarendra and C. S. Sundar, *AIP Advances*, **3**, 022101 (2013)

2. "Atomic scale study on the thermal evolution of local structure and magnetic properties in oleic acid coated iron oxide nanoparticles", **L. Herojit Singh**, R. Govindaraj, G. Amarendra and C. S. Sundar, *J. Phys. Chem. C*, **117**, 25042 (2013)

3. "Local structure and magnetic properties of cubic iron oxide nanoparticles formed in zeolite as deduced using Mössbauer spectroscopy", **L. Herojit singh**, R. Govindaraj, G. Amarendra and C. S. Sundar, *App. Phys. Lett.*, **103**, 193104 (2013)

4. "Point defects aspect of magnetite nano particles as studied by Mössbauer spectroscopy", **L Herojit Singh**, R Govindaraj, G Amarendra and C. S. Sundar, *AIP Conf. Proc.*, **1447**, 445 (2012)

5. "Partial inversion in nano zinc ferrite as studied using Mössbauer spectroscopy", **L Herojit Singh**, R Govindaraj, G Amarendra and C. S. Sundar, *AIP Conf. Proc.*, **1512**, 322 (2013)

6. "Mössbauer Studies of Local Environments of 57Fe in Iron Oxide Particles Dispersed Fe Matrix", **L. Herojit Singh**, R Govindaraj, P. A. Kumar, G. Amarendra, C. S. Sundar, *AIP Conf. Proc.*, 1349, 423 (2011)

7. "Studies on local structure and magnetic properties of polymorphs of iron oxides by Mössbauer spectroscopy", **L. Herojit Singh**, R. Govindaraj, G. Amarendra and C. S. Sundar, MRSI 2010, Trivandrum

8. Defect induced ferromagnetism and recovery in $ZnFe_2O_4$, (Manuscript under preparation)

9. Linear correlation between hyperfine parameters as observed in the thermal evolution of iron oxide nano particles, (Manuscript under preparation)

10. Aspect of local structure and magnetic properties in chemically synthesized magnetic nanoparticles as studied using Mossbauer spectroscopy, (Manuscript under preparation)

List of publications and conference proceedings not pertaining to thesis work:

1. “Annealing effects in Eurofer-97 steel as studied by Mössbauer spectroscopy”, **L. Herojit Singh**, S. Hari Babu, R. Govindaraj, G. Amarendra, and C. S. Sundar, *AIP Conf. Proc.*, **1447**, 1321 (2012)
2. “Mössbauer Spectroscopic studies in Ni-Fe-Co Alloy”, **L. Herojit Singh**, R. Govindaraj, C. Ravishankar, G. Amarendra and C. S. Sundar, *MRSI-AGM*, (2013)

ADDENDUM

Table 1: Mössbauer parameters of the bulk goethite, Magnetite, Maghemite and Hematite.

Phase	**δ_i (mm/s)**	**Δ_i (mm/s)**	**B_{hf}^i (T)**	**f_i (%)**
Goethite (α-FeOOH) [**1**]	0.35	-0.28	38.0	100
Magnetite (Fe_3O_4) [**2**]	0.28 0.67	-0.03 0.02	48.9 45.8	34 66
Maghemite (γ-Fe_2O_3) [**3**]	0.33	0.01	50.1	100
Hematite (α-Fe_2O_3) [**4**]	-0.22	0.37	51.4	100

References:

[1] M. Gotic and S. Music, *J. Mol. Struct*., **834-836** (2007) 445.

[2] M. Gotic and S. Music, *Eur. J. Inorg. Chem*., **2008** (2008) 966.

[3] E. Schmidbauer, M. Keller, *J. Magn. Magn. Mater*., **297** (2006) 107.

[4] M. Zic, M. Ristic, . Music, *J. Mol. Struct.*, **834-836** (2007) 141.